



# Assessment of the ascending thoracic aortic aneurysm rupture risk based on the local arterial stiffness

Solmaz Farzaneh

## ► To cite this version:

Solmaz Farzaneh. Assessment of the ascending thoracic aortic aneurysm rupture risk based on the local arterial stiffness. Other. Université de Lyon, 2019. English. NNT : 2019LYSEM006 . tel-03461281

**HAL Id: tel-03461281**

**<https://theses.hal.science/tel-03461281>**

Submitted on 1 Dec 2021

**HAL** is a multi-disciplinary open access archive for the deposit and dissemination of scientific research documents, whether they are published or not. The documents may come from teaching and research institutions in France or abroad, or from public or private research centers.

L'archive ouverte pluridisciplinaire **HAL**, est destinée au dépôt et à la diffusion de documents scientifiques de niveau recherche, publiés ou non, émanant des établissements d'enseignement et de recherche français ou étrangers, des laboratoires publics ou privés.



N°d'ordre NNT : 2019LYSEM006

**THESE de DOCTORAT DE L'UNIVERSITE DE LYON**  
opérée au sein de  
**l'Ecole des Mines de Saint-Etienne**

**Ecole Doctorale N° 488**  
**Sciences, Ingénierie, Santé**

**Spécialité de doctorat** : Mécanique et ingénierie

Soutenue publiquement le 15/02/2019, par :  
**(Solmaz Farzaneh)**

---

**Evaluation du risque de rupture d'un anévrisme de l'aorte  
thoracique ascendante en fonction de la rigidité artérielle locale**

---

Assessment of the ascending thoracic aortic aneurysm rupture risk based on  
the local arterial stiffness

---

Devant le jury composé de :

Duprey, Ambroise	Professore	CHU de Reims	Président
Labrosse, Michel	Professor	University of Ottawa	Rapporteur
Lalande, Alain	Professor	Université de Bourgogne	Rapporteur
Morbiducci, Umberto	Professor	Politecnico di Torino	Examineur
Stephane, Avril	Professor	MINES Saint-Étienne	Directeur de thèse
Trabelsi, Olfa	Associate Professor	université de technologie compiegne	Co-
directrice de thèse			

Spécialités doctorales	Responsables :	Spécialités doctorales	Responsables
SCIENCES ET GENIE DES MATERIAUX	K. Wolski Directeur de recherche	MATHEMATIQUES APPLIQUEES	O. Roustant, Maître-assistant
MECANIQUE ET INGENIERIE	S. Drapier, professeur	INFORMATIQUE	O. Boissier, Professeur
GENIE DES PROCÉDÉS	F. Gruy, Maître de recherche	SCIENCES DES IMAGES ET DES FORMES	JC. Pinoli, Professeur
SCIENCES DE LA TERRE	B. Guy, Directeur de recherche	GENIE INDUSTRIEL	X. Delorme, Maître assistant
SCIENCES ET GENIE DE L'ENVIRONNEMENT	D. Grailliot, Directeur de recherche	MICROELECTRONIQUE	Ph. Lalevée, Professeur

**EMSE : Enseignants-chercheurs et chercheurs autorisés à diriger des thèses de doctorat (titulaires d'un doctorat d'Etat ou d'une HDR)**

ABSI	Nabil	CR	Génie industriel	CMP
AUGUSTO	Vincent	CR	Image, Vision, Signal	CIS
AVRIL	Stéphane	PR2	Mécanique et ingénierie	CIS
BADEL	Pierre	MA(MDC)	Mécanique et ingénierie	CIS
BALBO	Flavien	PR2	Informatique	FAYOL
BASSEREAU	Jean-François	PR	Sciences et génie des matériaux	SMS
BATTON-HUBERT	Mireille	PR2	Sciences et génie de l'environnement	FAYOL
BEIGBEDER	Michel	MA(MDC)	Informatique	FAYOL
BLAYAC	Sylvain	MA(MDC)	Microélectronique	CMP
BOISSIER	Olivier	PR1	Informatique	FAYOL
BONNEFOY	Olivier	MA(MDC)	Génie des Procédés	SPIN
BORBELY	Andras	MR(DR2)	Sciences et génie des matériaux	SMS
BOUCHER	Xavier	PR2	Génie Industriel	FAYOL
BRODHAG	Christian	DR	Sciences et génie de l'environnement	FAYOL
BRUCHON	Julien	MA(MDC)	Mécanique et ingénierie	SMS
CAMEIRAO	Ana	MA(MDC)	Génie des Procédés	SPIN
CHRISTIEN	Frédéric	PR	Science et génie des matériaux	SMS
DAUZERE-PERES	Stéphane	PR1	Génie Industriel	CMP
DEBAYLE	Johan	MR	Sciences des Images et des Formes	SPIN
DEGEORGE	Jean-Michel	MA(MDC)	Génie industriel	Fayol
DELAFOSSSE	David	PR0	Sciences et génie des matériaux	SMS
DELORME	Xavier	MA(MDC)	Génie industriel	FAYOL
DESRAYAUD	Christophe	PR1	Mécanique et ingénierie	SMS
DJENIZIAN	Thierry	PR	Science et génie des matériaux	CMP
DOUCE	Sandrine	PR2	Sciences de gestion	FAYOL
DRAPIER	Sylvain	PR1	Mécanique et ingénierie	SMS
FAUCHEU	Jenny	MA(MDC)	Sciences et génie des matériaux	SMS
FAVERGEON	Loïc	CR	Génie des Procédés	SPIN
FEILLET	Dominique	PR1	Génie Industriel	CMP
FOREST	Valérie	MA(MDC)	Génie des Procédés	CIS
FRACZKIEWICZ	Anna	DR	Sciences et génie des matériaux	SMS
GARCIA	Daniel	MR(DR2)	Sciences de la Terre	SPIN
GAVET	Yann	MA(MDC)	Sciences des Images et des Formes	SPIN
GERINGER	Jean	MA(MDC)	Sciences et génie des matériaux	CIS
GOEURLOT	Dominique	DR	Sciences et génie des matériaux	SMS
GONDRAN	Natacha	MA(MDC)	Sciences et génie de l'environnement	FAYOL
GONZALEZ FELIU	Jesus	MA(MDC)	Sciences économiques	FAYOL
GRAILLOT	Didier	DR	Sciences et génie de l'environnement	SPIN
GROSSEAU	Philippe	DR	Génie des Procédés	SPIN
GRUY	Frédéric	PR1	Génie des Procédés	SPIN
GUY	Bernard	DR	Sciences de la Terre	SPIN
HAN	Woo-Suck	MR	Mécanique et ingénierie	SMS
HERRI	Jean Michel	PR1	Génie des Procédés	SPIN
KERMOUCHE	Guillaume	PR2	Mécanique et Ingénierie	SMS
KLOCKER	Helmut	DR	Sciences et génie des matériaux	SMS
LAFOREST	Valérie	MR(DR2)	Sciences et génie de l'environnement	FAYOL
LERICHE	Rodolphe	CR	Mécanique et ingénierie	FAYOL
MALLIARAS	Georges	PR1	Microélectronique	CMP
MOLIMARD	Jérôme	PR2	Mécanique et ingénierie	CIS
MOUTTE	Jacques	CR	Génie des Procédés	SPIN
NEUBERT	Gilles			FAYOL
NIKOLOVSKI	Jean-Pierre	Ingénieur de recherche	Mécanique et ingénierie	CMP
NORTIER	Patrice	PR1	Génie des Procédés	SPIN
O CONNOR	Rodney Philip	MA(MDC)	Microélectronique	CMP
OWENS	Rosin	MA(MDC)	Microélectronique	CMP
PERES	Véronique	MR	Génie des Procédés	SPIN
PICARD	Gauthier	MA(MDC)	Informatique	FAYOL
PIJOLAT	Christophe	PR0	Génie des Procédés	SPIN
PINOLI	Jean Charles	PR0	Sciences des Images et des Formes	SPIN
POURCHEZ	Jérémy	MR	Génie des Procédés	CIS
ROUSSY	Agnès	MA(MDC)	Microélectronique	CMP
ROUSTANT	Olivier	MA(MDC)	Mathématiques appliquées	FAYOL
SANAUR	Sébastien	MA(MDC)	Microélectronique	CMP
STOLARZ	Jacques	CR	Sciences et génie des matériaux	SMS
TRIA	Assia	Ingénieur de recherche	Microélectronique	CMP
VALDIVIESO	François	PR2	Sciences et génie des matériaux	SMS
VIRICELLE	Jean Paul	DR	Génie des Procédés	SPIN
WOLSKI	Krzysztof	DR	Sciences et génie des matériaux	SMS
XIE	Xiaolan	PR0	Génie industriel	CIS
YUGMA	Gallian	CR	Génie industriel	CMP

*Dedicated to my little Alice*







---

# Acknowledgements

I would like to express my sincere gratitude and appreciation to all who have supported me and contributed to this thesis.

Especially I would like to thank:

Prof. Stéphane Avril, my supervisor, for all the support and encouragement throughout this researching time. Your ability and your enthusiasm to find new approaches have inspired and guided me through the writing of this thesis and during my PhD-studies.

Dr. Olfa Trabelsi, co-supervisor, thank you for all scientific discussions that we had through this PhD.

Dr Ambroise Duprey, thank you for providing me CT images and all the data needed to start this research.

Thank you my colleges, PhD students and postdoctoral fellows for all support and a great time that we had together.

Fatemeh and Ebrahim, my mother and father, thanks for always supporting and believing in me. Thank you for all the love you are giving me and my family.

Mahnaz, Farahnaz and Vahid, my sisters and brother, thank you for being the best siblings and for all the joy we share.

My true love Jamal, my husband, thanks for all your support, giving me very smart ideas during this thesis and for always being there for me.



# Contents

---

<b>Acknowledgements</b>	<b>i</b>
<b>Contents</b>	<b>v</b>
<b>List of figures</b>	<b>viii</b>
<b>List of tables</b>	<b>ix</b>
<b>General Introduction</b>	<b>xi</b>
<b>1 State of the art</b>	<b>1</b>
1.1 Introduction . . . . .	2
1.2 The vascular system . . . . .	2
1.3 Cardiac Cycle . . . . .	3
1.4 Aorta . . . . .	4
1.5 Arterial Histology . . . . .	5
1.6 Mechanical behavior of arterial walls . . . . .	7
1.6.1 Nonlinearity and hyperelasticity . . . . .	8
1.6.2 Incompressibility . . . . .	8
1.6.3 Anisotropy . . . . .	8
1.6.4 Axial stretch and Residual stresses . . . . .	8
1.6.5 Twisting and shear deformation . . . . .	9
1.7 Vascular disease . . . . .	9
1.8 Aortic dissection and rupture . . . . .	9
1.9 Physiopathology of ATAA . . . . .	10
1.10 Symptoms and causes of ATAA . . . . .	11
1.11 Major factors in ATAA development . . . . .	12
1.11.1 Effects of aging . . . . .	12
1.11.2 Marfan syndrome . . . . .	13
1.11.3 Hypertension . . . . .	13

1.12	Diagnosis . . . . .	13
1.13	Treatments . . . . .	15
1.14	Issues posed by current risk criterion (diameter) . . . . .	16
1.15	Biomechanical factors instead of current risk criterion (diameter) . . . . .	17
1.16	Wall stress analysis of ATAA . . . . .	17
1.17	Wall strain analysis of ATAA . . . . .	18
1.18	Mechanical properties of ATAA . . . . .	19
1.19	Rupture risk indicator . . . . .	20
1.20	Inverse method . . . . .	21
1.21	Conclusion . . . . .	22
<b>2</b>	<b>Estimating aortic strain field using a pair of images and a mesh morphing approach</b>	<b>23</b>
2.1	Abstract . . . . .	25
2.2	Introduction . . . . .	25
2.3	Theory . . . . .	27
2.3.1	Method I . . . . .	28
2.3.2	Method II . . . . .	28
2.4	Materials and methods . . . . .	28
2.4.1	Data acquisition . . . . .	28
2.4.2	Computational implementation . . . . .	29
2.4.3	Numerical verification . . . . .	35
2.5	Results . . . . .	37
2.5.1	Method I . . . . .	38
2.5.2	Method II . . . . .	38
2.6	Discussion and conclusion . . . . .	40
<b>3</b>	<b>Inverse identification of local stiffness across ATAA</b>	<b>43</b>
3.1	Abstract . . . . .	46
3.2	Introduction . . . . .	46
3.3	Material and methods . . . . .	48
3.3.1	Origin of data . . . . .	48
3.3.2	Theory of the inverse approach . . . . .	48
3.3.3	Numerical implementation . . . . .	54
3.4	Results . . . . .	55
3.4.1	Numerical verification . . . . .	55
3.4.2	Linear elastic material property . . . . .	55
3.4.3	Non-linear anisotropic material property . . . . .	56
3.4.4	Patient-specific results . . . . .	59
3.4.5	Comparison of the results . . . . .	60
3.5	Discussion . . . . .	61
3.5.1	General remarks . . . . .	61

---

3.5.2	Limitations . . . . .	65
3.6	Conclusion . . . . .	66
<b>4</b>	<b>Identifying local arterial stiffness to assess the risk of rupture of ATAA</b>	<b>67</b>
4.1	Abstract . . . . .	69
4.2	Introduction . . . . .	69
4.3	Materials and methods . . . . .	70
4.3.1	The stretch ratio risk criterion . . . . .	70
4.3.2	The LESI methodology . . . . .	73
4.3.3	Statistical analysis . . . . .	75
4.4	Results . . . . .	77
4.5	Discussion . . . . .	80
4.5.1	Rupture risk criterion . . . . .	80
4.5.2	Regional variations of stiffness across ATAA . . . . .	85
4.5.3	Limitations . . . . .	86
<b>5</b>	<b>Extension of the methodology to MRI and ultrasound imaging</b>	<b>89</b>
5.1	Abstract . . . . .	91
5.2	Introduction . . . . .	91
5.3	Material and methods . . . . .	92
5.3.1	Ultrasound (US) . . . . .	92
5.3.2	Iterative Finite Element Analysis . . . . .	94
5.3.3	MRI . . . . .	95
5.3.4	Theory of the LESI methodology . . . . .	95
5.4	Results . . . . .	96
5.4.1	US . . . . .	96
5.4.2	MRI . . . . .	96
5.5	Discussion . . . . .	97
5.6	Future work . . . . .	98
	<b>General Conclusion</b>	<b>103</b>
	<b>Bibliography</b>	<b>105</b>
	<b>Annexe</b>	<b>119</b>





# List of Figures

1.1	Circulatory vascular system . . . . .	2
1.2	Cardiovascular system . . . . .	3
1.3	Normal blood pressure fluctuation in the aorta . . . . .	4
1.4	Anatomy of the aortic valve [59]. . . . .	5
1.5	Main bifurcations of the human aorta [7]. . . . .	6
1.6	Different regions of the human aorta . . . . .	6
1.7	Schematic model of the major components of an artery . . . . .	7
1.8	Aortic dissection . . . . .	10
1.9	Aortic rupture due to dissection of the aorta [6]. . . . .	10
1.10	Schematic demonstration of ATAA . . . . .	11
1.11	CT scan images of aorta . . . . .	14
1.12	Schematic illustration of ATAA replacement and aortic repair [1]. . . . .	16
2.1	Schematic illustration of morphing a reference mesh into a target geometry. . .	27
2.2	Centerlines and split surface (decomposition) of a real patient geometry . . . .	30
2.3	VMTK scripts . . . . .	33
2.4	Segmentation of the aortic geometry for diastolic phase . . . . .	33
2.5	Landmarks on the boundary of coronary and brachiocephalic arteries . . . . .	35
2.6	Panel of STL target in RBF morph <sup>®</sup> to apply the projection. . . . .	35
2.7	RBF morph points panel to introduce the landmarks . . . . .	36
2.8	Heterogeneous stiffness distribution in the aorta to obtain DG . . . . .	37
2.9	Map of the displacement magnitude obtained by the FEA model of a RG . . .	37
2.10	Map of the first principal strain obtained by the FEA model of a RG . . . . .	37
2.11	Map of displacement magnitude obtained by method I . . . . .	38
2.12	Map of first principal strain obtained by method I . . . . .	39
2.13	Displacement maps obtained by method II . . . . .	40
2.14	Strain maps obtained by method II . . . . .	40
3.1	Segmentation of the aortic geometry for diastolic phase . . . . .	51

3.2	Each element of arterial wall as a finite sector of an ellipsoidal membrane . . .	53
3.3	Flowchart of the methodology . . . . .	55
3.4	Map of the displacement magnitude . . . . .	56
3.5	Displacement maps . . . . .	57
3.6	Validation study for linear material properties . . . . .	58
3.7	Validation study for hyperelastic anisotropic material properties . . . . .	59
3.8	Distribution of local extensional stiffness for ascending and descending aortas .	60
3.9	Distribution of local extensional stiffness for in vivo and in vitro cuts . . . . .	62
3.10	Median and interquartile range of the local extensional stiffness . . . . .	63
4.1	Flowchart of the LESI methodology . . . . .	76
4.2	Regression of stiffness versus biomechanical parameters . . . . .	78
4.3	Stress–stretch curves . . . . .	81
4.4	Segmented geometries of aorta . . . . .	82
4.5	Boxplots of both groups of patients . . . . .	83
4.6	Extensional stiffness distribution . . . . .	84
5.1	Example of a 3D transesophageal US acquisition of an ATAA . . . . .	92
5.2	An overview of the segmentation process . . . . .	94
5.3	Segmented diastolic phases of a healthy case using MRI images. . . . .	95
5.4	Displacement reconstruction of a patient affected by ATAA using US images. .	96
5.5	Local extensional stiffness map of a patient with ATAA using US images. . . .	97
5.6	Local extensional stiffness map of healthy case using MRI images. . . . .	97
5.7	Registration of geometries segmented from MRI and CT scans together. . . . .	100
5.8	TAWSS and OSI resulting from the CFD analysis . . . . .	101

List of Tables

1.1	Advantages and disadvantages of different imaging modalities [49]. . . . .	15
2.1	Typical Radial Basis Functions. . . . .	34
2.2	Root mean square error values for each method . . . . .	39
3.1	Demographic information of three patients . . . . .	48
3.2	Values of non-linear anisotropic material parameters . . . . .	59
4.1	Clinical and biomechanical parameters of the 11 patients. . . . .	72
4.2	Median values of extensional stiffness identified in the different ATAA regions .	77
4.3	Pearson product-moment coefficient values . . . . .	79



---

# General Introduction

Cardiovascular disease is the leading cause of mortality worldwide. Based on the report of the World Health Organization (WHO), cardiovascular diseases take the lives of 17.9 million people every year which is 31% of all global deaths. It can be the result of aortic aneurysms or dissections. An aortic aneurysm is a dilation of an aortic segment which may lead to dissection or rupture causing eventually sudden death of a patient [101]. Some types of aneurysms may need surgical treatment to prevent rupture and some others may be stable for a life period. Nowadays physicians interpret an aneurysm as stable if its diameter is below 5.5 cm (or slow growing, growth  $< 1$  cm per year) otherwise a surgical intervention is recommended to repair it. Thus, most of deaths caused by aneurysm rupture can be prevented by choosing a proper treatment strategy such as watchful waiting (option A) or surgical intervention (option B) if it is necessary. It is suggested to assist physicians in taking the correct decision between option A and option B by considering biomechanical factors such as in vivo material properties of the tissue. As one of the function of arteries is to carry blood to the peripheral organs, any alteration to their mechanical properties has significant consequences. Consequently, understanding the mechanical properties of the aorta is important for the treatment of aortic diseases.

This thesis is a part of a project funded by the European Research Council (ERC-2014-CoG BIOLOCHANICS). In one of the work packages we predict the rupture risk of ATAAs for a cohort of patients, in the framework of a research protocol performed in compliance with the applicable French law and ethical standards and under the liability of the Saint-Etienne University Hospital (SEUH). The protocol is proposed to all patients operated in the Department of Cardiovascular Surgery for an ATAA surgical repair. All concerned patients are informed and give their express consent to contribute to this research according to the protocol specified in the consent form. After the surgical intervention on these patients, an ATAA segment is excised. From this segment, a square is cut in the outer curvature region and tested in bulge inflation. The stress-strain response is recorded to characterize the material property in ATAA. For all the included patients, X-ray computed tomography (CT) is employed before the surgical operation to image the aneurysm. Moreover, for each patient, systolic and diastolic pressures are recorded in the brachial artery. Image segmentation is achieved using the CT-scan to reconstruct a 3D mesh of each ATAA. Using all these data, the local strain distribution is reconstructed. Relating these strains to tensions with the extensional stiffness, the local extensional stiffness is finally derived at every position.

Based on previous studies, mechanical factors are introduced to estimate the rupture risk with increased reliability. In this thesis we develop a noninvasive inverse in vivo method (rather than in vitro) without any excision of the aorta to derive the local extensional stiffness (rather than the global stiffness) applicable as a reliable rupture risk criterion (rather than diameter). Moreover, we are interested in investigating the correlation between the local extensional stiffness identified on a cohort of patients with the stretch ratio risk criterion obtained from in vitro study based on bulge inflation tests. This thesis comprises 5 chapters:

1. Chapter 1 presents background research relevant to this thesis, including an introduction to the cardiovascular system, general background on aortic anatomy, physiology and histology, and an introduction to thoracic aortic aneurysms and prediction of aneurysm rupture risks.
2. In chapter 2 we estimate the aortic strain field using a pair of images through a cardiac cycle. Two methods are introduced based on mesh morphing functions to calculate displacements between a reference and a target geometry to track the same material points. In the first method an algorithm is developed to interpolate the coordinates of the reference mesh onto a target model based on the calculation of the parametric coordinates. In the second method, a radial basis function is used to map the reference mesh onto a target model.
3. In chapter 3 we introduce a novel inverse noninvasive methodology denoted by LESI (local extensional stiffness identification) [52], to identify *local* extensional stiffness non-invasively, by employing the gated CT scans and measured systolic and diastolic blood pressures. The methodology is applied to 3 patients in which the stiffness distribution is demonstrated. It is proved that the reconstruction of stiffness is correct on average and the local heterogeneity can be achieved using the LESI methodology [52]. This chapter is published in the BMMB journal (Farzaneh, S., Trabelsi, O. & Avril, S. Biomech Model Mechanobiol (2018). <https://doi.org/10.1007/s10237-018-1073-0>).
4. In chapter 4, we recruit 11 patients and we apply LESI method to all of them. Three regions of interest are selected through the aorta and statistical analysis is implemented between the median of extensional stiffness of segments and different mechanical parameters. A good correlation is found between the stretch ratio risk index and the extensional stiffness in the center of the square which corresponds to the bulge inflation sample. Finally it is shown that patients can be separated in two groups: a group of stiff and brittle ATAA and a group of relatively compliant ATAA. This chapter is submitted to Annals of Biomedical Engineering and is under revision.
5. Chapter 5 is the extension of the method to 2 different types of image modalities. We employ ultrasound and MRI images to apply the LESI method to ATAA. The extensional stiffness distribution using ultrasound images and using MRI are demonstrated.

---

Chapter

1

## State of the art

### Contents

1.1	Introduction . . . . .	2
1.2	The vascular system . . . . .	2
1.3	Cardiac Cycle . . . . .	3
1.4	Aorta . . . . .	4
1.5	Arterial Histology . . . . .	5
1.6	Mechanical behavior of arterial walls . . . . .	7
1.6.1	Nonlinearity and hyperelasticity . . . . .	8
1.6.2	Incompressibility . . . . .	8
1.6.3	Anisotropy . . . . .	8
1.6.4	Axial stretch and Residual stresses . . . . .	8
1.6.5	Twisting and shear deformation . . . . .	9
1.7	Vascular disease . . . . .	9
1.8	Aortic dissection and rupture . . . . .	9
1.9	Physiopathology of ATAA . . . . .	10
1.10	Symptoms and causes of ATAA . . . . .	11
1.11	Major factors in ATAA development . . . . .	12
1.11.1	Effects of aging . . . . .	12
1.11.2	Marfan syndrome . . . . .	13
1.11.3	Hypertension . . . . .	13
1.12	Diagnosis . . . . .	13
1.13	Treatments . . . . .	15
1.14	Issues posed by current risk criterion (diameter) . . . . .	16
1.15	Biomechanical factors instead of current risk criterion (diameter) . . . . .	17
1.16	Wall stress analysis of ATAA . . . . .	17
1.17	Wall strain analysis of ATAA . . . . .	18
1.18	Mechanical properties of ATAA . . . . .	19
1.19	Rupture risk indicator . . . . .	20
1.20	Inverse method . . . . .	21
1.21	Conclusion . . . . .	22

## 1.1 Introduction

This chapter is dedicated to the state of the art about biomechanical properties of the aorta preceded by general background on aortic anatomy, physiology and histology. Thoracic aortic aneurysms will be introduced and discussed as well. Finally a review of the literature about the prediction of aneurysm rupture risks will be provided.

## 1.2 The vascular system

The vascular system, also called the circulatory system, consists of a large number of vessels permitting the movement of blood through the body. To maintain homeostasis in all the organs, the blood vessels carry blood through the body, delivering oxygen and nutrients (e.g. vitamins and minerals) to the tissues and organs and removing cellular waste products [119]. Systemic circulation carries oxygenated blood away from the heart to all over the body and returns deoxygenated blood back to the heart. The vessels involved in systemic circulation include:

1. Arteries; blood vessels carrying oxygenated blood away from the heart to the body (Fig. 1.1-a).
2. Veins; blood vessels carrying blood from the body back into the heart (Fig. 1.1-b).
3. Capillaries; the smallest blood vessels between arteries and veins distributing oxygen-rich blood to the body.

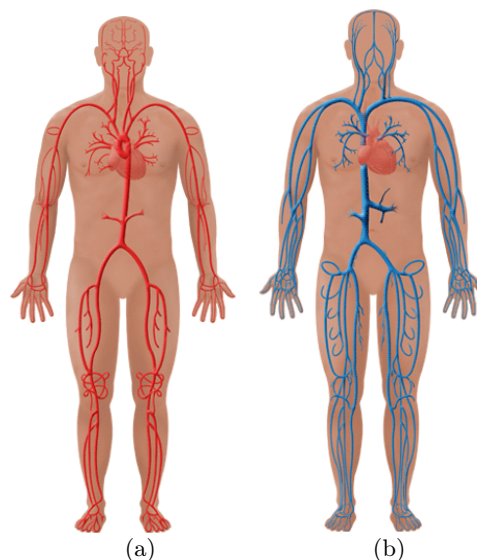


Figure 1.1: Circulatory vascular system including a- arteries and b- venous [5].

The cardiovascular system is composed of the heart, blood vessels and the blood (Fig. 1.2). In a nutshell, the heart is the pump and the blood vessels are the delivery routes. The main function of the cardiovascular system is to maintain the blood flow in the whole body, as this



is essential to survive. Veins contain a low oxygen concentration (as it has been taken out by the body) and high carbon dioxide concentration (as the body has unloaded it back into the blood). All the veins coming from the lower and middle body converge into a large vein named vena cava (VC). The VC drains into the right atrium of the heart pumping blood into the right ventricle. Then the right ventricle pumps blood to the pulmonary trunk, through the pulmonary arteries and into the lungs. In the lungs the blood takes up oxygen that we breathe in and gets rid of carbon dioxide, which we breathe out. Finally, the blood in the pulmonary veins are rich in oxygen to be consumed by the body again. Blood travels from the lungs into the left atrium and then is pumped into the left ventricle. The left ventricle then pumps this oxygen-rich blood out into the aorta which then is distributed to the rest of the body through other arteries.

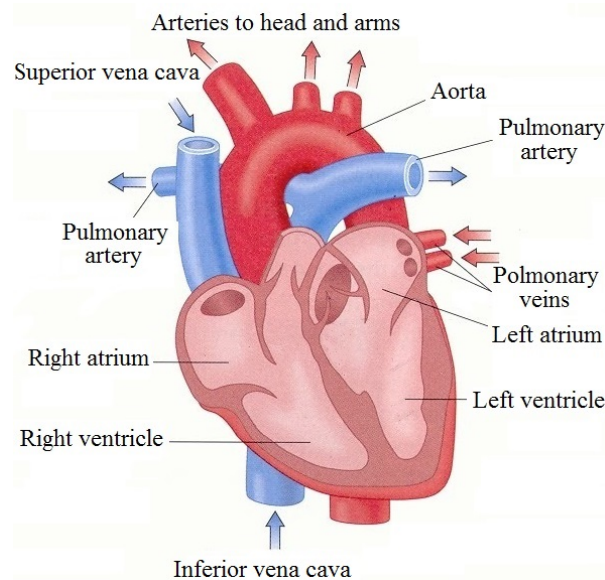


Figure 1.2: Cardiovascular system including four different chambers of the heart and its main arteries and veins [4].

### 1.3 Cardiac Cycle

The cardiac cycle is the sequence of events occurring in one beat of the heart. The pumping phase of the cycle, named systole, occurs when the heart muscle contracts while the expansion phase, named diastole, takes place when the heart muscle relaxes. In a healthy state, for a typical heart rate of  $\sim 75$  beats per minute (bpm), the entire cardiac cycle normally takes place in less than one second. For a total time of 0.8 s (a typical cardiac cycle) 0.3 s is for ventricular systole (contraction) during which the blood is pumped to all body systems from the two ventricles and 0.5 s is for diastole (dilation) during which the four chambers of the heart are refilled to complete the entire cycle. In normal resting state, adults have a maximum blood pressure (BP) during systolic phase of  $\sim 120$  mmHg ( $\sim 16$  kPa), and a minimum BP in the diastolic phase of  $\sim 80$  mmHg ( $\sim 10$  kPa). The normal blood pressure fluctuation in the

aorta is shown in Fig. 1.3.

At the beginning of the cardiac cycle, both atria and ventricles are at diastolic pressure. At this

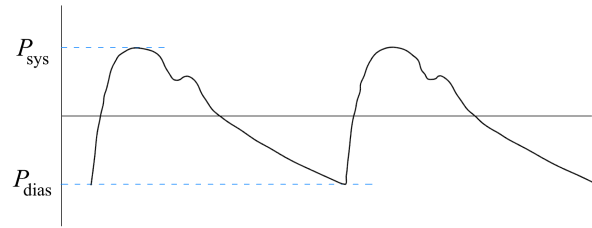


Figure 1.3: Normal blood pressure fluctuation in the aorta.  $P_{\text{dias}}$  and  $P_{\text{sys}}$  are diastolic and systolic pressures, respectively.

time, all the chambers of the heart are relaxed and receive blood, opening the atrioventricular valves. Following this phase, in atrial systole, the right and left atria contract simultaneously and drain blood into the right and left ventricles, respectively. The next phase is ventricular systole during which the left and right ventricles contract simultaneously and pump blood into the aorta and pulmonary trunk, respectively. In ventricular systole, the atria are relaxed and receive blood. Afterwards, the ventricles relax during ventricular diastole, and the semilunar valves close to stop the blood from returning into the ventricles from the aorta and pulmonary trunk. The atria and ventricles are in diastole again and the cycle is completed.

## 1.4 Aorta

The aorta is the main artery in the body which carries oxygen-rich blood to all the body through the systemic circulatory system. It is the largest artery, at about 25 mm in diameter, and also has the thickest walls of any blood vessel in the body. The aorta ascends superiorly from the left ventricle of the heart (ascending aorta), arches over the heart (aortic arch) to the back and to the left, and descends inferiorly behind the heart just anterior to the spinal column.

The ascending aorta starts from the aortic valve in the left ventricle of the heart and twists around the pulmonary trunk. It is noteworthy that, at the origin of the ascending aorta, the lumen contains three small pockets between the wall of the aorta and the cusps of the aortic valve (namely aortic sinuses). The left aortic sinus contains the origin of the left coronary artery while the right aortic sinus contains the origin of the right coronary artery. The posterior aortic sinus does not feed a coronary artery. For this reason, the left, right and posterior aortic sinuses are respectively named left-, right- and non-coronary sinuses. They are shown in Fig. 1.4. The coronary arteries transfer blood to the surface of the heart so that it has oxygen and nutrients to keep beating. The second portion of the aorta, the aortic arch, bifurcates into three major arteries:

1. The brachiocephalic trunk
2. The left common carotid artery

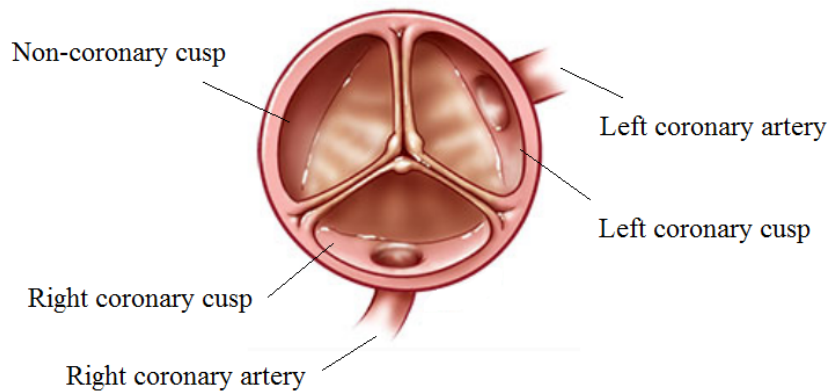


Figure 1.4: Anatomy of the aortic valve [59].

### 3. The left subclavian artery

The brachiocephalic trunk provides blood of the right arm and right side of the head, including the brain. The left common carotid artery supplies blood of the left side of the head including the brain. Finally, the left subclavian artery carries blood to the left arm.

The descending aorta carries blood through the thoracic and abdominal cavities of the body until it splits into the left and right common iliac arteries, which supply blood to the legs. The descending aorta is divided into two sections: the thoracic aorta and abdominal aorta (after the aorta passes through the diaphragm). The abdominal aorta branches off into many smaller arteries that supply blood to the major abdominal organs. Figs. 1.5 and 1.6 illustrate the different regions and bifurcations of the human aorta.

## 1.5 Arterial Histology

The structure of an arterial wall is composed of three distinct layers, namely the intima (tunica intima), the media (tunica media) and the adventitia (tunica externa). A healthy elastic artery is shown in Fig. 1.7 with its three layers. Arteries exhibit a mechanical response, that is influenced by the composition of the layers. Below, we discuss the constitutive and mechanical properties of the three layers of arterial walls.

### 1. Intima

It is the innermost layer of the arterial wall; it is composed of one layer of endothelial cells lining the arterial wall. The endothelial cells are in direct contact with the blood flow so that they mostly resist shear stress imposed by the blood flow. Moreover, intima consists of a subendothelial layer whose thickness changes with age, topography and disease [74].

### 2. Media

It is the middle layer of the arterial wall, much thicker than the intima, and composed of a complex three-dimensional network of elastin, collagen fibrils and smooth muscle

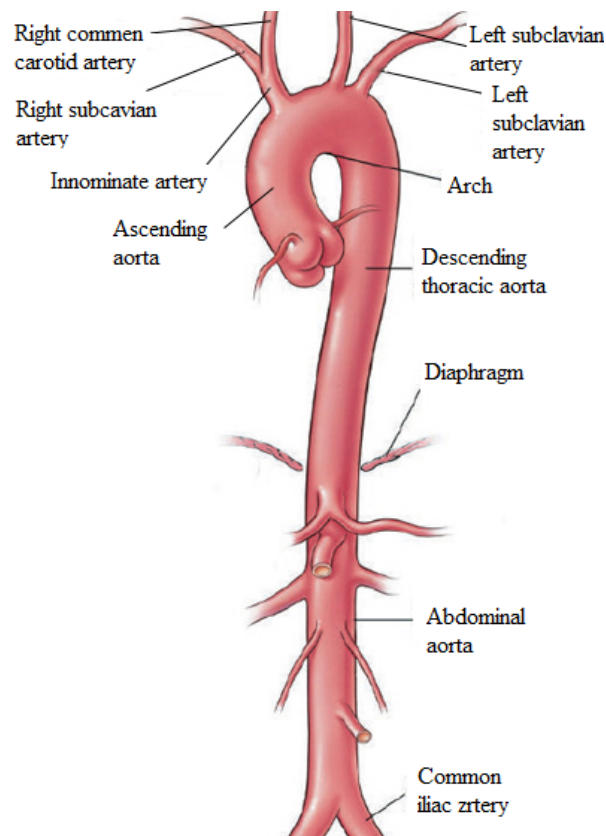


Figure 1.5: Main bifurcations of the human aorta [7].

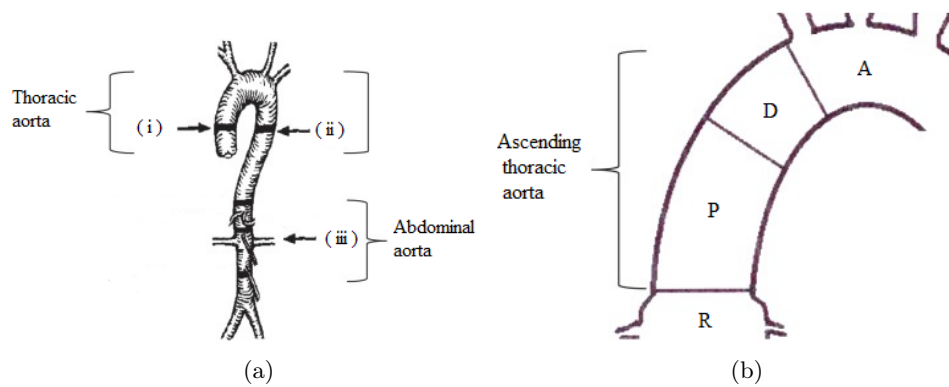


Figure 1.6: a- Different regions of the human aorta including the ascending thoracic (i), the descending thoracic (ii) and abdominal aorta (iii). b- Schematic demonstration of ascending thoracic aorta and aortic arch including the aortic root (R), the proximal ascending thoracic aorta (P), distal ascending thoracic aorta (D) and arch (A) [139].

cells (SMCs). The media is separated from the intima and adventitia by the internal and external elastic laminae, respectively. The main orientation of the fiber networks in the media is circumferential. Consequently, the circumferential direction shows a stiffer uniaxial response than the longitudinal one [74].

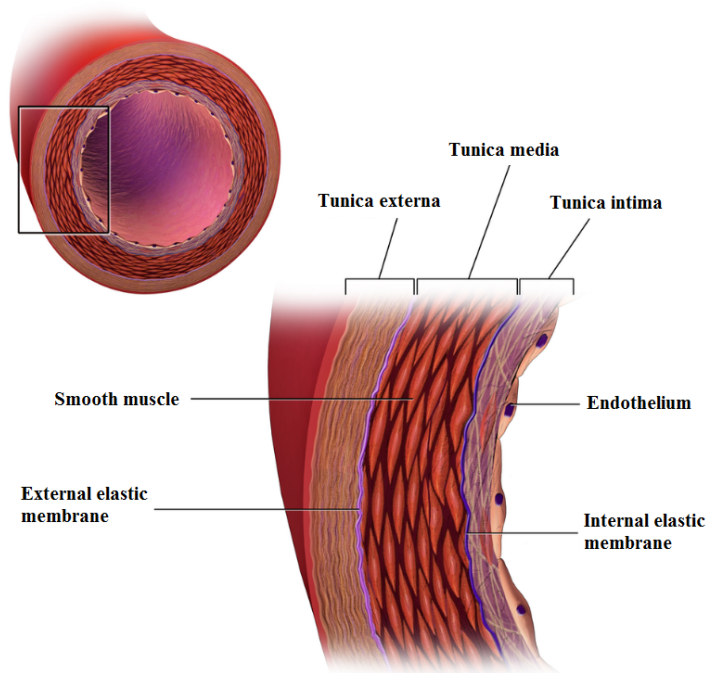


Figure 1.7: Schematic model of the major components of a healthy elastic artery composed of three layers: intima, media, adventitia [133].

### 3. Adventitia

It is the outermost layer of the arterial wall. In addition to thick bundles of collagen fibrils forming a fibrous tissue, it mainly includes histological ground substance and fibroblasts and fibrocytes (cells that produce collagen and elastin). In this layer, the network made of collagen fibers is mostly oriented in the longitudinal direction and the uniaxial mechanical response is stiffer in the longitudinal direction than in the circumferential one [76, 148].

## 1.6 Mechanical behavior of arterial walls

Analysis of each structure and of constituents is needed to understand the material behavior of arteries. Both *in vivo* (physiological state) and *in vitro* (which is outside their normal biological context but close to physiological conditions) tests are beneficial to identify material properties when input data are reliable enough. *In vivo* tests are desirable because the artery is under physiological condition, but they have significant limitation such as the effects of hormones and nervous control. *In vitro* experiments are also performed to measure the complex material response of arterial walls subject to simultaneous cyclic inflation, twist and axial extension to determine, for example, the anisotropy of arterial walls. The most common two-dimensional test is the inflation test of straight arterial tubes shown in [17].

### 1.6.1 Nonlinearity and hyperelasticity

The arterial wall exhibits a nonlinear mechanical response [122]. It is much stiffer under large stress whereas it can be easily deformed under low stress. This nonlinear response at higher stresses is mostly related to the interactions between wavy and collagen fiber networks and elastin matrix. Most continuum models of arteries taking into account the nonlinear behavior are hyperelastic models.

### 1.6.2 Incompressibility

A major portion of the arterial wall is composed of water [153]. Therefore, as water is incompressible, the volume of the aortic wall tissue does not change under the physiological deformation range and the arterial wall can be considered as an incompressible material. Carew et al. [28] immersed arterial sections in water in a closed chamber and observed a volume change of 0.165% at a pressure of 181 mmHg. Patel et al. [115] demonstrated the incompressibility of arteries experimentally by comparing the resistance of the material to changes in volume. Moreover, incompressibility of the human arterial wall was verified by Girerd et al [26] by studying different types and sizes of arteries. They measured the wall thickness and internal diameter using an ultrasonic echo-tracking device. The cross-sectional region of the arterial wall remained unchanged under different strain levels. For an incompressible material subjected to orthogonal stretches, any strain in the third direction can be calculated from the changes in the other two directions by considering the incompressible condition. Therefore, one can determine the mechanical properties of three-dimensional specimens from two-dimensional tests [92].

### 1.6.3 Anisotropy

According to some basic information about the anisotropy of artery provided by [71], uniaxial extensional tests on the arteries are not enough to characterize the anisotropic property of arterial walls. Several studies confirmed that the arterial tissue is anisotropic [114,140], confirming that its elastic properties are not identical in all directions. For example, Dobrin et al. [42] showed that, by assuming isotropy, the circumferential elastic modulus was overestimated by 17% at a pressure of 80 mmHg.

### 1.6.4 Axial stretch and Residual stresses

When an artery is excised from the body it reaches a state without pressure and any longitudinal forces. However, it does not reach a stress free state because longitudinal and circumferential residual stresses remain in the arterial segment. They result from tissue growth and adaptation to their mechanical environment during deposition and development [27,100]. The existence of residual stresses was demonstrated by Vaishnav et al. [141]. This effect is observed from the opening angle introduced by a radial cut of an unloaded ring of artery [58] during which the artery opens by itself. In the absence of longitudinal forces and intravascular and extravascular pressures, an arterial segment also exhibits a shortening when excised from the body [74,91].

This phenomenon shows the existence of a longitudinal pre-stress exerted by the surrounding tissue.

### 1.6.5 Twisting and shear deformation

Due to twisting action of the heart, the aortic arch and the upper part of the thoracic aorta experience some cyclic twisting and shear deformations [147]. On the other hand, the outside of the blood vessels is tethered to the surrounding tissues while their luminal surface is subjected to hemodynamic forces such as pressure and wall shear stress.

## 1.7 Vascular disease

Any disorder in blood vessels can be considered as a vascular disease. Vascular diseases generally affect the arteries and veins by weakening blood vessels, blocking blood flow or/and damaging the heart valves. Other organs may in turn be damaged by vascular disease, for example due to a decrease or complete blockage of blood flow. Below are some examples of vascular diseases and their effects [108]:

1. Disease of the coronary artery: chest pain, heart attack
2. Vascular disease of the great vessels: aortic aneurysm (a bulging and weakened region in the wall of a vessel) and coarctation (narrowing of the aorta).
3. Thoracic vascular disease: thoracic aortic aneurysm (a bulging and weakened region in the wall of a vessel).
4. Abdominal vascular disease: abdominal aortic aneurysm (a bulging and weakened region in the wall of a vessel).

## 1.8 Aortic dissection and rupture

An aortic dissection is a serious condition initiated by a tear in the intima of the aorta. Blood enters the media at the point of the tear because of the high pressures in the aorta and causes the tear to expand. It may extend proximally (closer to the heart) or distally (away from the heart) or both. The blood starts moving through the media, creating a false lumen. The majority of aortic dissections appear with an intimal rupture in the ascending aorta, the aortic arch, or distal to the ligamentum arteriosum in the descending thoracic aorta. As blood flows down the false lumen, it may cause secondary tears in the intima, through which the blood can re-enter the lumen in other locations of the aorta [35]. Therefore, blood flows through the tear, causing the inner and middle layers of the aorta to separate (dissect) as shown in Fig. 1.8. If the blood-filled channel ruptures outward the aortic wall in the false lumen, the aortic dissection is often considered fatal. This condition often occurs in men in their 60s and

70s. Aortic rupture is due to the weakening of the aortic wall leading to tearing of the aortic wall, allowing blood to escape outside the confinement of the aorta (see Fig. 1.9).

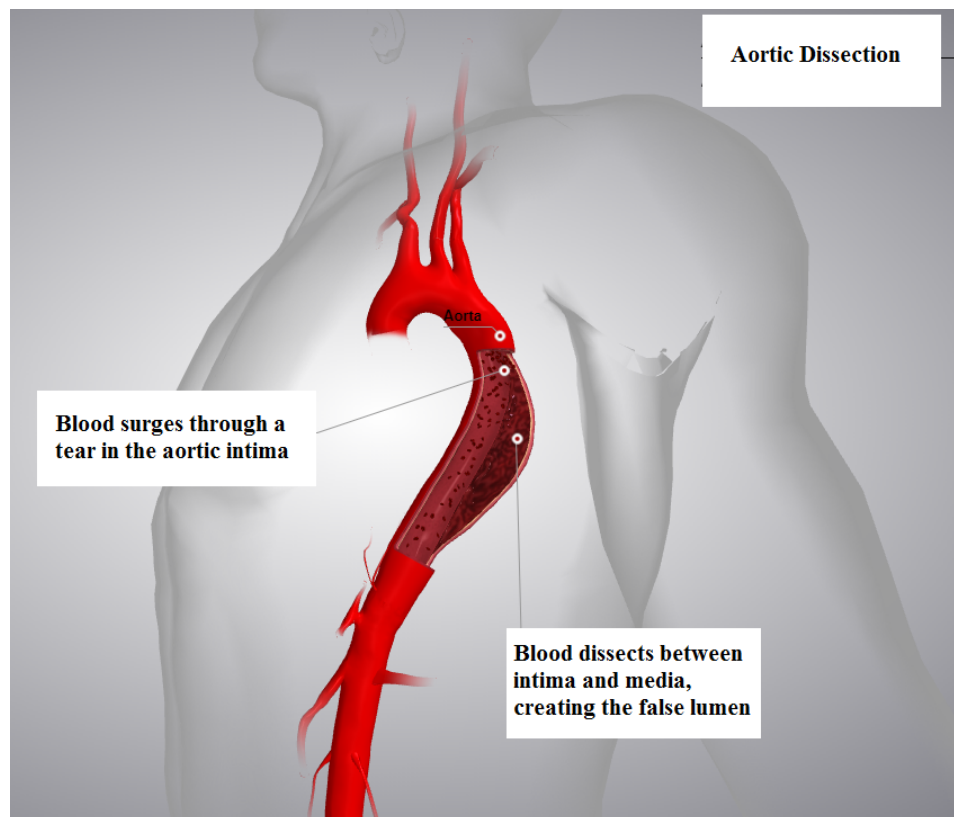


Figure 1.8: Aortic dissection in which the inner layer of the aorta tears and blood enter in between intima and media causing delamination [51].

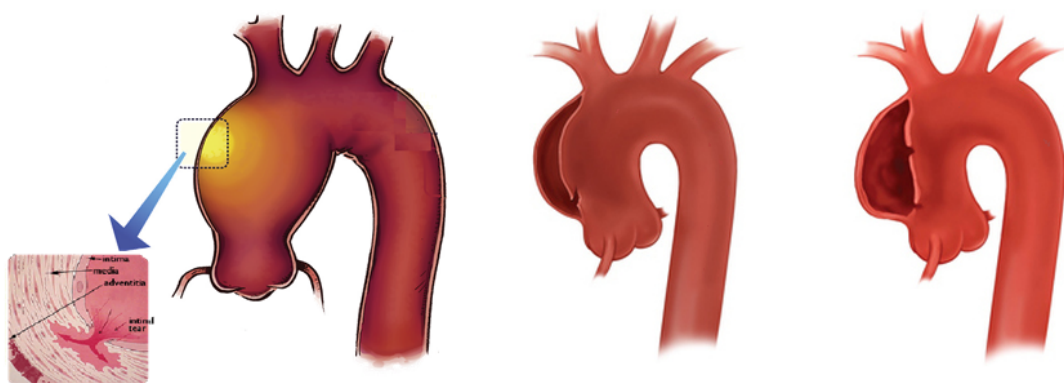


Figure 1.9: Aortic rupture due to dissection of the aorta [6].

## 1.9 Physiopathology of ATAA

An aneurysm occurs when an artery weakens and exhibits an abnormal bulge. This bulge can rupture the aorta and cause internal bleeding ending with death. Some aortic aneurysms may



burst while others may be stable but cause problems such as heart attacks, kidney problems and even death [2]. Aortic aneurysms can develop in different parts of the aorta running from the heart, the chest or abdomen. When they occur in the chest they are named thoracic aortic aneurysms (TAA). Aneurysms can occur anywhere in the thoracic aorta, including the ascending aorta near the heart, namely ascending TAA (ATAA), the aortic arch in the curve of the thoracic aorta and the descending aorta in the lower part of the thoracic aorta, namely descending TAA (DTAA). Fig. 1.10 shows an example of ATAA and DTAA. People affected by aortic aneurysms mostly do not have symptoms unless a dissection or rupture happens. If one has a family history of aortic aneurysm, Marfan syndrome or other connective tissue disease, or bicuspid aortic valve (BAV), the physician may recommend regular ultrasound or radiology testing such as computerized tomography (CT) scan or magnetic resonance imaging (MRI) to screen for aortic aneurysm.

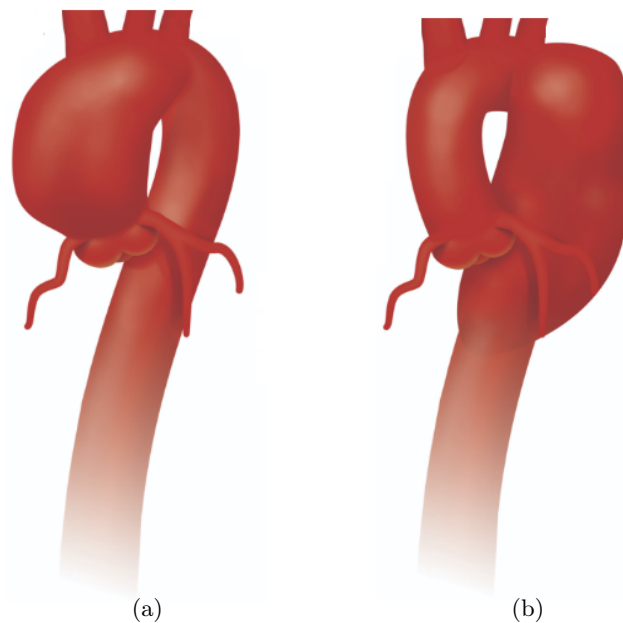


Figure 1.10: Schematic demonstration of a- the ascending thoracic aortic aneurysms and b- the descending thoracic aortic aneurysms (DTAA) [3].

## 1.10 Symptoms and causes of ATAA

Thoracic aortic aneurysms often grow slowly and usually without symptoms, making them difficult to detect. Some aneurysms never rupture or cause evident symptoms. They are often diagnosed by accident, when a CT scan or other screening shows a bulge in the aorta.

As a TAA grows, if symptoms are present, people may notice a pain in the chest, back, jaw, or/and neck as well as hoarseness, cough and shortness of breath. Factors that have an impact on the rupture of aorta are age, hypertension, aortic valve phenotype (bicuspid or tricuspid) or genetic disorders including Marfan syndrome (MFS) and Ehler-Danlos syndrome [44].

MFS is a heritable disorder of connective tissue caused by mutations in the extracellular matrix protein fibrillin-1 which can lead to aortic root aneurysm [67]. Due to the high occurrence of aortic root aneurysm with related aortic dissection risk, the lifespan is often shortened [37]. In the Marfan syndrome, coarctation of the aorta is not a common abnormality, but it is observed more often than expected. [46].

It has been significantly important to study the microstructure of the aortic wall, because alteration in the quantity of elastin and collagen, both of which contribute to elasticity and strength, can change the mechanical properties in aging and disease. It is known that the ascending thoracic aorta (ATA) is susceptible to aneurysm and dissection, having potential haemodynamic effects. Here we will focus on literature reports that specifically characterize and quantify the variation in amount and architecture of elastin and collagen specifically in the ATA due to aging and disease.

## **1.11 Major factors in ATAA development**

Although the exact reason of aortic aneurysms is still partially unknown, several important factors may play prominent roles in aneurysm development including aging and blood vessel diseases in the aorta, such as Marfan syndrome and atherosclerosis. Patients with TAA are at higher risk for aortic dissection if they are subjected to high blood pressure, especially not controlled, smoking, use of cocaine and other stimulants which increase aortic wall stress such as weight lifting, trauma, aortic coarctation and disorders [103]. Other causes of thoracic aortic dissection are pregnancy, polycystic renal disease, chronic use of corticosteroids or immunosuppressant drugs, aortic wall infections and heredity [103]. In the following sections, the most prevalent factors are discussed.

### **1.11.1 Effects of aging**

It has been shown that elastin concentration within the aorta decreases with age, but the elastin content remains unchanged [70]. This is also confirmed by different other studies [50, 106], suggesting that the decrease in elastin concentration is partly due to increase in fraction of the other components, such as collagen [64, 123, 125], while the total elastin content remains unchanged [93]. Moreover, the growth and remodeling of the human thoracic aorta occurring by aging are associated with fragmentation (degradation) of elastin fibres [135]. Fragmentation is also observed in calcified thoracic aortas with atherosclerotic lesions [132]. In particular, in the wall of ATA, the elastin concentration (% per mg of sample, dry weight) was reported to gradually decrease by 36% from birth to 81 years [78]. In another study of a cohort of patients, the same author showed a decrease in elastin concentration by 33% between 20 and 90 years [77].

Numerous studies [64, 123, 125] reported an increase in the content of aortic wall collagen with aging. Moreover, [50] showed that collagen concentration increases from 20% to 30.5% and [87] reported an increase from 19.9% to 25.5% with aging. However, the increase in collagen content

can be layer-specific and occurs nonlinearly with age in the case of the thoracic aorta. It is approximately constant for individuals younger than 45 and increases slowly thereafter [106]. In addition, the structure of collagen fibres changes during life with increasing by irregularly arranged fibres in the media of the thoracic aorta [135]. In summary, studies on collagen in the human aorta for different ages show a significant correlation of collagen content with age [9] and a considerable rise in the number of hydroxyproline residues (indicative of amount of collagen) after age 50 [69].

### 1.11.2 Marfan syndrome

In the aorta of MFS patients, there is elastin deficiency in cross-linking residues, decreasing the content of elastin by  $\sim 50\%$  [8, 117]. The degradation of elastin and decrease in cross-linking could lead to aneurysm in MFS patients because the elastin loss may lead to a release of high compressive prestresses within the aortic wall and subsequently end in the enlargement of the aortic diameter [56]. Moreover, analysis of the elastin in the media of dissecting aortic aneurysms showed a decrease in the elastin concentration in dissection sites of TAA [149]. Particularly, in dissected ATAs, the elastin content is mainly decreased compared with non-dissected ATAs.

The collagen content in aortas in patients with dissecting aortic aneurysm and MFS patients is similar to that in the healthy aorta and collagen does not show structural changes [111, 117]. Despite the consistency of this trend with the thoracic aorta in dissecting aneurysms, collagen concentration decreases but collagen content increases, specifically at dissection sites [149].

### 1.11.3 Hypertension

Hypertension or high blood pressure is a condition when blood flows through the vessels with excessive pressure. It is defined by a systolic blood pressure greater than 140/90 mmHg over a number of weeks. The short-term effect of an artery to a high blood pressure is a distension of the arterial wall and a decrease in its thickness. The circumferential wall stress is then increased. To recover the initial circumferential stress, an increase in internal diameter and thickening of the media are observed mainly by hypertrophy and hyperplasia of SMCs, and by an increase in the synthesis of collagen, elastin and proteoglycans [31, 63].

## 1.12 Diagnosis

The decision for surgical intervention on a patient with an TAA depends on a reliable and reproducible diagnostic method. If a TAA is suspected, the physician may order the following imaging modalities to measure and characterize the ascending thoracic aorta [49].

1. Transthoracic echocardiography (TTE) is a method of screening and monitoring. It uses ultrasonic (above the range of human hearing) sound waves that are produced and detected within an ultrasound transducer. Even though the images of mid and distal segments of the ascending aorta provided by TTE are not sufficient, it is a recommended

imaging technique for monitoring patients affected by root or proximal aortic aneurysm and for follow-up. In cases where echocardiography shows a dilated aorta, or where the quality of the visualization is poor, computed tomography (CT) or magnetic resonance imaging (MRI) is recommended.

Ultrasound elastography has been highlighted in recent years for noninvasive estimation of tissue mechanical properties. It takes advantage of changed soft tissue elasticity in diverse pathologies to provide quantitative and qualitative data useful for diagnostic purposes. Therefore, elastography methods can be used to differentiate affected tissue from normal tissue for diagnostic applications [127].

2. A CT scanner sends X-ray beams through the body and recognize different levels of density and tissues inside a solid organ, and can yield detailed information about the body by constructing cross-sectional images. Advances in CT scanning include increased patient comfort, faster scanning times and higher resolution images. However, in younger patients the cumulative radiation dose from follow-up examinations could be harmful for the patient [57]. Fig. 1.11 shows an image of aorta acquired by CT scan.
3. MRI is an increasingly employed noninvasive imaging modality. MRI scans employ powerful magnetic fields and radio frequency pulses to provide detailed pictures of organs, soft tissues, bone and other body structures. Differences between normal and abnormal tissue are clearer on an MRI image than a CT scan. Although there is no radiation involved in an MRI scan, it can be a noisy exam and takes more time than a transesophageal echocardiography. In addition, it provides good visualization of the ascending aorta but it is stressful for the patient.

Advantages and disadvantages of ultrasound, CT scan and MRI imaging have been summarized in Table 1.1.

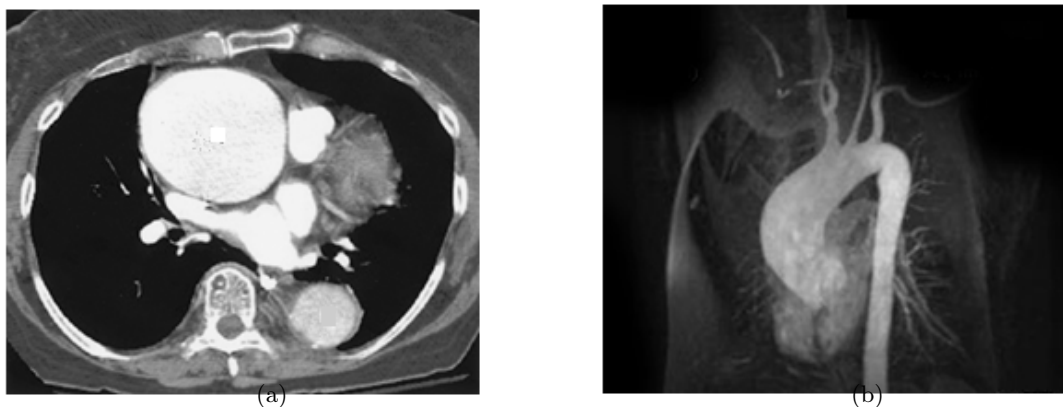


Figure 1.11: CT scan images of aorta, a- transversal b- frontal planes.

Table 1.1: Advantages and disadvantages of different imaging modalities [49].

	Ultrasound	CT-scan	MRI
Advantages	Widely available	Rapidly available	Nearly 100% specific and sensitive
	No radiation exposure	Nearly 100% specific and sensitive	No radiation exposure
	Enables the study of valve function	Can diagnose dissection	Can visualize entire aorta
	measurement of wall thickness	Can visualize entire aorta	
Disadvantages	Time consuming compared to CT-scan (center dependent)	Radiation exposure	Time consuming compared to CT-scan
	Arch not visualized	Contrast nephropathy	Many contraindications
	Inter-observer variability		Contraindicated in advanced renal failure
	Difficulty visualizing portions distal to the sinotubular junction		More expensive

## 1.13 Treatments

Depending on the size, rate of growth, location of an aneurysm and the overall health of the patient, the decision on how to treat a thoracic aneurysm is taken. If a thoracic aneurysm is small and no symptoms are observed, a watchful waiting is recommended which includes [134]:

1. Monitoring of the aneurysm with CT or MRI scans every 6 months or one year
2. Controlling high blood pressure and lowering the pressure on the region of the aneurysm.
3. Limitation of some physical activities, for example carrying heavy objects should be avoided due to increased pressure on the aorta.

The risk of rupture increases when the aneurysm is larger than the normal diameter of the aorta. The decision to treat a thoracic aneurysm with surgery is indicated based on following factors:

1. The presence of symptoms such as chest, back, jaw and neck pain.

2. When the aneurysm is growing fast (more than 1 cm per year).
3. Signs of an aortic dissection such as sudden dissection pain in the chest or back.
4. The age of the patient and the patient's medical condition.

Nowadays, the decisive criterion for an aneurysm is the greatest vascular diameter. Surgical intervention is indicated when the diameter is greater than 5.5 cm and surgical correction is guided by the aneurysm location. An ATAA surgical repair is schematically shown in Fig. 1.12. For combined aortic valve and ascending aorta replacement, either the valve or the aortic prostheses can be implanted sequentially or a composite graft can be placed.

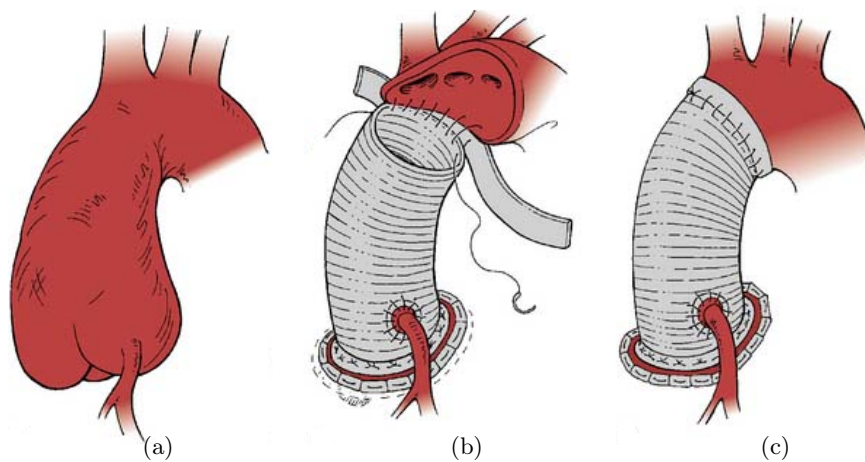


Figure 1.12: Schematic illustration of ATAA replacement and aortic repair [1].

Reproducible measurement of the vascular segment is needed to monitor the diameter growth rate. Descending and thoracoabdominal aneurysms grow on average 1.9-3.4 mm/year while ascending and aortic arch aneurysms grow 0.2-2.8 mm/year. The presence of Marfan syndrome, large aneurysm size, bicuspid aortic valve and distal aneurysm locations were systematically accompanied by fast TAA growth. Moreover, presence of chronic dissection disorder was also considered as risk factor for faster TAA growth [110].

### 1.14 Issues posed by current risk criterion (diameter)

The criterion based on 5.5 cm diameter for surgical intervention is extensively recognized as insufficient. For example, the International registry of 15 Acute Aortic Dissection (IRAD) conveyed that among 591 type "A" aortic dissections, 59% had a diameter below 5.5 cm so the current aortic diameter excludes approximately 50% of patients with an acute type A aortic dissection from preventive replacement of the ascending aorta. Therefore aortic rupture cannot be reliably predicted by measuring the ATAA diameter and there is a need for more reliable risk indicators. On the other hand, diameters smaller than 5.5 cm still have a 5-10% chance of rupture while large aneurysms that are resected might have remained stable for the patient's

lifetime. The important question remains: is a diameter of 5.5 cm the right criterion for surgery, or must we move to a smaller diameter? Several medical centers that are specialized in aortic surgery have already operated ascending aortic aneurysms  $<5.0$  cm in diameter, and it is time to re-evaluate the guidelines [86].

### 1.15 Biomechanical factors instead of current risk criterion (diameter)

Several studies of AAA suggest that biomechanical factors may reliably predict the risk of rupture better than the diameter criterion. A noninvasive method was developed by [61] for evaluation of the rupture potential of AAAs using patient-specific analysis. They calculated the ratio of locally acting wall stress to strength as rupture potential index of the AAA. Their results suggest that the peak rupture potential index may be better suited to identify AAAs at high risk of rupture than maximum diameter or peak wall stress alone. In another study on AAA, the diameter and peak wall stress in some patients were investigated. Two protocols were followed in which some patients underwent an elective repair within 1 year, and others were underwent an emergency repair. Significant differences were found for initial diameter and initial peak wall stress, but peak wall stress showed to better differentiate patients who later needed emergent repair [54]. Based on these studies and due to the insufficiency of the current risk criterion (diameter), researchers have developed various rupture risk indicators for ATAA rupture.

### 1.16 Wall stress analysis of ATAA

It is widely acknowledged that the rupture of ATAA occurs when the stress applied to the aortic wall reaches the rupture stress. Therefore, some studies focused on wall stresses in ATAA as a biomechanical criterion for the risk of dissection. Finite element analyses were implemented by [55] to compare peak wall stresses in patients with 5.0 cm diameter versus  $<5.0$  cm, demonstrating significantly greater wall stresses in the larger versus smaller aneurysms in both circumferential and longitudinal directions. However, a poor correlation was found between peak wall stresses in both circumferential and longitudinal directions with ATAA diameter. These data show that the peak ATAA wall stresses may be useful as a biomechanical marker for the risk of rupture.

Accurate determination of patient-specific wall stress needs models with a three-dimensional geometry, including zero-pressure and residual stresses, precise measurement of wall local thickness and finding proper material properties to fit model parameters. Krishnan et al [90] employed a zero-pressure configuration based on the geometry reconstructed from in vivo images to calculate aortic wall stress. The first and second principal wall stresses were compared when a zero-pressure and systemic-pressure geometries were employed in FE models. It was concluded that peak principal stresses using zero-pressure geometry are greater than those ones

obtained without the zero-stress geometries. This was also confirmed by Mousavi et al. [104] using a FEM based on the constrained mixture theory (CMT).

Moreover, wall stresses were also compared for ATAA with bicuspid and tricuspid aortic valve (TAV) [152], showing greater circumferential and longitudinal stresses in bicuspid aortic valves. Peak wall stress did not correlate with bicuspid aortic diameter, confirming that the diameter alone may be a poor predictor of the dissection risk. Their results also highlighted the need for patient-specific wall stress analysis for rupture risk prediction.

Smoljkic et al [128] characterized the geometrical and mechanical properties of ATAA. Their findings acknowledged that mechanical or geometrical information cannot provide sufficient rupture risk assessment. The ratio of physiological to ultimate wall stress appeared as more promising parameter. However, wall stress evaluation suffered from unreliability in wall thickness measurement between patients and between measurement methods.

Analysis of wall shear stress parameters showed a high and locally varying wall shear stress on the outer aortic wall and high temporal oscillations in wall shear stress on either left or right side of the aorta. These results may explain the asymmetric dilatation observed in ATAA. A hypertension simulation showed an increase in wall shear stress upon 44% compared to normal systemic pressure models [121].

Pasta et al [113] developed a method to evaluate and compare the dissection properties of non-aneurysmal and aneurysmal human ascending thoracic aortas from patients with bicuspid aortic valve and normal tricuspid aortic valve morphologies employing biomechanical delamination testing. Following complete delamination of ATAA tissue samples, tensile tests were carried out on each delaminated half to compare their tensile strengths. Results showed that aneurysmal aortas with BAV and TAV have lower delamination properties than non-aneurysmal aorta.

Emerel et al [48] proposed a method to evaluate ascending aortic distensibility using pre-dissection non-invasive imaging. They reported that aortic wall strain and distensibility were decreased while stiffness and longitudinal wall stress were increased. They also found no significant difference in circumferential wall stress patients sustaining type A aortic dissection and healthy cases.

## **1.17 Wall strain analysis of ATAA**

In vivo evaluation of the full-field distribution of wall strain was performed by image analysis of electrocardiographic- (ECG) gated data in patients with ATAA [112]. The results indicated that the aneurysmal ascending aorta of controlled patients was stiffer compared to the healthy one and patients over 55 years old had significantly lower extensibility. In addition, the patient risk (the ratio of in vivo strain to the rupture strain) increased significantly with high systolic blood pressure, old age and higher pressure-strain modulus. Moreover, statistical analysis showed that an increased pressure-strain modulus was a risk criterion for ATAAs with bicuspid aortic valve, suggesting a different mechanism of failure in these patients.



## 1.18 Mechanical properties of ATAA

Over the past decades the biomechanical properties of the aorta have been widely investigated using different methods [15, 38, 81, 89, 109, 146]. Azadani et.al [15] collected ATAA samples from patients undergoing surgical aneurysm repair. Biaxial stretch testing was used to obtain mechanical properties of the tissues. Patient-specific ATAA physiologic stress was estimated using preoperative CT scans. Stiffness of ATAA and ascending aorta tissue were identified at respective physiologic stress. The results demonstrated that physiological stress of ATAA was significantly greater than that of normal controls. Besides, tissue stiffness of ATAAs was significantly greater than that of the ascending aortas. They found a good correlation between tissue stiffness of ATAAs and ATAA diameter but no correlation was found between stiffness of ATAAs and patient age. Moreover, no correlation was found between maximum diameter and physiological stress of ATAA.

Age effects on dilated human ascending aorta were investigated by in vitro measurement of the mechanical properties of human ascending aorta [109]. Specimens were cut from collected tissue obtained from 54 patients undergoing elective aortic graft replacement surgery in different ages and were used for opening angle, biaxial elastic, and uniaxial circumferential strength tests. The opening angle was remarkably greater in older patients compared to younger patients. All biaxial elastic samples showed nonlinear material behavior. At lower strains, rapid increases in circumferential and axial stresses occurred in the group of older patients. Mean strength was significantly lower in old patients in comparison with young patients. These alterations in mechanical properties showed that age may affect the risk of aortic dissection or rupture of enlarged ascending aorta.

Regional and directional differences in the mechanical properties of ATAA were estimated by Iliopoulos et.al [81]. In most samples, circumferential peak elastic modulus and failure stress were significantly higher in all regions and the inner layers of the aortic wall ruptured first. Heterogeneity was found in the mechanical properties of ATAA, in which the longitudinal anterior region was the weakest zone. No correlation was found between failure stress and ATAA diameter or patient age. Failure stress correlated inversely with the wall thickness and directly with peak elastic modulus.

The inhomogeneity of the ATAA at the millimeter scale was demonstrated by Davis et.al [38]. They proposed a combined experimental and computational model employing bulge inflation tests, digital image correlation (DIC) and an inverse membrane approach to estimate the pointwise stress, strain, and hyperelastic properties of the ATAA. The pointwise hyperelastic material properties were estimated on 10 human ATAA samples excised from patients who underwent elective surgical repair of ATAA. They captured the different levels of heterogeneity in the ATAA, from regional to local. They showed that the material properties in the ATAA were heterogeneous at length scales between 1 mm and 1 cm.

Khanafer et.al [89] provided measurements of the elastic modulus of the aortic wall of ATAA for different ranges of physiological and hypertensive pressures. Moreover, they measured pre-

failure stress, taken as the peak stress obtained before sample failure, for each test. 97 fresh samples were obtained from outer and inner curvatures of different aortas excised from  $n = 13$  patients with ATAAs and tested uniaxially in circumferential and longitudinal orientations. The maximum elastic modulus in the inner curvature was significantly higher in the circumferential direction in comparison with the longitudinal. The peak stress indicated direct correlation with maximum elastic modulus and inverse correlation with aortic wall thickness.

Moreover, it was reported that the tensile strength of longitudinal and circumferential ATAA specimens was 29% and 34% less than that of normal tissue, respectively. Maximum tissue stiffness was 72% stiffer for longitudinal ATAA and 44% stiffer for circumferential ATAA than for controlled tissue, respectively [146].

## 1.19 Rupture risk indicator

Martin et al [98] defined a criterion, namely the diameter ratio risk, which is the ratio between the current diameter of the aneurysm to the rupture diameter. They showed that the diameter ratio risk increased significantly with the physiological elastic modulus of the artery. Commonly, rupture risk is also estimated as the ratio between current (or physiological) and ultimate stress. However, wall stress evaluation has uncertainties in wall thickness measurement. Moreover, there is a large variability in ultimate stress between individuals, which prevents obtaining patient-specific values.

Different authors measured geometrical and mechanical properties of ATAA and showed that rupture properties may vary significantly even with tissues having similar elastic properties [30, 43, 44, 128, 146]. In addition, another disadvantage of stress based rupture index is that current stress induced by normal blood pressures is usually far from the ultimate stress. Indeed, rupture is often an accidental event during which there is a sudden rise of pressure and stress in the wall. Even dissections are typically preceded by a specific severe exertional or emotional event [47].

The stretch ratio risk index, as the ratio of the current tissue stretch (under in vivo conditions) and the maximum stretch (at which the tissue ruptures), appears very promising [44], because it is strongly correlated with the local tissue stiffness which can be obtained with the Local Extensional Stiffness Identification (LESI) methodology [52]. However, results showed that there was no correlation between the strength of ATAA samples and their in vivo stiffness.

To examine various criteria for the local failure of AAA, Volokh et al [145] developed an experimental model including a failure description. They analyzed various states of the biaxial tension in the AAA material and assessed the strain energy, the maximum principal stretch and stress, the maximum shear stress and von Mises stress criteria of the local failure. They concluded that the von Mises stress showed a larger variability comparing to the strain energy. It could be interesting to define a rupture risk criterion based on maximum strain energy as it would combine both stress and strain contributions, but apart from Volokh et al, nobody really investigated this way further.

To understand the biaxial rupture of ATAAs, Duprey et.al [44] developed a methodology based on bulge inflation and full-field optical measurements. They reviewed the failure properties (maximum stress, maximum stretch) obtained by bulge inflation testing on a cohort of patients and compared them with failure properties obtained from uniaxial tension. Therefore, they also defined a rupture risk criterion based on the extensibility of the tissue showing that this rupture risk was strongly correlated with the physiological elastic modulus of the aorta, independent of the ATAA diameter, age or the aortic valve phenotype of the patient.

Trabelsi et al [138] developed a method for the in vivo identification of the global stiffness of an aortic segment based on the estimation of distensibility using gated CT scans and pressures. Following the methodology of [44] they also employed bulge inflation tests on excised tissue segments of ATAA. However, only moderate correlation was found between the global in vivo stiffness values and the local stretch based rupture risk criterion.

## 1.20 Inverse method

An inverse problem is the process of calculating parameters from a set of observations in which we cannot directly identify these parameters in the lab. In other words the "inverse problem" uses the results of actual observations to derive the values of the parameters that characterize the system under investigation.

Inverse methods are widely used to characterize material parameters. For example, our focus is placed on the in vitro evaluation of hyperelastic parameters using full-field data collected by digital image correlation systems [14]. It is employed for a membrane-like tissue through bulge inflation tests of pieces of aortic aneurysms. An inverse method was developed based on the principle of virtual power to estimate the regional distribution of material parameters for general applications. Characterizing stress-strain response using full-field measurements, the stress was determined at every Gauss point using inverse membrane analysis. The local material property were estimated by fitting the local stress-strain response to a hyperelastic surface energy density [14]. Moreover, an inverse method was developed by [95] to compute aortic wall stress under in vivo loads. Their objective was to evaluate the material parameters by minimizing the objective function. Therefore, they computed a true stress field from the in vivo geometries and loading conditions to establish an objective function based on the true stress fields, constitutive equations and deformation relations. In another inverse approach the local distribution of residual strains and stresses was estimated using a finite element model, from digital image correlation measurements on a sample of excised tissue [16].

Inverse methods have been implemented in other biomechanical applications as well. For example Zhang et al [154] determined the mechanical properties of the iris in vivo using an inverse method. Pressures in the anterior and posterior chambers and the displacement of the characteristic points on the surface of the iris were calculated. Using ultrasonic images, a finite element model of the anterior chamber was implemented before perfusion. To do so, an algorithm was employed to determine the material parameters of the iris by minimizing the

difference between the results from the finite element model and the experimental results.

## 1.21 Conclusion

As pointed in the state of the art, many studies introduced different new mechanical factors to estimate the rupture risk of ATAA to increase the decision reliability of surgeons. It was shown that the diameter is not a sufficient indicator of rupture risk, and that criteria based on peak wall stress estimation suffer from uncertainties in wall thickness and strength. However, a stretch ratio risk index demonstrated a good correlation with stiffness. Since most studies previously discussed were in vitro, the question is could we non invasively identify the in vivo local stiffness of ATAA to estimate a reliable rupture risk criterion?

We demonstrate in this thesis that the noninvasive identification of local elastic properties of ATAA is highly important and possible, provided that images can be acquired with a sufficient temporal and spatial resolution, and provided that a robust inverse method is available to process these datasets. Most of the thesis is devoted to developing and validating this methodology.

# Estimating aortic strain field using a pair of images and a mesh morphing approach

## Résumé

La déformation de la paroi des anévrismes de l'aorte thoracique ascendante (AATAs) peut constituer un biomarqueur important. L'objectif de cette étude est d'évaluer et d'appliquer des techniques de morphing et de maillage afin de faciliter le processus de reconstruction de la déformation. Après la segmentation des scanners de tomodensitométrie, la géométrie à chaque phase du cycle cardiaque (différents pas de temps tout au long du cycle cardiaque) est obtenue sous forme de fichiers STL. En supposant un ensemble de nœuds attachés aux mêmes points matériels, le maillage de référence est transformé en un maillage cible à l'aide de deux méthodologies différentes. Dans la première méthodologie (méthode I), le logiciel Vascular Modeling Toolkit (VMTK) [11] est utilisée pour obtenir les coordonnées paramétriques de tous les nœuds du fichier STL. La méthode est basée sur la décomposition de la surface en branches et en mappant chaque branche sur les coordonnées paramétriques du modèle. Le morphing de maillage par VMTK est un processus qui prend du temps. Par conséquent, pour réduire le temps de travail, nous considérons une seconde méthodologie (méthode II) se basant sur un logiciel dédié appelé Radial Basis Functions (RBFs) morph<sup>®</sup>. Il permet une reconstruction automatique des champs de déplacement sur l'aorte entre une géométrie de référence et une cible. Les RBF sont une classe de fonctions d'interpolation mathématique permettant de transformer un maillage en modèle. Enfin, nous comparons les champs de déplacement et de déformation obtenus avec la méthode I à ceux obtenus avec la méthode II. Bien que la méthode II soit une méthode efficace préservant la topologie du maillage, l'analyse quantitative de la validation numérique montre un écart très supérieur à celui de la méthode I. Nous avons finalement décidé d'utiliser la méthode I pour la reconstruction des cartes de déformation dans l'ATAA.

## Contents

---

<b>2.1</b>	<b>Abstract . . . . .</b>	<b>25</b>
<b>2.2</b>	<b>Introduction . . . . .</b>	<b>25</b>
<b>2.3</b>	<b>Theory . . . . .</b>	<b>27</b>
2.3.1	Method I . . . . .	28
2.3.2	Method II . . . . .	28
<b>2.4</b>	<b>Materials and methods . . . . .</b>	<b>28</b>
2.4.1	Data acquisition . . . . .	28
2.4.2	Computational implementation . . . . .	29
2.4.3	Numerical verification . . . . .	35
<b>2.5</b>	<b>Results . . . . .</b>	<b>37</b>
2.5.1	Method I . . . . .	38
2.5.2	Method II . . . . .	38
<b>2.6</b>	<b>Discussion and conclusion . . . . .</b>	<b>40</b>

---

## 2.1 Abstract

Wall strain across ascending thoracic aortic aneurysms (ATAAs) can be an important biomarker. The objective of this study is to evaluate and to apply mesh morphing and mapping techniques to facilitate the process of strain reconstruction. After segmentation of gated computed tomography (CT) scans, the geometry at each phase of a cardiac cycle (different time steps throughout the cardiac cycle) is obtained as STL files. Assuming a set of nodes attached to the same material points, the reference mesh is morphed onto a target surface using two different methodologies. In the first methodology (method I), the Vascular Modeling Toolkit (VMTK) [11] is used to obtain the parametric coordinates of all the nodes of the STL files. The method is based on the decomposition of the surface into existing branches and mapping each branch onto template parametric coordinates. Mesh morphing by VMTK is a time consuming process, therefore to reduce the labor time we consider a second methodology (method II) which relies on a dedicated software named Radial Basis Functions (RBFs) morph<sup>®</sup>. It permits automatic reconstruction of displacement fields across the aorta between a reference and a target geometry. RBFs are a class of mathematical interpolation functions to perform mesh morphing of a computational model. Finally we compare the displacement and strain fields obtained from method I to those obtained from method II. Although method II is a strong method preserving the mesh topology, quantitative analysis of numerical validation show a root mean square deviation of 0.1 for the first principal strain between finite element analysis (FEA) and method II while this value is 0.0064 for method I. Consequently, we eventually decided to use method I for the reconstruction of strain maps in ATAAs.

Keywords: Mesh morphing; Reconstruction of strain; RBF morph<sup>®</sup>; VMTK; Finite-elements; Ascending thoracic aortic aneurysms; Cardiac cycle;

## 2.2 Introduction

Cardiovascular diseases are becoming more prevalent in modern societies. In the past years, a lot of emphasis has been placed on the investigation of these diseases. It has been demonstrated that biomechanical factors may be used to improve the treatment strategies and the quality of surgical interventions [44, 55, 90, 112, 138, 152]. For example, it has been shown that rupture occurs when the stretch applied to ascending thoracic aortic aneurysms (ATAAs) reaches the maximum extensibility of the tissue and that this maximum extensibility correlates strongly with the ATAA stiffness [44]. In addition, the ratio of in vivo strain to the ruptured one, quantifying the patient rupture risk, increases extensively with age, higher systolic blood pressure and higher pressure-strain modulus. Therefore, the approach proposed by [112] indicates that the in vivo evaluation of the aortic wall strain is promising as it could be employed for the development of a rupture criterion based on the aortic aneurysm extensibility.

Reconstruction of in vivo strains requires the measurement of ATAA displacements. Digital image correlation (DIC) is a technique of displacement measurement for in vitro applications [13, 38, 39]. Zhou et al. [155] developed a method in which the images of a sample were

captured at unloaded and various loaded states. Small squares were defined on the first image, forming a mesh to calculate 2D strain fields. They derived the position of each square in the deformed configuration using an image correlation algorithm. The motion of each square was then tracked, image-by-image, reconstructing displacement fields which could then be used to derive strains. Researchers always attempted to find an automatic and fast method for in vivo measurement of displacements to reduce the labor time of in vivo strain reconstruction. For instance, Pasta et al. [112] developed a method using ECG-gated computed tomography (CT) to generate patient-specific geometric meshes of the ascending aorta and to estimate the displacement and strain fields using a mathematical algorithm. As soon as full-field in vivo strain measurement is available, inverse methods can be developed to process DIC measurements and to reconstruct the regional variations of material properties.

Numerous mesh morphing tools developed for different applications may also enable tracking displacement fields. They usually consist in mapping a template mesh onto a patient-specific deformed geometry. For instance, Biancolini et al. [22] developed a mesh-morphing method for the human femur based on radial basis functions (RBFs) which are a class of mathematical interpolation functions. The interactive process implemented in a dedicated software (RBF morph<sup>®</sup>) allows to morph a template finite element model (FEM) onto a patient geometry by locating a set of landmark points. Another morphing technique based on RBF was developed to map the geometry of a healthy template aorta onto patient-specific ATAA geometries [25]. In addition, Couteau et al. [36] proposed a patient-specific method, called the mesh-matching (M-M) algorithm, allowing automatic 3D mesh generation of complex structures. The M-M algorithm was used to generate finite element models of the human femur from a template femur geometry.

The extension of mesh-morphing methodologies to estimate the displacement fields of the aorta is not straightforward. Input data are CT scans acquired throughout a cardiac cycle of a patient. Geometries at different phases throughout the cardiac cycle for a patient can be reconstructed using semi-automatic segmentation. Then one configuration of the aorta should be mapped onto another to ensure that their material points remain identical. Under the assumption that nodes are attached to the same material points in different phases, the displacement fields could be obtained using different methods. As a first method, the Vascular Modeling Toolkit (VMTK) [11] can be employed to derive the parametric coordinates of the arterial surface. Afterwards, structural mesh of each phase can be generated with an identical number of elements and nodes (to track the same material point) by applying a mesh morphing function between the geometries [52]. As a second method, the RBF morph<sup>®</sup> employed to calculate the coefficients of a linear system with an order equal to the number of source points [24], in which the displacement of an arbitrary node of the mesh is expressed as the summation of the radial contribution. Mesh smoothing can be achieved by preserving mesh topology in terms of total number, type and connectivity of the elements. [20, 21]. For both methods, anatomical references are required to ensure that the measurements taken at different phases of the cardiac cycle remain attached to the same identical locations in the aorta.



Therefore, the main objective of this chapter is to introduce methods to estimate the deformation fields of the aorta during a cardiac cycle. Afterwards, these results can be related to the measured pressure to achieve the global objective of the thesis which is reconstruction of stiffness properties.

## 2.3 Theory

Given reference and target geometries mesh morphing defines a transformation from the reference geometry to the target geometry. Some principles for proper mesh morphing are topology preservation, feature preservation, rigidity preservation, smoothness and the most importantly here, preserving identical material points of the two reference and target geometries. Topology preservation refers to preserving the topology such as no holes should suddenly appear during the morphing transition. Feature preservation refers to the preservation of important features, for example morphing between two animals, legs, heads and other features should remain during the transition. Rigidity preservation is the fact that sometimes a rigid transformation (rotation and translation) is preferred to a transformation. Smoothness means that the shape transformation should be smooth, avoiding discontinuities.

Fig. 2.1 shows a schematic morphing of a reference mesh onto a target geometry. The objects are represented by vertices and faces, so model  $M$  is a pair as  $(V, F)$ , where  $V$  is the set of vertices, with each vertex coordinates of  $v_i \in \mathbb{R}^3$ , while  $F$  is the set of faces, where each face,  $f_i$ , can be described by a triple  $(k, l, m)$  or quadruple  $(k, l, m, n)$ , with  $k, l, m$  and  $n$  indices of vertices forming the face  $f_i$ . In mesh morphing problems, there are two input meshes. The reference and target meshes are denoted as  $M^r = (V^r, F^r)$  and  $M^t = (V^t, F^t)$ , respectively (see Fig. 2.1). Therefore, morphing is a process of transforming  $M^r$  as a reference mesh into  $M^t$  as a target mesh by changing the coordinates of nodes (to fit them onto the target geometry) without changing the number of nodes or elements, while the connections between these nodes or elements remain unchanged.

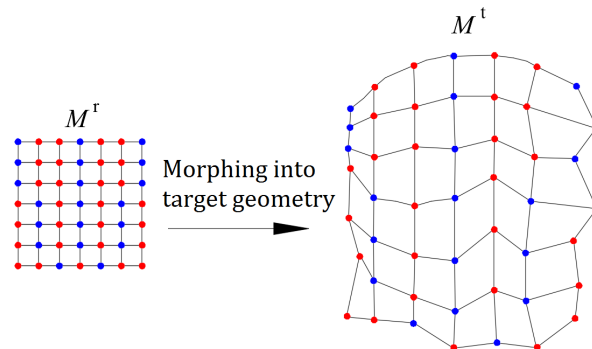


Figure 2.1: Schematic illustration of morphing a reference mesh into a target geometry.

Each reconstructed aortic model,  $M = (V, F)$ , from CT scans is composed of a set of nodes and it can be assumed that a node illustrates the position of the same material point at each

phase of the cardiac cycle. Because we have meshes at different phases of the cardiac cycle that do not satisfy this assumption, the objective of this chapter is to introduce methodologies based on mesh morphing that can create meshes satisfying this assumption.

### 2.3.1 Method I

Considering model  $M^j = (V^j, F^j)$  with  $j \in \{r, t\}$ , in this method we first derive the parametric coordinates,  $\mathbf{U}^j = (u^j, v^j) \in \mathbb{R}^2$ , of the Cartesian coordinates,  $\mathbf{X}^j = (x^j, y^j, z^j) \in \mathbb{R}^3$ , where  $u^j \in [0, L^j]$  and  $v \in [-\pi, \pi]$  are the longitudinal and circumferential components of the parametric coordinates, respectively. Upon  $\mathbf{U}^j$  is available a template mesh with  $u_{\text{temp}}^j \in [u_{\text{min}}^j, u_{\text{max}}^j]$  and  $v_{\text{temp}} \in [-\pi, \pi]$  should be morphed on the model  $M^j$  using an algorithm developed in MATLAB. To this end, an arbitrary number of points was created in a domain of  $(u_{\text{temp}}^j, v_{\text{temp}})$  as a template meshgrid. Afterwards, a polynomial approximation was implemented around each node of the template meshgrid.

### 2.3.2 Method II

In this method two models, the reference and target models, denoted by  $M^r = (V^r, F^r)$  with vertex number of  $n$  and  $M^t = (V^t, F^t)$  with vertex number of  $m$ , respectively, are available. The objective is to transform mesh of  $M^r$  into  $M^t$  by changing the coordinates of its nodes (to fit them onto the target geometry), preserving the topology of the mesh. RBF was applied to calculate the coefficients of a linear system with an order equal to the number of source points  $m$  using a multivariate polynomial corrector vector of order  $m - 1$ . In this method the displacement of an arbitrary node of the mesh is defined as the summation of the radial contribution.

## 2.4 Materials and methods

### 2.4.1 Data acquisition

After informed consent and according to a protocol approved by the Institutional Review Board of the University Hospital Center of Saint-Etienne (CHU-SE, France), non invasive systolic and diastolic blood pressures in brachial artery and gated CT scans were obtained for a patient who underwent elective surgical repair of ATAA at CHU-SE. Gated CT scans were obtained for the patients prior to ATAA surgical repair. Both diastolic and systolic phases (including phases in between diastolic and systolic phases) were acquired throughout the cardiac cycle and they were employed to reconstruct and track the geometrical variations of the whole aorta. Semi-automatic segmentation of the CT scans was achieved using MIMICS (v.10.01, Materialise NV). The obtained three-dimensional (3D) surface of the aorta was exported for diastolic and systolic phases with STL format. To identify the systolic and diastolic phases, the luminal volumes of each phase were computed. The systolic phase was defined as the largest volume and the diastolic phase as the smallest volume.

### 2.4.2 Computational implementation

At least two sets of images corresponding to two different phases of a cardiac cycle and subsequently two geometries should be available from gated CT scans to obtain the corresponding strain fields. The main purpose here is to derive a mathematical function, namely deformation, that maps one configuration of the aorta onto the other one ensuring that their material points remain identical. Therefore, each reconstructed aortic geometry should be meshed in such a way that each node represents the position of the same material point at each phase of the cardiac cycle. To do so, it is required that all phases are meshed with an identical number of nodes and elements.

#### 2.4.2.1 Method I

VMTK is used to calculate nodal parametric coordinates of each model. It is a collection of Python libraries and tools for 3D reconstruction, geometric analysis, mesh generation and surface data analysis for image-based modeling of blood vessels. The approach consists of several steps: calculation of centerlines, definition of the reference system, decomposition of the bifurcation into its branches and their parameterization.

Centerlines are calculated as the paths defined on Voronoi diagram sheets that minimize the integral of the radius of maximal inscribed spheres along the path in the arterial wall domain, corresponding to the shortest paths in the radius metric [10]. Assuming  $\Omega \subset \mathbb{R}^3$  is the vascular domain,  $\text{MA}(\Omega)$  is the medial axis,  $\gamma$  is a path between two endpoints of  $\mathbf{P}_1$  and  $\mathbf{P}_2$  parametrized by arclength  $\tau \in [0, L]$  over the  $\text{MA}(\Omega)$  and  $R(x)$  is the radius of maximal inscribed spheres, a centerline is traced by

$$\mathbf{c}(\tau) = \arg \min_{\gamma \in \text{MA}(\Omega)} \left\{ \int_{\gamma^{-1}(\mathbf{P}_1)=0}^{\gamma^{-1}(\mathbf{P}_2)=L} R[\gamma(\tau)^{-1} d\tau] \right\} \quad (2.1)$$

Since a centerline is made of all the centers of a subset of maximal inscribed spheres, it is possible to construct the canal surface or tube around each centerline which is the envelope of the spheres along the centerline. Therefore, assuming  $r(\tau)$  represents the radius of the spheres located along the centerlines, a tube surface around each centerline is defined as

$$T_{\mathbf{c},r}(\mathbf{x}) = \min_{\tau \in [0,L]} |\mathbf{x} - \mathbf{c}(\tau)|^2 - r^2(\tau) \quad (2.2)$$

The entity for the center of a sphere,  $\mathbf{P} \in \mathbb{R}^3$ , with radius  $r \in \mathbb{R}$  can be defined by  $\tilde{\mathbf{P}}(\mathbf{P}, ir) \in \mathbb{R}_1^4$ , where  $i$  denotes the imaginary unit. Therefore, a sphere in  $\mathbb{R}^3$  is a point in the four-dimensional Minkowski space of  $\mathbb{R}_1^4$ . This formalism allows easy generalization of the line geometry to that of tubes so that the definition of the tube in a more compact notation can be written

$$T_{\tilde{\mathbf{c}}}(x) = \min_{\tau \in [0,L]} |\mathbf{x} - \tilde{\mathbf{c}}(\tau)|^2 \quad (2.3)$$

with centerlines indicated as  $\tilde{\mathbf{c}}(\tau) = (\mathbf{c}(\tau), ir(\tau))$

After computing centerlines of a branching vascular segment, a set of lines are available, running from one inlet to each outlet. The interaction of two centerlines in a vascular tree intersect is defined as a bifurcation. Bifurcations are split into branches, by defining two points on each centerline which are termed as the reference points. The first reference point is where the centerline intersects the tube surface of another centerline and the second reference point is the center of the nearest upstream sphere touching the first reference point, respectively defined as

$$\tau_1^A = \min\{\tau_1 \in [0, L_1]\} : \exists \tau_2 \in [0, L_2] : |c_1(\tau_1) - \tilde{c}_2(\tau_2)|^2 = 0 \quad (2.4)$$

$$\tau_1^B = \max\{\tau_1 \in [0, \tau_1^A]\} : |\tilde{c}_1(\tau_1) - c_1^A|^2 = 0 \quad (2.5)$$

Eq. 2.4 indicates that  $\tilde{c}_1(\tau_1)$  and  $\tilde{c}_2(\tau_2)$  are two centerlines traced between the same inlet and two bifurcation outlets at which the point  $c_1(\tau_1)$  crosses the tube surface  $\tilde{c}_2(\tau_2)$ , with reference point  $\tilde{c}_1^A = \tilde{c}_1(\tau_1^A)$ .

The decomposition of branches is implemented based on the identified reference points. Centerlines are split into tracts equivalent to each bifurcation branches. The actual surface decomposition is performed by partitioning space around the tube surfaces of the centerline tracts corresponding to each branch. Fig. 2.2-a and Fig. 2.2-b show the centerlines and split surface (decomposition) of a real patient's geometry.

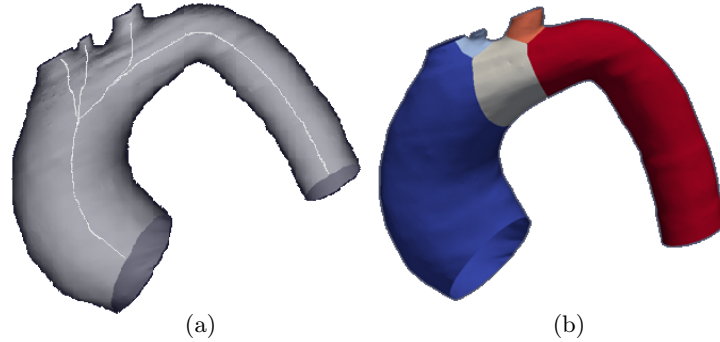


Figure 2.2: a- Centerlines and b- split surface (decomposition) of a real patient's geometry.

Each branch is topologically equivalent to a cylinder after split of a bifurcation into branches and is mapped onto a set of rectangular parametric coordinates. Let us assume that  $\partial\Omega_i$  represents the surface of the  $i$ th branch determined by two topological circles  $\psi_{i0}$  and  $\psi_{iL}$ . Considering that  $U = (u, v) \subset \mathbb{R}^2$  is the parametric space with the longitudinal and periodic circumferential parametric coordinates of  $u \in [0, L_i]$  and  $v \in [-\pi, \pi]$ , respectively, a bijective mapping can be presented by [11]

$$\Phi : \partial\Omega_i \rightarrow U_{\mathbf{u}} \quad (2.6)$$

satisfying  $\Phi(\mathbf{x}) = (0, v)$  on  $\psi_{i0}$  and  $\Phi(\mathbf{x}) = (L_i, v)$  on  $\psi_{iL}$ . VMTK generates longitudinal mapping using a stretch and a harmonic function to localize centerline abscissa and reference system [68]. Solving the elliptic partial differential equation, the harmonic function  $f = f(\mathbf{x})$

with  $\mathbf{x} \in \partial\Omega_i$  is calculated by

$$\Delta_B f = 0 \quad (2.7)$$

and subsequently, the stretch function,  $s$ , can be expressed by

$$s(f) = \frac{1}{|\lambda(f)|} \int_{\lambda(f)} g(\mathbf{x}) d\lambda \quad (2.8)$$

where  $\lambda(f)$  denotes a level-set of  $f$  and  $\Delta_B$  is the Laplace-Beltrami operator. Therefore, the longitudinal parametric coordinate is calculated by

$$u(\mathbf{x}) = s \circ f(\mathbf{x}) \quad (2.9)$$

and the circumferential parametric coordinate is computed by

$$v(\mathbf{x}) = \arccos((\mathbf{x} - \mathbf{c}(\tau)) \cdot \mathbf{n}(\tau)) \quad (2.10)$$

where  $\mathbf{n}(\tau)$  is the angular position of each node directed towards the center of the osculating circle of the curve. It is defined by a set of normals along the arclength of  $\tau$ .

#### 2.4.2.2 Postprocessing the parametric results of VMTK in MATLAB

VMTK provides longitudinal and circumferential parametric coordinates for each distinguished group of branches shown in Fig 2.2. It is required to postprocess these results to obtain the structural mesh and connectivity. For this purpose, an arbitrary number of points was created in the  $u_{\text{temp}} \in [u_{\min}, u_{\max}]$  and  $v_{\text{temp}} \in [-\pi, \pi]$  domain as a template meshgrid. Afterwards, a polynomial approximation was implemented around each node of the template meshgrid. Assume  $(u_{\text{temp}}^i, v_{\text{temp}}^i)$  presents the parametric coordinates of node  $\mathbf{X}_i$  from template meshgrid and  $(\mathbf{u}_{\text{nb}}, \mathbf{v}_{\text{nb}})$  denotes the parametric coordinates of several neighborhood nodes around  $\mathbf{X}_i$  on the aortic surface (parametric coordinates of all nodes on the aortic surface are available from VMTK results). The neighborhood nodes were selected based on condition as

$$du_j = (u_{\text{nb}}^j - u_{\text{temp}}^i) < \delta_u \quad (2.11a)$$

$$dv_j = (v_{\text{nb}}^j - v_{\text{temp}}^i) < \delta_v \quad (2.11b)$$

where  $\delta_u$  and  $\delta_v$  are preselected values denoting the size of the neighborhood. They are chosen based on mesh quality (fine or coarse) of the aortic surface. A polynomial approximation was then employed to minimize the squares of

$$R = \mathbf{A}\mathbf{X} - \mathbf{X}_{\text{nb}} \quad (2.12)$$

with

$$\mathbf{A} = \begin{bmatrix} 1 & du_1 & dv_1 & du_1 dv_1 & du_1^2 & dv_1^2 & du_1^2 dv_1 & du_1 dv_1^2 \\ \vdots & \vdots & \vdots & \vdots & \vdots & \vdots & \vdots & \vdots \\ 1 & du_k & dv_k & du_k dv_k & du_k^2 & dv_k^2 & du_k^2 dv_k & du_k dv_k^2 \\ \vdots & \vdots & \vdots & \vdots & \vdots & \vdots & \vdots & \vdots \\ 1 & du_n & dv_n & du_n dv_n & du_n^2 & dv_n^2 & du_n^2 dv_n & du_n dv_n^2 \end{bmatrix} \quad (2.13)$$

$$\mathbf{X} = \begin{bmatrix} X_1 & Y_1 & Z_1 \\ X_2 & Y_2 & Z_2 \\ \vdots & \vdots & \vdots \\ X_8 & Y_8 & Z_8 \end{bmatrix} \quad (2.14)$$

and

$$\mathbf{X}_{nb} = \begin{bmatrix} X_{nb}^1 & Y_{nb}^1 & Z_{nb}^1 \\ \vdots & \vdots & \vdots \\ X_{nb}^k & Y_{nb}^k & Z_{nb}^k \\ \vdots & \vdots & \vdots \\ X_{nb}^n & Y_{nb}^n & Z_{nb}^n \end{bmatrix} \quad (2.15)$$

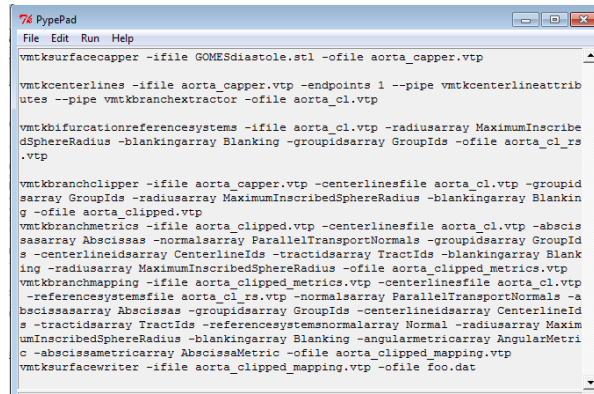
Consequently, solving this system of equations in MATLAB, the structural mesh of the aorta including nodes and connectivities can be generated. Before starting VMTK some manual work should be performed on the available STL files. The segmented geometries of STL files had some local irregularities (bumps) due to image noise at each phase of the cardiac cycle. These bumps were filtered such that VMTK could run. The inlets and outlets of the imported mesh into VMTK should be open in order to define source points to calculate centerline. When the geometry is ready for running VMTK, we write the appropriate scripts such as centerline calculation, definition of reference points, decomposition and mapping of bifurcating vessels (Fig. 2.3). To run the scripts, we use VMTK from a Tcl/Tk GUI. It is needed to ensure that the measurements taken at different phases of the cardiac cycle are attached to the same identical material points of the aorta. Therefore, coronary and brachiocephalic arterial branches are employed to provide anatomical reference positions along the aortic centerline based on the longitudinal component of the parametric coordinates, as shown in Fig. 2.4. To adjust the phases longitudinally, the origin of  $u$  was set in the coronary plane at each phase. Using results of VMTK, MATLAB was used to solve the system of equations written in Eqs. 2.12-2.15 assuming  $\delta_u=8$  mm and  $\delta_v=\pi/5$  rad (they can slightly vary for each patient depending on mesh quality). Then a structural mesh of each phase is obtained with an identical number of nodes and elements. Subtraction of the nodal coordinates between systole and diastole delivers the displacements of the aorta between the two phases. Strains are derived from displacements by performing a Dirichlet finite element analysis (FEA) in ABAQUS.

### 2.4.2.3 Method II

In this method, we use RBF Morph<sup>®</sup> to directly transform the reference mesh onto the target model with the identical numbers of nodes and elements. RBFs are a class of mathematical interpolation functions that can be used to derive mesh morphing of the computational model in a discretized domain, generally used in Computer-Aided Engineering (CAE) applications. It applies predefined displacements to a set of purposely generated points, namely source points. To solve the RBF mathematical problem, the scalar parameters (sought coefficients) of a linear

system with the same order as the number of interested source points are calculated. Once the RBF system coefficients have been calculated, the displacement of an arbitrary node from the mesh can be expressed as the summation of the radial contribution of each one. Consequently, a desired modification of the mesh nodal position (smoothing) can be properly applied by preserving mesh topology in terms of total number, type and connectivity of the constituting elements. The combined variation of the coordinates of surface and volume nodes (morphing) is typically, but not always, performed on the starting configuration of the computational model to generate new geometries without remeshing obligations [24].

In particular, the RBF Morph<sup>®</sup> tool employs the RBF interpolant,  $s(\mathbf{x})$ , which includes a radial function containing the RBF,  $\Phi$ , of order  $m$  and a multivariate polynomial corrector vector,  $h(\mathbf{x})$ , of order  $m - 1$ , ensuring the compatibility of rigid motions. Specifically, if  $N$  is



```

vmtksurfacecapper -ifile GOMESdiastole.stl -ofile aorta_capper.vtp

vmtkcenterlines -ifile aorta_capper.vtp -endpoints 1 --pipe vmtkcenterlineattrib
utes --pipe vmtkbranchextractor -ofile aorta_cl.vtp

vmtkbfurcationreferencesystems -ifile aorta_cl.vtp -radiusarray MaximumInscribe
dSphereRadius -blankingarray Blanking -groupidarray GroupIds -ofile aorta_cl_rs
.vtp

vmtkbranchclipper -ifile aorta_capper.vtp -centerlinesfile aorta_cl.vtp -groupid
array GroupIds -radiusarray MaximumInscribedSphereRadius -blankingarray Blankin
g -ofile aorta_clipped.vtp

vmtkbranchmetrics -ifile aorta_clipped.vtp -centerlinesfile aorta_cl.vtp -abscis
sasarray Abscissas -normalsarray ParallelTransportNormals -groupidarray GroupId
s -centerlineidsarray CenterlineIds -tractidsarray TractIds -blankingarray Blank
ing -radiusarray MaximumInscribedSphereRadius -ofile aorta_clipped_metrics.vtp

vmtkbranchmapping -ifile aorta_clipped_metrics.vtp -centerlinesfile aorta_cl.vtp
-referencesystemsfile aorta_cl_rs.vtp -normalsarray ParallelTransportNormals -a
bscissasarray Abscissas -groupidarray GroupIds -centerlineidsarray CenterlineId
s -tractidsarray TractIds -referencesystemsnormalarray Normal -radiusarray Maxim
umInscribedSphereRadius -blankingarray Blanking -angularmetricarray AngularMetri
c -abscissametricarray AbscissaMetric -ofile aorta_clipped_mapping.vtp

vmtksurfacewriter -ifile aorta_clipped_mapping.vtp -ofile foo.dat

```

Figure 2.3: VMTK scripts to derive the parametric coordinates of each node.

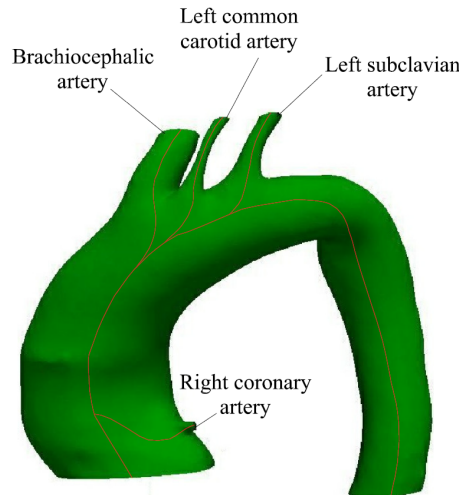


Figure 2.4: Segmentation of the aortic geometry for diastolic phase, including left subclavian artery, brachiocephalic artery, left common carotid artery and coronary artery branches. Coronary and brachiocephalic arterial branches are employed to provide anatomical reference positions along the aortic centerline based on the longitudinal component of the parametric coordinates.

the total number of source points, the RBF interpolant can be written as

$$s(x) = \sum_{i=1}^N \gamma_i \Phi(\|x - x_i^s\|) + h(x) \quad (2.16)$$

where  $x$  is the vector identifying the position of a generic node belonging to the surface and/or volume mesh,  $x_i^s$  is the  $i$ th source node position vector and  $\|\bullet\|$  is the Euclidean norm.

A great flexibility using RBF can be achieved by using different radial functions that can be locally or globally applied. Several options for RBF are summarized in Table 2.1. RBF morph<sup>®</sup>

Table 2.1: Typical Radial Basis Functions.

Radial functions	$\Phi(r)$
Spline type	$r^n, \forall n = 2k + 1; k = 1, 2, \dots$
Thin plate spline	$r^n \log(r), \forall n = 2k; k = 1, 2, \dots$
Multiquadric	$\sqrt{1 + r^2}$
Inverse Multiquadric	$\frac{1}{\sqrt{1 + r^2}}$
Inverse quadratic	$\frac{1}{1 + r^2}$
Gaussian	$e^{-r^2}$

is implemented in Fluent (ANSYS<sup>®</sup> Academic Research, Release 17.0) to compute the coordinates of the morphed geometry using reference (for example diastole) and target geometries (for example systole). For RBF morph<sup>®</sup>, it is required to import the reference geometry as 3D solid elements in Fluent (ANSYS<sup>®</sup> Academic Research, Release 17.0). Therefore, the outer wall was interpolated assuming a wall thickness of 2 mm. To derive the displacement and eventually strain, the three steps using method II were:

1. In RBF morph<sup>®</sup>, to obtain the displacements, the landmarks can be selected by inserting their coordinates on the surface mesh of the coronary and brachiocephalic arteries in RBF morph<sup>®</sup> [22]. Therefore, a set of points, two points in the boundary of coronary artery and two points in the boundary of brachiocephalic artery as seen in Fig. 2.5, are selected. The coordinates of landmarks on the reference geometry are inserted in RBF morph<sup>®</sup>. Corresponding points are defined by introducing the corresponding displacements on the surface mesh of the deformed (target) aorta via points panel as shown in Fig. 2.5 and 2.7. We need these landmarks between coronary and brachiocephalic arteries to control the axial movement of the aorta resulting from heart motions.
2. The resulting 3D solid mesh is projected onto the target one using the "STL target" tool of RBF morph<sup>®</sup> (Fig. 2.6). The target is transformed into an implicit RBF surface using surfs panel that allows an accurate projection. A field moving the original mesh onto the target is now available after solving and morphing via solve and morph panels (Fig. 2.7).



3. Having in hand the reference and morphed geometries, we derive the displacement using RBF morph<sup>®</sup> between them by subtraction of the nodal coordinates of both geometries. Finally, to obtain the strain map, a Dirichlet FEA was performed in ABAQUS.

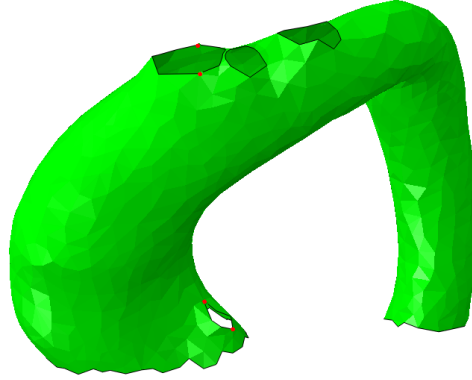


Figure 2.5: Landmarks on the boundary of coronary and brachiocephalic arteries (two points in the boundary of the coronary artery and two points in the boundary of brachiocephalic artery). Red points show the landmarks.

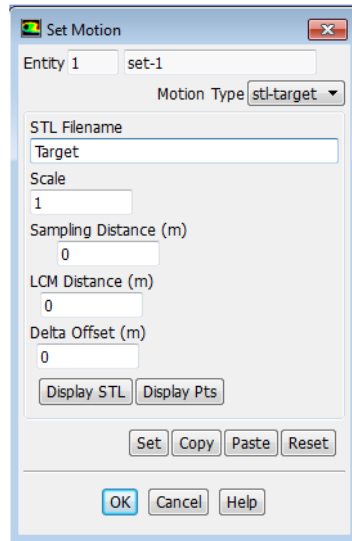


Figure 2.6: Panel of STL target in RBF morph<sup>®</sup> to apply the projection.

### 2.4.3 Numerical verification

As mentioned above, morphing methods were employed to calculate in vivo displacements between two phases of the cardiac cycle and subsequently to compute circumferential and axial strains. Therefore, here the aim is first to ensure that the displacements obtained by method I and method II are consistent. We need a reference case where the strain field is precisely known between two different geometries, to evaluate the two methodologies. To this end, we chose a raw STL file (in diastole) segmented from CT images as a reference geometry (RG) to obtain a deformed geometry (DG) by FEA under predefined loading conditions. The STL file

of RG was imported into Abaqus as shell triangular elements with two Gauss points. Linear elastic mechanical behavior was used. Thus, in the absence of body forces and independent from the coordinate system, equilibrium of linear momentum on the arterial wall reads

$$\nabla \cdot \boldsymbol{\sigma} = 0 \quad (2.17)$$

This is also referred as Newton's second law.  $\nabla$  represents the nabla operator and  $\boldsymbol{\sigma}$  is the Cauchy stress tensor. For elastic materials, Hooke's law represents the material behavior and relates the stresses and strains. The general equation for Hooke's law (constitutive equations) is given by

$$\boldsymbol{\sigma} = \mathbb{C} : \boldsymbol{\varepsilon} \quad \text{with} \quad \boldsymbol{\varepsilon} = \frac{1}{2}[\nabla \mathbf{u} + \nabla \mathbf{u}^T] \quad (2.18)$$

where  $\mathbb{C}$  denotes the fourth-order stiffness tensor while  $\boldsymbol{\varepsilon}$  and  $\mathbf{u}$  are the infinitesimal strain tensor and the displacement vector, respectively.  $(\bullet)^T$  displays a transpose and  $\mathbf{A} : \mathbf{B} = A_{ij}B_{ij}$  is the inner product of two second-order tensors.

The RG was loaded by an average intramural pressure ( $P=40$  mmHg (5.33 kPa)). Besides, we considered the same boundary conditions on the inlet and all outlets of the ATAA model, allowing only radial displacements and blocking displacements in the other two directions (circumferential and axial).

The displacement and strain maps for the DG were obtained from FEA. Having in hand RG and DG as diastolic and systolic geometries, respectively, we were able to verify the accuracy of each method. Here displacement and strain maps were validated from FEA performed with a heterogeneous stiffness distribution. Three regions with different stiffness were defined in the aorta as shown in Fig. 2.8.

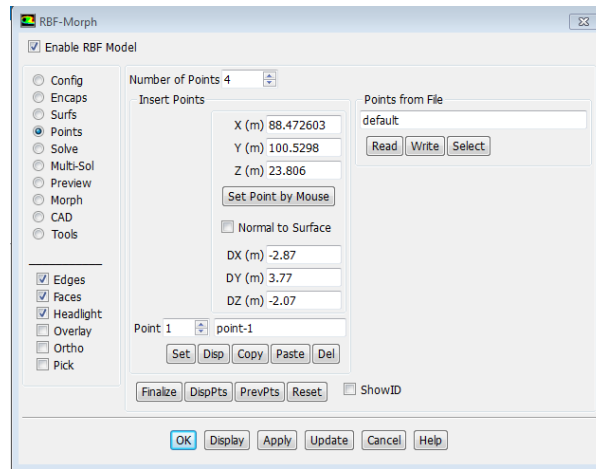


Figure 2.7: RBF morph points panel to introduce the landmarks. The coordinates of landmarks on the reference geometry and the corresponding displacements on the target geometry are shown.

## 2.5 Results

The displacement and first principal strain maps of the original FEA are shown in Figs. 2.9 and 2.10, respectively. To verify the accuracy of each methodology, we compared the displacement and strain maps obtained from I and II with the original reference FEA.

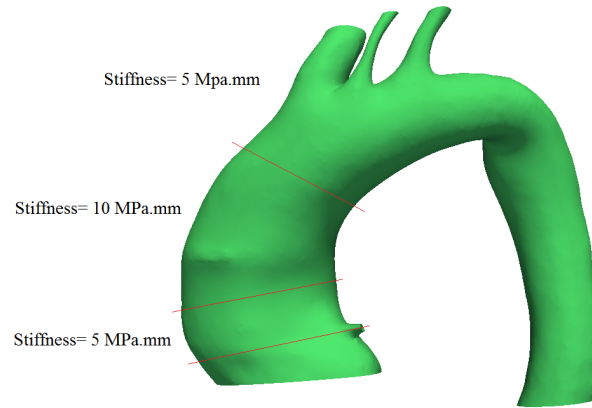


Figure 2.8: Heterogeneous stiffness distribution considered in the aorta to obtain DG from FEA of RG.

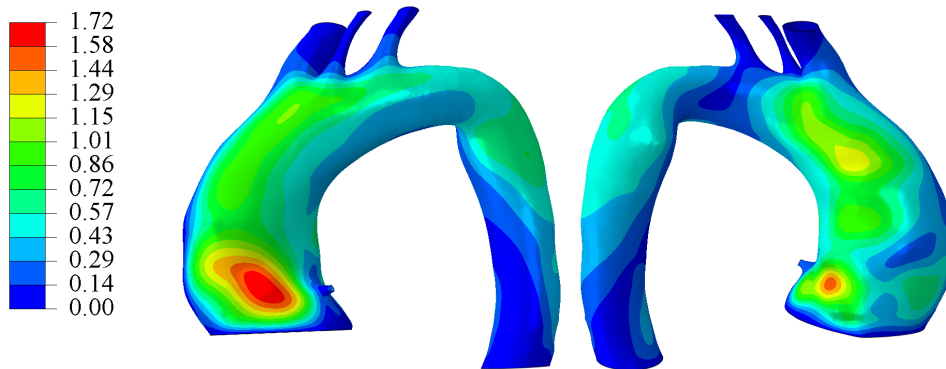


Figure 2.9: Map of the displacement magnitude obtained by the FEA model of a RG from two different views.

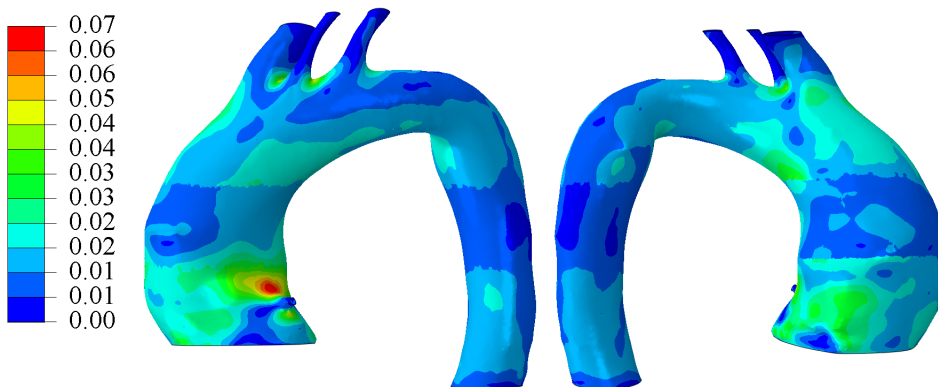


Figure 2.10: Map of the first principal strain obtained by the FEA model of a RG from two different views.

### 2.5.1 Method I

A region of interest in the ascending aorta in Fig. 2.9 and 2.10 is cut and shown in Figs. 2.11-a and 2.12-a. Comparing displacements and first principal strain distributions reconstructed by method I (Figs. 2.11-b and 2.12-b) with the corresponding maps obtained from FE, one can observe a good agreement between them. This indicates that structural meshes of both RG and DG geometries generated by method I are related to the same points.

In addition, to evaluate the consistency of method I with the FEA results from a quantitative point of view, we calculated the root mean square error (RMSE) value between corresponding displacements presented in Figs. 2.11-a and 2.11-b as well as corresponding first principal strains presented in Figs. 2.12-a and 2.12-b. The quantitative results reported in Table 2.2 indicate that the result from method I and FEA are very close, validating the strain reconstruction using method I.

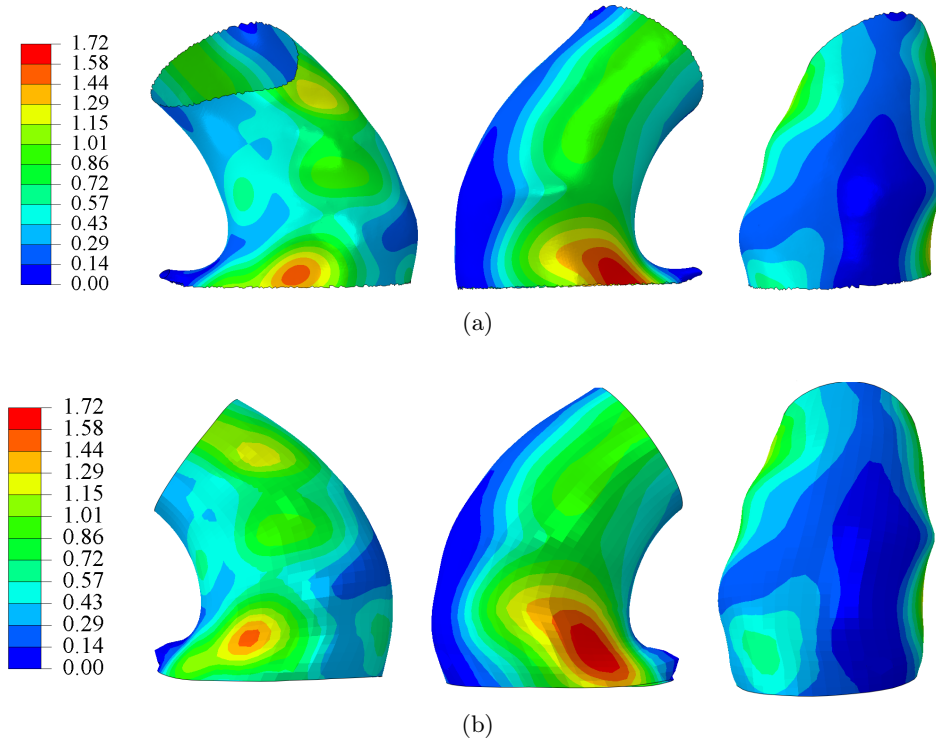


Figure 2.11: Map of displacement magnitude obtained by a- FEA, a cut from region of interest in ascending aorta in Fig. 2.9, b- method I

### 2.5.2 Method II

Displacement magnitude and first principal strain distributions reconstructed using method II are shown in Fig. 2.13 and 2.14, respectively. Comparison of magnitude of displacements reconstructed by method II with the corresponding results of original reference FEA in Fig. 2.11-a illustrated that the displacements obtained from method II were not in good agreement with those of the original FEA. It was not unexpected that this inaccurate displacement reconstruc-

tion causes a considerable error in reconstruction of strain distribution (see Figs. 2.12-a and 2.14). This indicated that RG and DG geometries morphed by method II were poorly related to corresponding material points.

Moreover, we analyzed the results obtained from original FEA and method II from a quantitative point of view. For this purpose, the RMSE value between corresponding displacements presented in Figs. 2.11-a and 2.13 as well as corresponding first principal strains presented in Figs. 2.12-a and 2.14. The results have been summarized in Table 2.2 for each method.

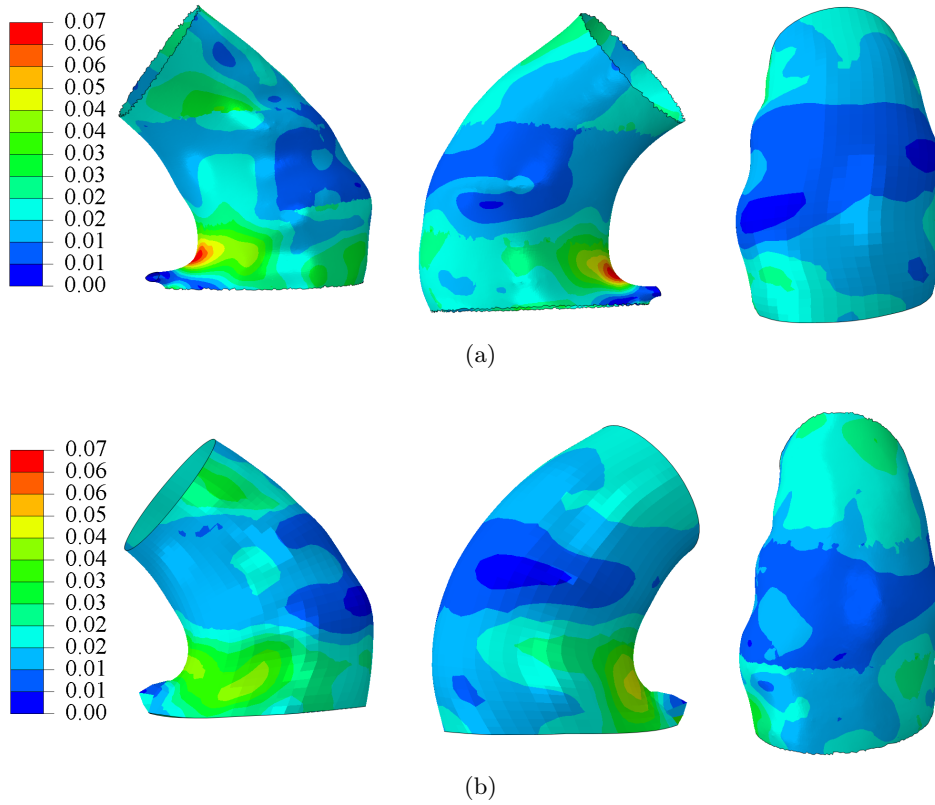


Figure 2.12: Map of first principal strain obtained by a- FEA, a cut from region of interest in ascending aorta in Fig. 2.10, b- method I

Table 2.2: Root mean square error values for each method in directions of  $X$ ,  $Y$ ,  $Z$  and magnitude.  $U_x$ ,  $U_y$  and  $U_z$  are displacement components while  $U$  and  $\epsilon_{\max}$  are the displacement magnitude and first principal strain respectively.

Method	$U_x$	$U_y$	$U_z$	$U$	$\epsilon_{\max}$
1	$6.52e^{-7}$	$4.3e^{-7}$	$2.58e^{-7}$	$1.45e^{-11}$	$6.4e^{-3}$
2	0.48	0.47	0.3	0.2	0.1

## 2.6 Discussion and conclusion

In this study two sets of images corresponding to two different phases of a cardiac cycle obtained from gated CT scans were used. After geometry reconstruction some manual cleaning of each geometry, was needed. The results of the VMTK as metric data were used to solve a system of equations in MATLAB to obtain structural meshes for RG and DG. In contrast, by executing Fluent (ANSYS® Academic Research, Release 17.0), it is automatic to reconstruct the deformation between RG and DG with the same material points using method II. However, before starting the RBF morph® process it is also required to remove some negative volumes from RG and to convert RG to 3D solid elements by applying a finite thickness. When RG and DG are available with the same nodes attached to the material points, it is simple to calculate and to visualize displacements in between two geometries by subtraction of DG from RG. The remaining steps for reconstruction of the strain are very similar in both methods. Therefore, using method II, the process to derive the displacements can be considered as an automatic method. Reconstruction of displacements by method I was very time consuming and requiring many manual steps beside of the non-automatic segmentation step. We noticed that regarding processing time, method II could be a good alternative for this purpose, being very user-friendly due to implementation in Fluent (ANSYS® Academic Research, Release 17.0).

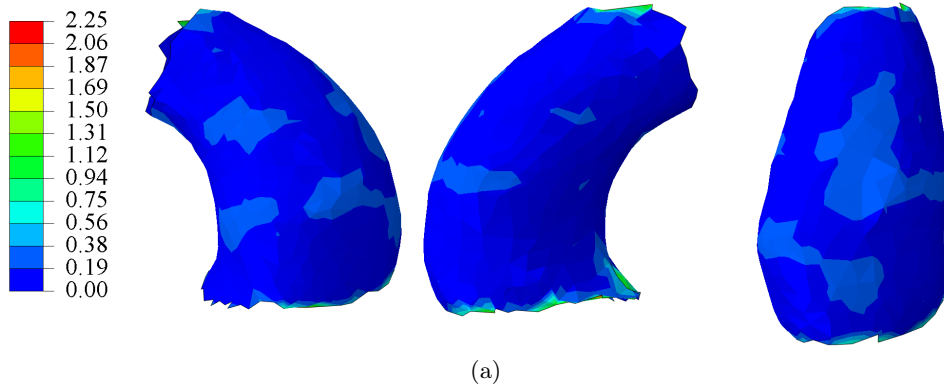


Figure 2.13: Displacement maps obtained by method II [mm].

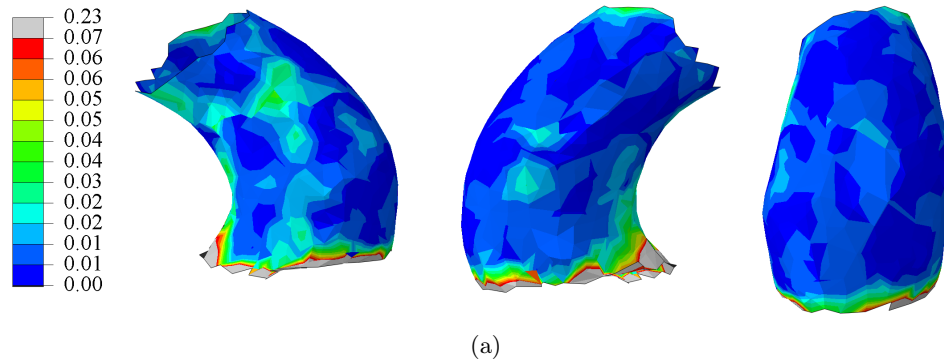


Figure 2.14: Strain maps obtained by method II.

By comparing the three different results qualitatively, we concluded that the displacement reconstruction by method II was far from what we expected while method I delivered consistent displacements. We also performed a quantitative analysis of data between both methods with the ones obtained by original FEA. The results showed that the RMSE value for the results of method I (displacement and reconstructed strain) showed high accuracy of method I in comparison with method II.

To conclude, method I appears to be more reliable for tracking the displacement of nodes attached to the same material points in the aortic wall. However, method II is very powerful to morph the geometry to the nearest distance and an appropriate application to automatically morph an existing mesh to conform to a geometry maintaining constant mesh topology. It has also ability to modify mesh topology preserving element quality. At this stage, we decided to employ method I for displacement and strain reconstruction rather than method II as the results using method I were more accurate and reliable, despite being more time consuming.





# Inverse identification of local stiffness across ATAA

**Authors:** Solmaz Farzaneh, Olfa Trabelsi and Stéphane Avril

**Published in:** BMMB journal (Farzaneh, S., Trabelsi, O. & Avril, S. Biomech Model Mechanobiol (2018). <https://doi.org/10.1007/s10237-018-1073-0>)

## Résumé

Comme indiqué dans l'état de l'art (chapitre 2), différents facteurs mécaniques sont introduits pour améliorer de manière fiable la prise de décision chirurgicale chez les patients affectés par l'ATAA. Le diamètre présente une insuffisance pour être considéré comme un indicateur fiable du risque de rupture. Comme le critère de risque en déformation montre une bonne corrélation avec la rigidité, nous voulons nous concentrer sur l'identification in vivo spécifique au patient de la rigidité locale de l'ATAA de manière non invasive. En utilisant les tomodensitogrammes préopératoires, une segmentation semi-automatique des tranches de tomodensitométrie a été réalisée dans MIMICS (v.10.01, Materialise NV) pour 3 patients. Un maillage structural de l'aorte est défini avec un ensemble de nœuds attachés aux mêmes points matériels à différentes phases tout au long du cycle cardiaque. Les séries de Fourier ont été utilisées pour obtenir le déplacement (terme fondamental) permettant de reconstruire la distribution locale des contraintes. La déformation a ensuite été reliée à la pression (pressions brachiales mesurées lors de la tomodensitométrie) et l'équilibre a été écrit pour reconstruire la rigidité membranaire locale à chaque position.

## Résultats:

-Les distributions de la rigidité membranaire locale apparaissent hétérogènes, en particulier dans l'ATAA.

-La distribution de la rigidité membranaire locale,  $Q$ , a montré des valeurs plus élevées pour les aortes ascendantes par rapport aux aortes descendantes.

-Une analyse statistique a été réalisée pour comparer la rigidité identifiée à celle obtenue par deux méthodes précédemment développées ( $Q_{in-vitro}$  and  $Q_{in-vivo}$ ). Cette analyse a montré que les valeurs médianes et interquartiles pour différentes coupes chez tous les patients se situaient relativement aux mêmes gammes. Comparant la boîte interquartile obtenue dans cette étude avec les résultats correspondants de [138], il peut être déduit que pour tous les patients,  $Q_{in-vivo}$  est une valeur comprise entre la valeur inférieure et la valeur médiane (principalement proche de la médiane) alors que les valeurs de  $Q_{in-vitro}$  sont proches des valeurs interquartiles correspondantes inférieures.

---

## Contents

<b>3.1</b>	<b>Abstract . . . . .</b>	<b>46</b>
<b>3.2</b>	<b>Introduction . . . . .</b>	<b>46</b>
<b>3.3</b>	<b>Material and methods . . . . .</b>	<b>48</b>
3.3.1	Origin of data . . . . .	48
3.3.2	Theory of the inverse approach . . . . .	48
3.3.3	Numerical implementation . . . . .	54
<b>3.4</b>	<b>Results . . . . .</b>	<b>55</b>
3.4.1	Numerical verification . . . . .	55
3.4.2	Linear elastic material property . . . . .	55
3.4.3	Non-linear anisotropic material property . . . . .	56
3.4.4	Patient-specific results . . . . .	59
3.4.5	Comparison of the results . . . . .	60
<b>3.5</b>	<b>Discussion . . . . .</b>	<b>61</b>
3.5.1	General remarks . . . . .	61
3.5.2	Limitations . . . . .	65
<b>3.6</b>	<b>Conclusion . . . . .</b>	<b>66</b>

---

### 3.1 Abstract

Aortic dissection is the most common catastrophe of the thoracic aorta, with a very high rate of mortality. Type A dissection is often associated with an ascending thoracic aortic aneurysm (ATAA). However, it is widely acknowledged that the risk of type A dissection cannot be reliably predicted simply by measuring the ATAA diameter and there is a pressing need for more reliable risk predictors. It was previously shown that there is a significant correlation between a rupture criterion based on the ultimate stretch of the ATAA and the local extensional stiffness of the aorta. Therefore, reconstructing regional variations of the extensional stiffness across the aorta appears highly important. In this paper, we present a novel non-invasive inverse method to identify the patient-specific local extensional stiffness of aortic walls based on preoperative gated CT scans. Using these scans, a structural mesh is defined across the aorta with a set of nodes attached to the same material points at different time steps throughout the cardiac cycle. For each node, time variations of the position are analyzed using Fourier series, permitting the reconstruction of the local strain distribution (fundamental term). Relating these strains to tensions with the extensional stiffness, and writing the local equilibrium satisfied by the tensions, the local extensional stiffness is finally derived at every position. The methodology is applied onto the ascending and descending aorta of three patients. Interestingly, the regional distribution of identified stiffness properties appears heterogeneous across the ATAA. The identified stiffness is also compared on average with values obtained using other non-local methodologies. The results support the possible non-invasive prediction of stretch-based rupture criteria in clinical practice using local stiffness reconstruction. Keywords: Non-invasive inverse method; Local extensional stiffness; Finite-elements; Ascending thoracic aortic aneurysms; Patient-specific; Risk of rupture

### 3.2 Introduction

Ascending thoracic aortic aneurysms (ATAAs) manifest by localized ballooning of the aorta. They are difficult to detect because they usually have no symptom. Unrecognized and untreated TAA may lead to dissection or rupture of the aneurysm ending with instantaneous death. Independently of age and gender, about 30,000 people in Europe and 15,000 people in the United States are diagnosed with a TAA every year [23, 84, 120].

ATAA are commonly treated with a timely surgical repair by replacement of the dilated aortic segment with synthetic grafts. For patients without any familial disorders such as Marfan syndrome, elective surgical intervention of ATAA is recommended when its diameter is larger than 5.5 cm or when it is considered as a fast growing aneurysms (growth > 1 cm per year) [29, 32, 33, 47, 84]. The diameter of 5.5 cm as a criterion of surgical intervention is extensively recognized as an insufficient criterion. For example, the International Registry of Acute Aortic Dissection (IRAD) conveyed that among 591 type "A" aortic dissections, 59% had a diameter below 5.5 cm. Moreover, several studies considering abdominal aortic aneurysms (AAA) suggest that biomechanical factors may reliably predict the risk of rupture rather than the diameter

criterion alone [45, 54, 61]. Wall stress analysis and identification of patient-specific material properties of abdominal aortic aneurysms using 4D ultrasound were performed to improve rupture risk assessment [143]. It is well-known that the rupture of ATAA occurs when the stress applied to the aortic wall reaches the rupture stress [97, 99, 136]. Another definition of rupture can be represented when the stretch applied to the tissue is greater than its maximum extensibility or distensibility (stretch based rupture criterion). Accordingly, Duprey et al. [44] proposed a stretch-based rupture risk criterion and showed its correlation with tangent elastic modulus in ATAA based on data collected in 31 patients. In that study, individual rupture stretch and tangent elastic moduli were determined *in vitro* by means of bulge inflation tests on the identical ATAA wall tissue segments that had been excised intraoperatively. Trabelsi et al. [138] proposed a method for the *in vivo* identification of the (global) stiffness of an aortic segment based on the determination of volumetric distensibility from gated CT scans and pulsed pressure. However, only moderate correlation was found between the global *in vivo* stiffness values and the (local) stretch based rupture risk criterion determined from bulge inflation tests on excised tissue segments of 13 ATAA. Therefore, the assessment of the local elastic properties of the ATAA-wall from *in vivo* data that are clinically available, might be a crucial point for establishing a reliable method of estimation of ATAA rupture risk [105]. In the present paper, a new inverse approach to this task is presented.

This is meaningful as stiffening of the aortic wall is both a cause and a consequence of ATAA [30, 146]. Stiffening leads to a decrease of extensibility due to loss of elastin and deposition of collagen during growth and remodeling. There are studies that have indeed demonstrated such stiffening (without wall weakening) in age-matched subjects [60, 82]. They mostly found local variations of mechanical parameters along the longitudinal direction, indicating higher strength and peak elastic modulus along the circumferential direction compared to the longitudinal direction [82]. Therefore, identifying non-invasively the *in vivo* elastic properties of the aorta would help clinicians to take decisions whether the patient needs surgical intervention. Besides, the mechanical properties can be used to perform computational analyses, the accuracy of which will rely on the accuracy of input parameters.

However, non-invasive characterization of elastic properties is not the most common approach for deriving material properties of aortas. The most common methods to obtain material properties are *in vitro* uniaxial and biaxial mechanical tests [30, 62, 109]. They permit plotting stress-strain curves and deriving parameters of strain energy functions or linearized elastic moduli of the aneurysmal walls at different stages of loading [146]. Several studies have characterized the mechanical properties of ATAA via strain energy functions and elastic moduli indicating that ATAA causes stiffening and extensibility reduction. To assess rupture risk on a patient-specific level, their results imply decreased tissue compliance as a rupture risk factor [98, 131].

To our best knowledge no study has ever identified regional variations of material properties in ATAAs on a patient-specific basis using a non-invasive methodology. Therefore, the main objective of this work is to present a novel methodology based on gated CT images for the iden-

tification of local stiffness properties in ATAAs under assumptions of linearized and isotropic elasticity. After a comprehensive presentation, we present different numerical validations of the methodology and show exemplary results in three patients proof of concept.

### 3.3 Material and methods

#### 3.3.1 Origin of data

After informed consent and according to a protocol approved by the Institutional Review Board of the University Hospital Center of Saint-Etienne, non invasive systolic and diastolic blood pressures in brachial artery and gated CT scans were obtained for three patients who underwent elective surgical repair of ATAA at the University Hospital of Saint-Etienne (CHU-SE) in France. The demographic information of these patients is recorded in Table 3.1. For each patient, images were recorded at ten phases of their cardiac cycle. These images were used to reconstruct the geometry of their whole aorta, including diastolic and systolic phases. Semi-automatic segmentation of the CT image slices was done using MIMICS (v.10.01, Materialise NV). The three-dimensional (3D) surface of the aorta was generated for each phase and exported as STL format. All phases were cut by the same cross sectional planes to predefine a domain of the aorta larger than the final segment of interest in both ascending and descending parts. The purpose was to initiate the procedure in order to run the Vascular Modeling Toolkit (VMTK, Orobix, Bergamo, Italy; [www.vmtk.org](http://www.vmtk.org)) [11] and to derive the parametric coordinates of the surface. The same smoothing factor was applied at all phases. To recognize the systolic and diastolic phases, the luminal volumes of all phases were compared. The systolic scan was defined as the one with the largest volume and the diastolic scan as the one with the smallest volume.

Table 3.1: Demographic information of three patients. Note that  $\Delta P$  is the difference between diastolic and systolic pressures,  $Q_{in-vivo}$  denotes the extensional stiffness obtained by [138] and  $Q_{in-vitro}$  is the extensional stiffness obtained by [44].

Patient ID	Sex	Age	$\Delta P$ [KPa] (mmHg)	$Q_{in-vivo}$ [MPa.mm]	$Q_{in-vitro}$ [MPa.mm]
1	M	27	8.66 (65)	1.96	0.78
2	M	84	13.4 (100.5)	6.14	4.11
3	M	61	11.5 (86)	4.6	1.24

#### 3.3.2 Theory of the inverse approach

A set of nodes was defined across each reconstructed aortic geometry, with the requirement that a node represented the position of the same material point at each phase of the cardiac cycle. For this, it was essential to reconstruct a structural mesh for all phases with an identical

number of elements and nodes and to have a mesh morphing function between the geometries of each phase.

VMTK [11] was employed to generate the structural mesh from STL files. The method was based on centerlines and decomposition of the surface into existing branches and mapping each branch onto template parametric coordinates. Once a bifurcation is split into branches, each branch is topologically equivalent to a cylinder and can be mapped onto a set of rectangular parametric coordinates [11]. The approach for mapping the surface of bifurcations consisted of several steps: calculation of centerlines, definition of the reference system, decomposition of the bifurcation into its branches and their parameterization. VMTK provides a technique based on objective criteria capable of generating consistent parameterizations over a wide range of bifurcating geometries. Let  $\partial\Omega_i$  be the surface of the  $i$ th branch which is delimited by two topological circles  $\psi_{i0}$  and  $\psi_{iL}$ . Considering  $u \in [0, L_i]$  is the longitudinal parametric coordinate and  $v \in [-\pi, \pi]$  is the periodic circumferential parametric coordinate, over the parametric space of  $U \subset \mathbb{R}^2$  in the coordinates  $U = (u, v)$ , a bijective mapping is derived as [11]

$$\Phi : \partial\Omega_i \rightarrow U \quad (3.1)$$

such that  $\Phi(\mathbf{x}) = (0, v)$  on  $\psi_{i0}$  and  $\Phi(\mathbf{x}) = (L_i, v)$  on  $\psi_{iL}$ . Longitudinal mapping in VMTK is created by a harmonic and a stretch function to achieve localization with respect to centerline abscissa and reference system [68]. The harmonic function  $f = f(\mathbf{x})$  with  $\mathbf{x} \in \partial\Omega_i$  is computed by solving the elliptic partial differential equation as

$$\Delta_B f = 0 \quad (3.2)$$

where  $\Delta_B$  is the Laplace-Beltrami operator. The longitudinal parametric coordinate is expressed by

$$u(\mathbf{x}) = s \circ f(\mathbf{x}) \quad (3.3)$$

where  $s$  is the stretch function and can be defined as

$$s(f) = \frac{1}{|\lambda(f)|} \int_{\lambda(f)} g(\mathbf{x}) d\lambda \quad (3.4)$$

where  $\lambda(f)$  indicates a level-set of  $f$ . The angular position of each node is determined by a set of normals along the curve of frame  $\tau$ , named  $\mathbf{n}(\tau)$  (which is directed towards the center of the osculating circle of the curve at each point), and its nearest point on the centerline,  $\mathbf{c}(\tau)$ , as

$$v(\mathbf{x}) = \arccos((\mathbf{x} - \mathbf{c}(\tau)) \cdot \mathbf{n}(\tau)) \quad (3.5)$$

where  $\tau$  indicates the different time frames.

One of the requirements is that the inlets and outlets of the imported mesh into VMTK should be open. Left subclavian artery, brachiocephalic artery, left common carotid artery and coronary artery branches were used to provide anatomical references to ensure that the measurements taken at different phases of the cardiac cycle were at the same location in the aorta (see Fig. 3.1). Eventually, the extracted data from VMTK were postprocessed in Matlab to extract

an accurate mesh using the longitudinal and circumferential metrics obtained from VMTK. A template meshgrid with an arbitrary number of points was created in the  $u_{\text{temp}} \in [u_{\min}, u_{\max}]$  and  $v_{\text{temp}} \in [-\pi, \pi]$  domain. A polynomial approximation was implemented around each node of the template meshgrid. For instance, let  $(u_{\text{temp}}^i, v_{\text{temp}}^i)$  denote the parametric coordinates of node  $\mathbf{X}_i$ . Let  $(\mathbf{u}_{\text{nb}}, \mathbf{v}_{\text{nb}})$  be the parametric coordinates of the nodes of the reconstructed STL surface around  $\mathbf{X}_i$ . These nodes were selected such that  $du_j = (u_{\text{nb}}^j - u_{\text{temp}}^i) < \delta_u$  and  $dv_j = (v_{\text{nb}}^j - v_{\text{temp}}^i) < \delta_v$ ,  $\delta_u$  and  $\delta_v$  defining the size of the neighborhood. We assumed  $\delta_u = 8 \text{ mm}$  and  $\delta_v = \pi/5 \text{ rad}$ . Therefore using the least-squares method, the polynomial approximation was written such as

$$\mathbf{A}\mathbf{X} = \mathbf{X}_{\text{nb}} \quad (3.6)$$

with

$$\mathbf{A} = \begin{bmatrix} 1 & du_1 & dv_1 & du_1 dv_1 & du_1^2 & dv_1^2 & du_1^2 dv_1 & du_1 dv_1^2 \\ \vdots & \vdots & \vdots & \vdots & \vdots & \vdots & \vdots & \vdots \\ 1 & du_k & dv_k & du_k dv_k & du_k^2 & dv_k^2 & du_k^2 dv_k & du_k dv_k^2 \\ \vdots & \vdots & \vdots & \vdots & \vdots & \vdots & \vdots & \vdots \\ 1 & du_n & dv_n & du_n dv_n & du_n^2 & dv_n^2 & du_n^2 dv_n & du_n dv_n^2 \end{bmatrix} \quad (3.7)$$

$$\mathbf{X} = \begin{bmatrix} X_1 & Y_1 & Z_1 \\ X_2 & Y_2 & Z_2 \\ \vdots & \vdots & \vdots \\ X_8 & Y_8 & Z_8 \end{bmatrix} \quad (3.8)$$

and

$$\mathbf{X}_{\text{nb}} = \begin{bmatrix} X_{\text{nb}}^1 & Y_{\text{nb}}^1 & Z_{\text{nb}}^1 \\ \vdots & \vdots & \vdots \\ X_{\text{nb}}^k & Y_{\text{nb}}^k & Z_{\text{nb}}^k \\ \vdots & \vdots & \vdots \\ X_{\text{nb}}^n & Y_{\text{nb}}^n & Z_{\text{nb}}^n \end{bmatrix} \quad (3.9)$$

Based on a mesh sensitivity analysis, an average mesh size of  $1 \times 1 \text{ mm}$  was used. According to Wittek et al [151] who observed that the ascending thoracic aorta experiences clockwise and counterclockwise twist, we derived the time variations of the circumferential coordinate,  $v$ , of coronary arteries in the space of parametric coordinate and subtracted this value from the circumferential coordinate of the assumed reference phase in order to apply torsion during aortic wall motion. To adjust all phases longitudinally, the origin of  $u$  was set in the coronary plane at each phase. Accordingly, the torsion was applied by subtracting the shift of the  $v$  value at the inlet, and by subtracting a shift in the  $v$  value all along the thoracic aorta, varying linearly from  $v$  to 0 between the inlet and the position of the brachiocephalic artery.

Any periodic function (in this case nodal coordinates of all phases,  $x(t)$ ) can be expressed as a weighted sum of infinite series of sine and cosine functions of varying frequency. Therefore,



having the structural mesh of all ten phases, a discrete Fourier transform was employed such as

$$x(t) = a_0 + \sum_{n=1}^{\infty} \left( a_n \cos(nft) + b_n \sin(nft) \right) \quad (3.10)$$

where  $a_0$  is the Direct Current (DC) term and the sum is the fundamental magnitude of the time-varying node positions when  $n=1$  while  $f$  is the fundamental frequency. A strain analysis was performed on the average geometry (defined by using the DC terms of all nodal positions) by applying displacements (including torsion) at each node corresponding to the fundamental term obtained from the Fourier transform in Eq. 3.10. As the fundamental term is complex, the real and the imaginary parts are applied separately at the corresponding nodes (in their average position, defined by the DC term) using the finite element method (FEM). Eventually the reconstructed strain components were also complex. The components in the longitudinal and circumferential directions were derived respectively as

$$\begin{aligned} \varepsilon_1^{\text{com}} &= \varepsilon_1^r + i\varepsilon_1^{\text{im}} \\ \varepsilon_2^{\text{com}} &= \varepsilon_2^r + i\varepsilon_2^{\text{im}} \end{aligned} \quad (3.11)$$

where superscripts "*r*" and "*im*" indicate real and imaginary contributions, respectively. Therefore the magnitude of strains in the longitudinal and circumferential directions can be respectively obtained as

$$\begin{aligned} \varepsilon_1 &= \sqrt{\varepsilon_1^{r^2} + \varepsilon_1^{\text{im}^2}} \\ \varepsilon_2 &= \sqrt{\varepsilon_2^{r^2} + \varepsilon_2^{\text{im}^2}} \end{aligned} \quad (3.12)$$

The results of the strain computation are independent of the chosen material properties and this methodology is applicable to finite deformation problems. Although the aortic tissue is

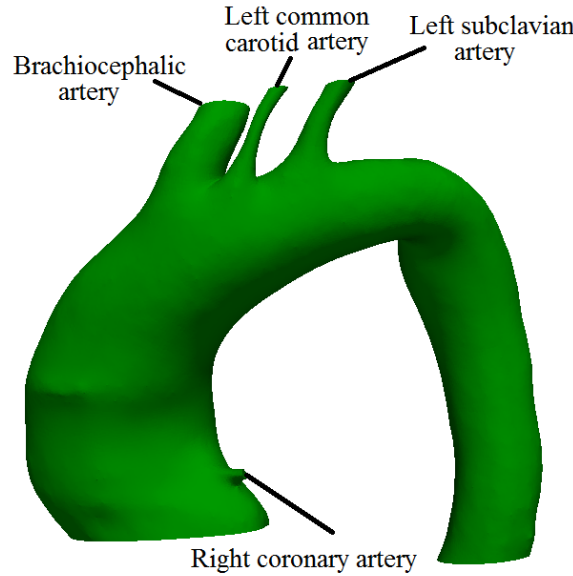


Figure 3.1: Segmentation of the aortic geometry for diastolic phase. Including left subclavian artery, brachiocephalic artery, left common carotid artery and coronary artery branches which are used as anatomical references.

globally anisotropic and nonlinear, we linearized here its mechanical behaviour in the range of strains induced by pressure variations between diastole and systole, and neglected anisotropic effects in this range too. The constitutive equations reduced to Hooke's law in plane stress. Due to the spatial resolution of CT, the local aortic thickness cannot be measured accurately *in vivo*. The thickness was previously measured *in vitro* on the excised sample after the surgery [44]. However, the *in vitro* measurement is performed when the tissue is loadfree, whereas the tissue is stretched and pressurized *in vivo*. Therefore the thickness can vary significantly *in vivo*, thus to express the Hooke's law, we wrote the membrane tensions,  $\tau$ , as

$$\begin{aligned}\tau_1(t) &= \tau_1^0 + Q(\varepsilon_1(t) + \nu\varepsilon_2(t)) \\ \tau_2(t) &= \tau_2^0 + Q(\nu\varepsilon_1(t) + \varepsilon_2(t))\end{aligned}\tag{3.13}$$

where  $\tau_1^0$  and  $\tau_2^0$  are the DC terms of both components of the membrane tension (representing pretensions existing in the average geometry due to average blood pressure and axial tension),  $Q$  is the extensional stiffness and  $\nu$  is the Poisson's ratio in which incompressibility is assumed ( $\nu=0.49$ ). We derived  $\tau_1^0$  and  $\tau_2^0$  by achieving an FE stress analysis on the average geometry under the effect of the average pressure  $P_0$  using the approach proposed by [85].

As shown in Fig. 3.2 it is assumed that each element of the arterial wall is a finite sector of an ellipsoidal membrane with radii  $r_1$  and  $r_2$  in both circumferential and longitudinal directions. Then, in the framework of these assumptions, local equilibrium equations can be written as

$$P(t) = \frac{\tau_1(t)}{r_1(t)} + \frac{\tau_2(t)}{r_2(t)}\tag{3.14}$$

where  $r_1$  and  $r_2$  are the radii of the element sector in both directions (major and minor) as shown in Fig. 3.2 and  $P$  is the applied pressure. Using  $P_0$  to denote the DC term of pressure variations, and neglecting second order variations, Eq. 3.14 can be rewritten:

$$\begin{aligned}P(t) - P_0 &= \frac{\tau_1(t) - \tau_1^0}{r_1^0} + \\ &\frac{\tau_2(t) - \tau_2^0}{r_2^0} - \frac{\tau_1^0(r_1(t) - r_1^0)}{(r_1^0)^2} - \frac{\tau_2^0(r_2(t) - r_2^0)}{(r_2^0)^2}\end{aligned}\tag{3.15}$$

Using  $\Delta P$ ,  $\Delta\tau_1$ ,  $\Delta\tau_2$ ,  $\Delta r_1$  and  $\Delta r_2$  to denote the fundamentals of pressure, the circumferential and longitudinal components of the local tension tensor, and the circumferential and longitudinal radius of curvature, respectively, Eq. 3.15 can be written as follows:

$$\Delta P = \frac{\Delta\tau_1}{r_1^0} + \frac{\Delta\tau_2}{r_2^0} - \frac{\tau_1^0(\Delta r_1)}{(r_1^0)^2} - \frac{\tau_2^0(\Delta r_2)}{(r_2^0)^2}\tag{3.16}$$

In the following, we assume  $\Delta P = (P_{sys} - P_{dias})/2$ .

Substituting Eqs. 3.13 in 3.16, we obtain the extensional stiffness for each element such as

$$Q = \frac{\Delta P + \frac{\tau_1^0 \Delta r_1}{(r_1^0)^2} + \frac{\tau_2^0 \Delta r_2}{(r_2^0)^2}}{\frac{\varepsilon_1(t) + \nu\varepsilon_2(t)}{r_1^0} + \frac{\nu\varepsilon_1(t) + \varepsilon_2(t)}{r_2^0}}\tag{3.17}$$

To obtain  $r_1$  and  $r_2$  fast and efficiently, we developed a method based on the principle of virtual work as previously introduced in [19], assuming stresses  $\boldsymbol{\sigma}$  at equilibrium with external loads  $\mathbf{T}$  should satisfy the following equation:

$$\int_v \sigma_{ij} : \varepsilon_{ij}^* d\nu + \int_{\partial\nu} T_i u_i^* ds = 0 \quad (3.18)$$

where  $v$  is the volume of the domain of interest,  $\partial\nu$  is its surface boundary,  $\mathbf{u}^*$  is a virtual continuous displacement field and  $\boldsymbol{\varepsilon}^*$  are the virtual strains related to the gradients of the virtual displacements. As this equation is valid for any virtual field,  $\mathbf{u}^*$  can be defined as a unit vector oriented along the normal directions of the aortic wall at every node (directions  $n_{1,2,3,4}^n$  in Fig. 3.2) to inflate the aorta virtually. Accordingly, it is possible to derive the following local equation:

$$\sigma_1 h \varepsilon_1^* + \sigma_2 h \varepsilon_2^* = p u^* \quad (3.19)$$

where  $\sigma_1$  and  $\sigma_2$  are the principal components of the stress and  $h$  is the thickness. The Laplace

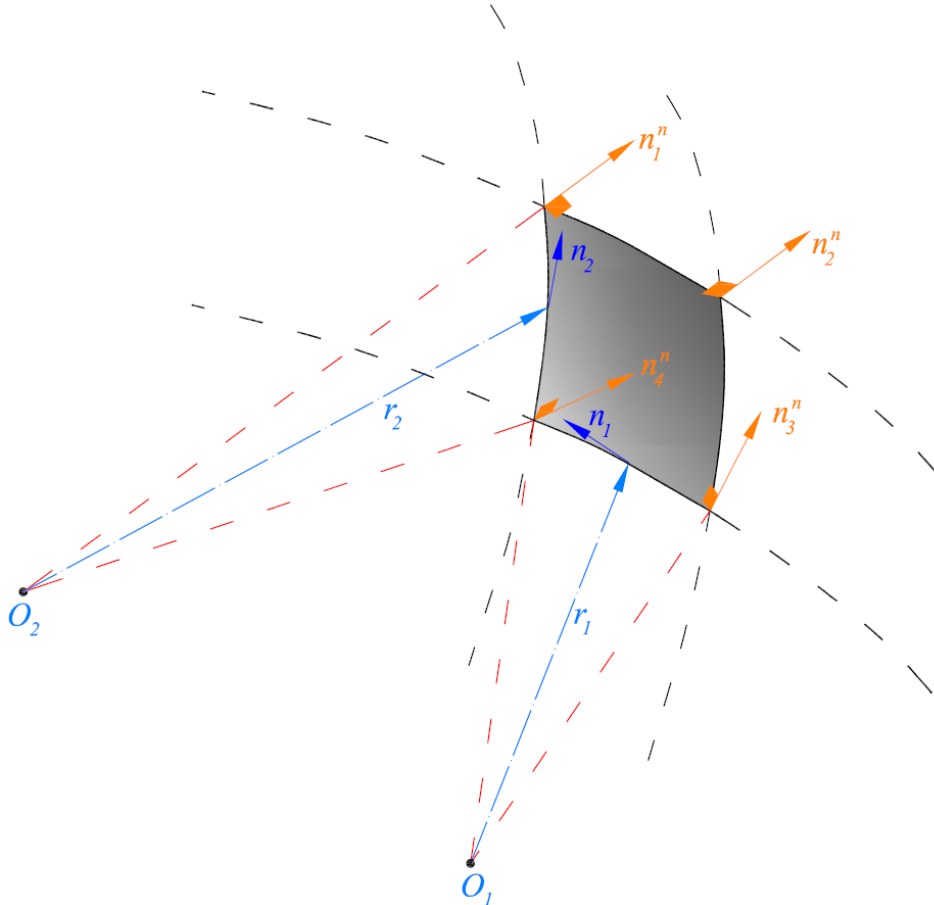


Figure 3.2: It is assumed that each element of the arterial wall is a finite sector of an ellipsoidal membrane with radii  $r_1$  and  $r_2$  in both circumferential and longitudinal directions.  $n_1$  and  $n_2$  are tangential unit vectors normal to  $r_1$  and  $r_2$ , respectively.  $n_i^n$  with  $i=\{1,2,...,4\}$  is normal unit vector at each node of the element.

law may be written:

$$\frac{\sigma_1}{r_1}h + \frac{\sigma_2}{r_2}h = p \quad (3.20)$$

By identification between the two previous equations, we obtain directly a relationship between the local radii of curvature and the virtual strain fields:

$$\begin{aligned} \frac{1}{r_1} &= \frac{\varepsilon_1^*}{u^*} \\ \frac{1}{r_2} &= \frac{\varepsilon_2^*}{u^*} \end{aligned} \quad (3.21)$$

In the current study we used the concept of "extensional stiffness" which equals the material stiffness times the thickness and whose dimension is MPa.mm.

Stiffness variations across the different regions of the thoracic aorta may exist at different scales. In order to filter out high frequency variations, the obtained results were eventually fitted using Fourier polynomial of order 4 along the circumferential directions and polynomials of order 3 along the axial direction, permitting a smoother estimation of stiffness distribution.

### 3.3.3 Numerical implementation

We reconstructed ascending and descending aortas excluding all branches. Therefore, the right coronary and brachiocephalic arteries were used as reference points to obtain identical parts of the ascending aorta at different phases and the left subclavian artery was used as a reference point to consider identical parts of the descending aorta at different phases. For each patient and each phase, a structural mesh using quadrilateral elements with four nodes was prepared and then the average structural meshes of ascending and descending aortas were obtained by averaging the nodal positions throughout the cardiac cycle. Afterwards, for each aorta, the Abaqus FE software [72] was employed to calculate  $\varepsilon_1^*$  and  $\varepsilon_2^*$  by applying  $u^*$  at each node in normal directions of  $n_1^n:n_4^n$  in Fig. 3.2. Moreover, two other independent FE analyses were performed by applying corresponding real and imaginary displacements at each node (including aorta torsion) to calculate  $\varepsilon_1^{\text{com}}$  and  $\varepsilon_2^{\text{com}}$  and subsequently  $\varepsilon_1$  and  $\varepsilon_2$  expressed in Eq. 3.12. For each FE analysis, orientation user subroutine (ORIENT) was employed to assign local material directions in order to save results in the local coordinate system. Each geometry was a non-perfectly cylindrical geometry so that the radial direction (normal to the artery) was defined as the outward normal direction to each element, the axial direction was defined as the direction parallel to the luminal centerline in the direction of the blood flow, and the circumferential direction was perpendicular to both previously defined directions. To calculate and visualize the local extensional stiffness expressed in Eq. 3.17, a user material subroutine (UMAT) and a user-defined external databases (UEXTERNALDB) were coupled with the commercial FE software Abaqus [72]. The complete methodology is summarized in a flowchart shown in Fig. 3.3.

In summary, we had to perform several different steps to characterize the local aortic stiffness for each patient. The most time consuming step was the segmentation of CT images (cleaning could last one day for the noisiest). Generation of the structural mesh took about 10 minutes

including VMTK and further processing. It took less than 2 hours to prepare the ABAQUS input files for stress analyses, strain analyses, stiffness assessment and reconstruction. Each ABAQUS resolution took about five minutes.

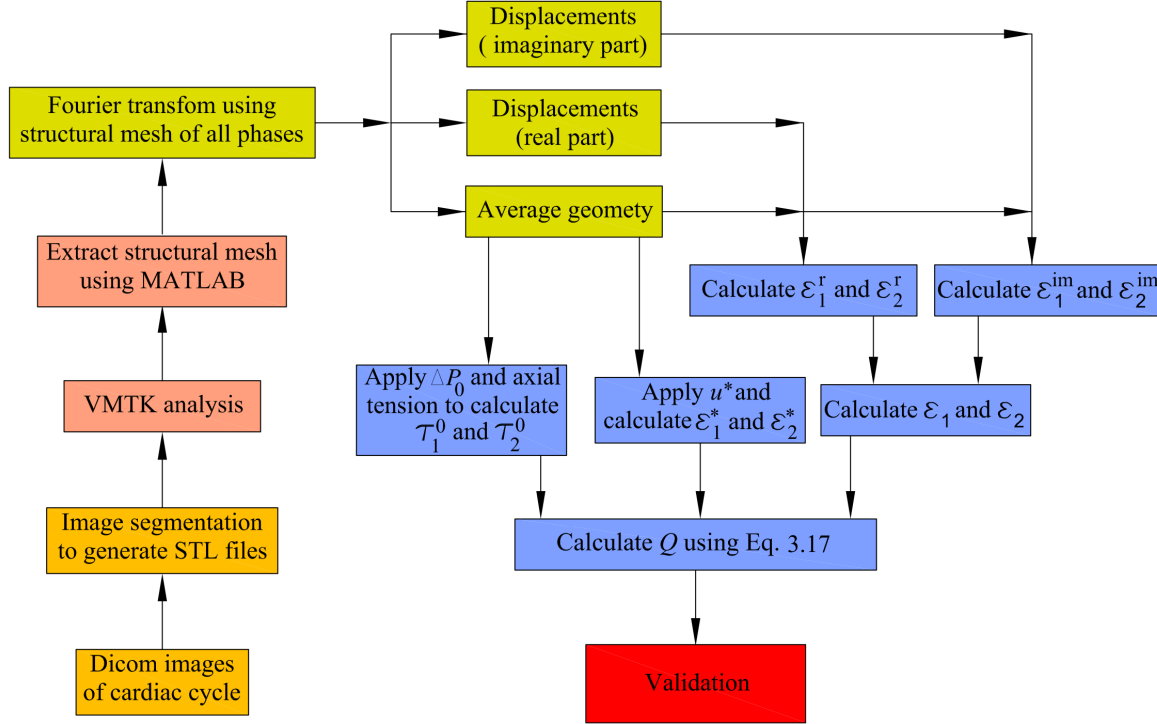


Figure 3.3: Flowchart of the methodology to identify local extensional stiffness of aorta.

## 3.4 Results

### 3.4.1 Numerical verification

Numerical validation was performed considering two different material behaviors: linear isotropic elasticity and non-linear anisotropic hyperelasticity.

### 3.4.2 Linear elastic material property

For the sake of validation, we used a reference aortic geometry (RG) and we created numerically a deformed aortic geometry (DG) by considering the effects of an average intramural pressure ( $P=40$  mmHg (5.33 KPa)) onto the aorta modeled with a linear elastic behavior. The DG was derived by a finite element analysis using the raw STL mesh of the reference geometry. Two analyses (cases) were performed: one with a homogeneous stiffness in the whole aorta and another one with a heterogeneous stiffness distribution in which three regions were defined in the aorta, each one with a different stiffness as shown in Fig. 3.6. Each analysis provided a deformed STL mesh. Displacement maps used to reconstruct DG are shown in Fig. 3.4. Having in hand RG and DG for both cases, we performed our approach using VMTK and MATLAB

to independently generate the structural mesh of each geometry. For the sake of validation, we subtracted the nodal coordinates of both structural meshes (on RG and DG). As can be observed in Fig. 3.5, we found a good agreement between the displacements reconstructed using our approach and the reference displacement, indicating that structural meshes of both geometries are related to nearly similar material points. After this first validation on the reconstructed displacement data, we applied the whole methodology with reconstruction of stiffness distributions from the two simulated cases. For each case, a stiffness distribution was obtained and compared to the reference one (Fig. 3.6). The reconstructed stiffness was in good agreement with the reference and especially the local heterogeneity could be well retrieved for the heterogeneous case. Artifacts only appear very locally at the proximal and distal parts of the aortic segment due to spurious effects of polynomial smoothing close to the boundary (edge effects).

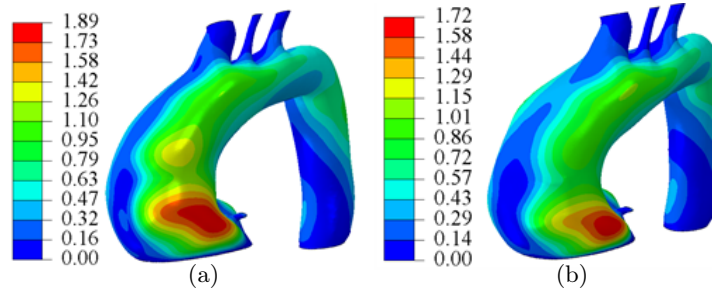


Figure 3.4: Map of the displacement magnitude [mm] after inflation of the reference geometry (RG) using FE analysis considering a- a homogenous stiffness and b- a heterogeneous stiffness distributions.

### 3.4.3 Non-linear anisotropic material property

We have performed a complementary validation of our methodology considering anisotropy and effects of nonlinearity. We used the same aortic geometry (raw stl) as the one used for the linearized case study, which is the aortic geometry of a real patient which was segmented from a CT scan obtained at  $P_{diastole}=80$  mmHg (10.66 KPa). We modeled the aortic wall with a Gasser-Ogden-Holzapfel anisotropic strain energy function which may be written as [75]

$$\bar{\Psi} = C_{10}(\bar{I}_1 - 3) + \frac{k_1}{2k_2} \sum_{i=4,6} [\exp[k_2(\bar{I}_i - 1)^2] - 1] + \kappa(J - 1)^2 \quad (3.22)$$

where  $C_{10}$  and  $k_1$  are material parameters and have a stress-like dimension, and  $k_2$  is a dimensionless material parameters while  $\kappa$  is the bulk modulus and  $J$  is the Jacobian.  $\bar{I}_1 = \text{tr}(\bar{\mathbf{C}})$ ,  $\bar{I}_4 = \bar{\mathbf{C}} : \mathbf{a}_{01} \otimes \mathbf{a}_{01}$  and  $\bar{I}_6 = \bar{\mathbf{C}} : \mathbf{a}_{02} \otimes \mathbf{a}_{02}$  are respectively the first, fourth and sixth invariant of the modified counterparts of the right Cauchy-Green tensor,  $\bar{\mathbf{C}}$ . Note that the two families of collagen fibers are characterized by two orientation vectors  $\mathbf{a}_{01} = [0 \cos\theta \sin\theta]$  and  $\mathbf{a}_{02} = [0 \cos\theta -\sin\theta]$ , where  $\theta$  is the orientation angle.

Two analyses were performed: One with a homogeneous distribution of hyperelastic material

properties in the whole ascending thoracic aorta and the other with a heterogeneous distribu-

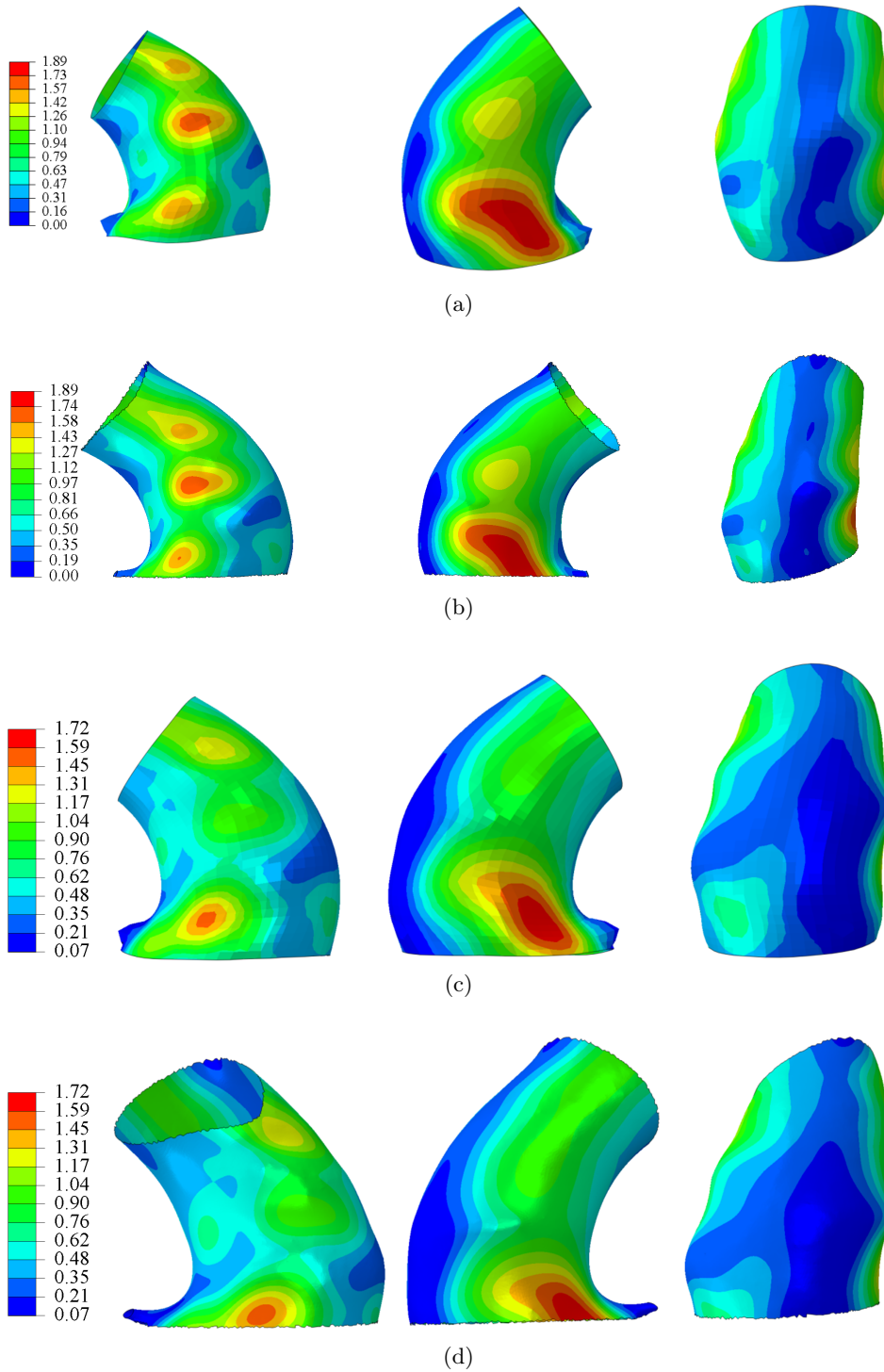


Figure 3.5: a- Displacement maps [mm] obtained by our methodology considering a homogenous stiffness, b- Reference displacement maps obtained using a finite element analysis considering a homogenous stiffness, c- Displacement maps obtained by our methodology considering a heterogeneous stiffness distribution, d- Reference displacement maps obtained using a finite element analysis considering a heterogeneous stiffness distribution.

tion of hyperelastic material properties, considering three regions. Material parameters used for this validation study are reported in Table 3.2. Before applying these two models to calculate displacements between diastole and systole, we first computed the zero pressure geometry in each case using the approach presented by Mousavi et al [104,105]. Afterwards, we calculated the deformation of the aortic geometry for a systolic pressure directly by applying  $P_{systole}=120$  mmHg (16 kPa) onto the zero pressure geometry.

Having in hand the diastolic geometry and the computed systolic geometry, we applied our approach using VMTK and MATLAB to independently generate the structural mesh of each geometry (systolic and diastolic) in both homogeneous and heterogeneous analyses. We subtracted the nodal coordinates of both structural meshes (systolic and diastolic phases) to obtain the displacements between systole and diastole for each case. Assuming the diastolic phase as the reference geometry we applied our methodology to retrieve the local aortic stiffness properties. The identified results shown in Fig. 3.7 demonstrate that our methodology is able to retrieve the "stiff" region in the heterogeneous case, whereas the homogeneous case show only small variations which are mostly related to edge effects. However, this remains a qualitative

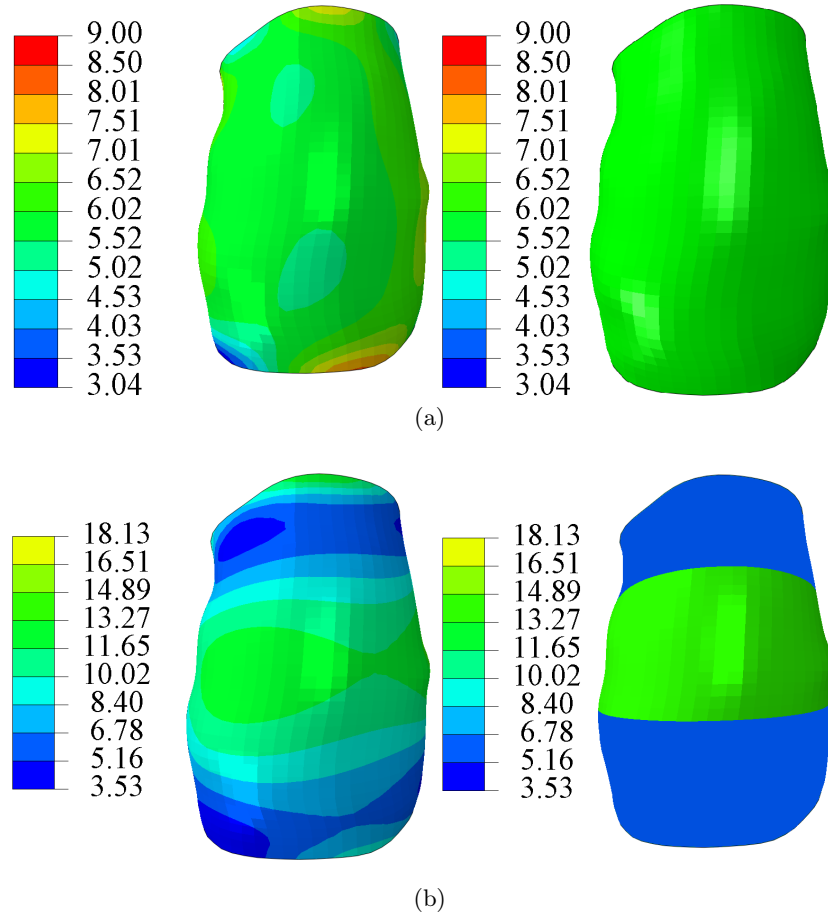


Figure 3.6: Validation study: stiffness map [MPa.mm] reconstructed using our methodology (left) for the assigned homogeneous stiffness (right)(a). Stiffness map reconstructed using our methodology (left) for the assigned heterogeneous stiffness (right)(b).



comparison as the obtained linearized stiffness is not directly related to hyperelastic properties. This qualitative validation completes well the previous quantitative validation where we modeled the aorta with a linear elastic behavior and where we were able to retrieve the correct stiffness properties.

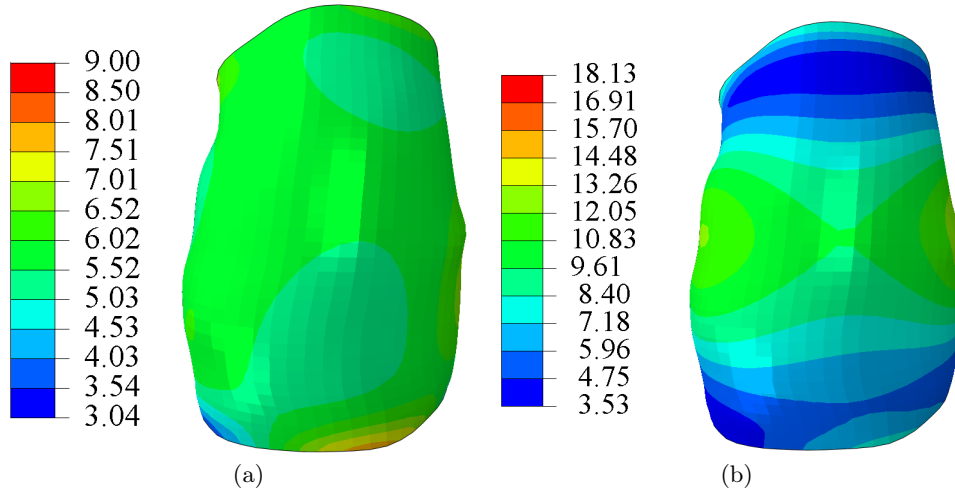


Figure 3.7: Validation study: stiffness map [MPa.mm] reconstructed using our methodology considering a- homogeneous and b- heterogeneous hyperelastic anisotropic material properties.

#### 3.4.4 Patient-specific results

The methodology described previously was applied on 3 patients. The extensional stiffness of their aorta was reconstructed at every Gauss point of the mesh (excluding the branches and the region of the arch between the brachiocephalic and the left subclavian arteries) and then the values were interpolated at nodal positions. The results were plotted as independent colormaps which are shown in Fig. 3.8. The distributions appear heterogeneous, especially in the ATAA regions where some regions of relatively higher extensional stiffness appear. The distribution of local extensional stiffness showed higher values for ascending aortas compared to descending aortas.

Table 3.2: Values of non-linear anisotropic material parameters for homogeneous and heterogeneous models

	$C_{10}$ [kPa.mm]	$k_1$ [kPa.mm]	$k_2$	$\theta_1$ [°]	$\theta_2$ [°]
Homogenous	30	500	5	35	-35
Heterogeneous stiff	60	1000	5	35	-35
Heterogeneous compliant	30	500	5	35	-35

### 3.4.5 Comparison of the results

For these 3 patients, elastic properties of their ATAA were previously characterized with two other methods:

1. An ATAA segment was defined by two transverse planes located respectively at 10 cm and 55 cm from the coronary artery. Across the defined segment, the average distensibility of the ascending thoracic aorta was assessed from CT scans according to [138]

$$D_V = \frac{\Delta V}{V \Delta P} \quad (3.23)$$

where  $V$ ,  $\Delta V$  and  $\Delta P$  are respectively the luminal volume, the volume difference between diastole and systole and the pressure difference. The extensional stiffness was deduced as the ratio between the distensibility and the average diameter of the segment. Let  $Q_{in-vivo}$  denote the extensional stiffness obtained with this method.

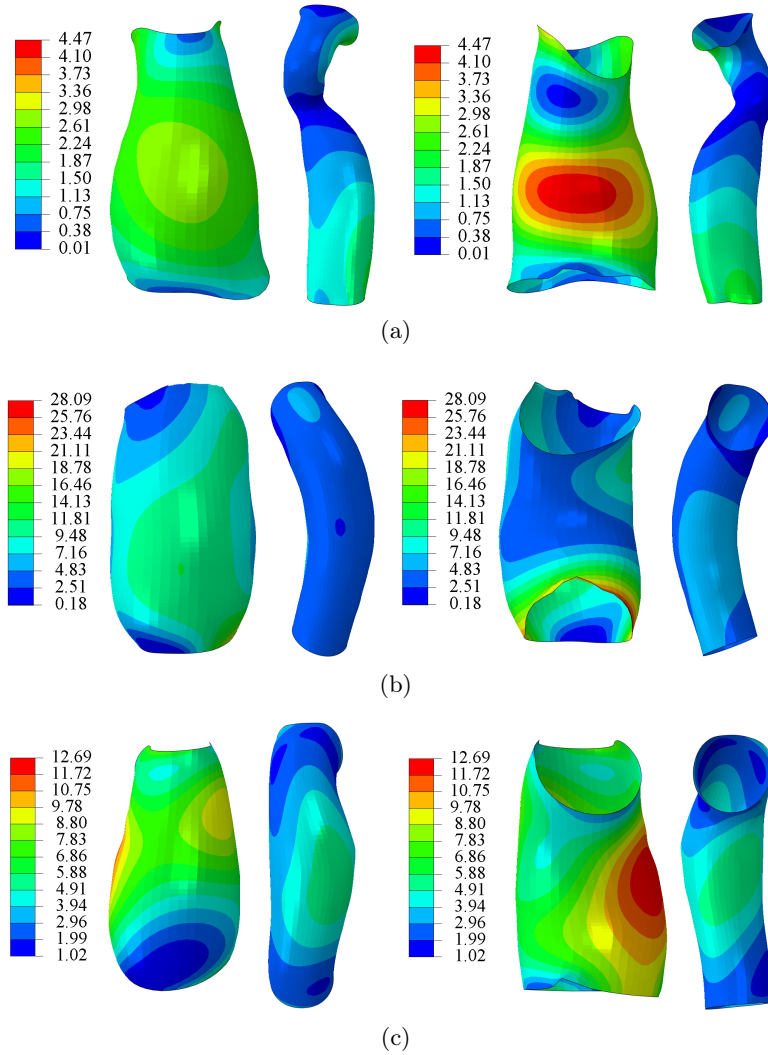


Figure 3.8: Distribution of local extensional stiffness [MPa.mm] in ascending and descending aortas for Patient 1 (a), Patient 2 (b) and Patient 3 (c). Left and right show frontal and distal views respectively.

2. After the surgical intervention on these patients, an ATAA segment was excised. From this segment, a square ( $45 \times 45 \text{ mm}$ ) was cut in the outer curvature region and tested in bulge inflation. The stress–strain response of the tested sample was linearized over a range of pressures inducing similar tensions in the tissue as the tensions produced by diastolic and systolic pressures. The obtained linearized stiffness of the tissue over this range, multiplied by tissue thickness, yielded another estimate of the extensional stiffness, which was denoted  $Q_{in-vitro}$ .

Therefore, for each patient, we focused on the distribution of extensional stiffness across the ATAA segment and across the cut square (Fig. 3.9). For the sake of statistical analysis, we derived the median and interquartile ranges of all nodal values of the identified extensional stiffness (Fig. 3.10). The analysis was achieved first by taking all the values of the ascending aorta, then only the values in the ATAA segment and finally only the values of the cut square. For each patient, we also plotted in Fig. 3.10 the  $Q_{in-vitro}$  and  $Q_{in-vivo}$  values obtained by [44] and [138], respectively. This analysis showed that the median and interquartile values for different cuts of all patients are relatively at the same ranges. Comparing the interquartile box obtained in this study with the corresponding results of [138], it can be deduced that for all patients  $Q_{in-vivo}$  is a value between the lower and the median value (mostly close to median) while  $Q_{in-vitro}$  values are close to lower corresponding interquartile. This can be explained by the mechanical actions of surrounding tissues and environment *in vivo*, which may apply a counter pressure on the artery. We did not take into account this counter pressure in the identification as  $P(t)$  in Eq. 3.14.

## 3.5 Discussion

In this paper we have introduced an original method to reconstruct the stiffness distribution of the thoracic aorta from gated CT images considering ten phases of a cardiac cycle. This methodology requires tracking the deformations of the aortic wall throughout a cardiac cycle from the gated CT images. The deformations were tracked without any additional information or marker indicating heterogeneous deformation in between the bifurcations.

### 3.5.1 General remarks

For the first time ever, regional variations of stiffness properties across ATAA were reconstructed on 3 patients non-invasively. To achieve this reconstruction, a novel non-invasive inverse method was developed based on preoperative gated CT scans. The non invasive identification of elastic properties of ATAA is highly important as our research group [44,138] recently showed that the extensional stiffness is significantly correlated with the stretch based rupture risk of ATAA. Therefore, it is significantly interesting to obtain the local extensional stiffness of the ascending thoracic aorta to detect pathological regions with the highest risks of rupture. Interestingly, our results indicate that the local extensional stiffness is higher in the aneurysmal ascending thoracic aorta than in the descending aorta, and that the values are relatively higher

than stiffness properties reported for healthy aortas. However, despite this general trend, the distribution of extensional stiffness is heterogeneous in the aneurysmal region, with large stiffness in the bulging part of aneurysm. The local loss of elasticity can be related to a more pronounced local remodeling with, for instance, a larger fraction of collagen fibers. Sassani et al [124] showed a large distribution of fiber orientations spanning from circumferential to longitudinal directions, which was also supported by [131] stating that ATAA had no effect on strength. However, this can cause stiffening and extensibility reduction, corroborated with histological observation of elastin degradation but not collagen content. It could be interesting also to check the possible correlation of these regions with local concentration of wall shear stress induced by the blood flow [97]. All these possible correlations between regional variations of extensional stiffness and local tissue composition or local hemodynamics effects are currently under study in our group on a cohort of patients. Over the past decades the biomechanical properties of the aorta have been widely investigated [30,43,58,62,73,102,109,118,129,146]. As the aortic tissues are intrinsically anisotropic, the identified stiffness provided by our method combines effects of the axial and circumferential extensional linearized stiffness. However, as

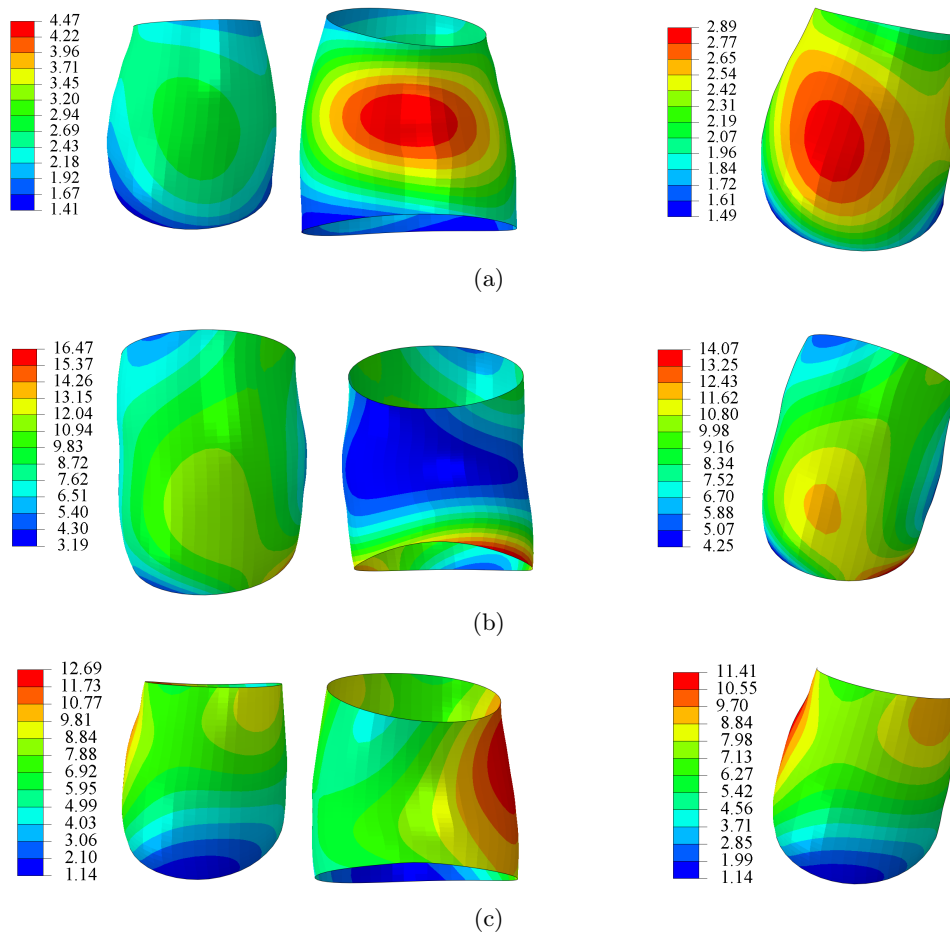


Figure 3.9: Distributions of local extensional stiffness [MPa.mm] for Patient 1 (a), Patient 2 (b) and Patient 3 (c). Results on the left shows frontal and distal views of *in vivo*. Results on the right demonstrates *in vitro* cut.

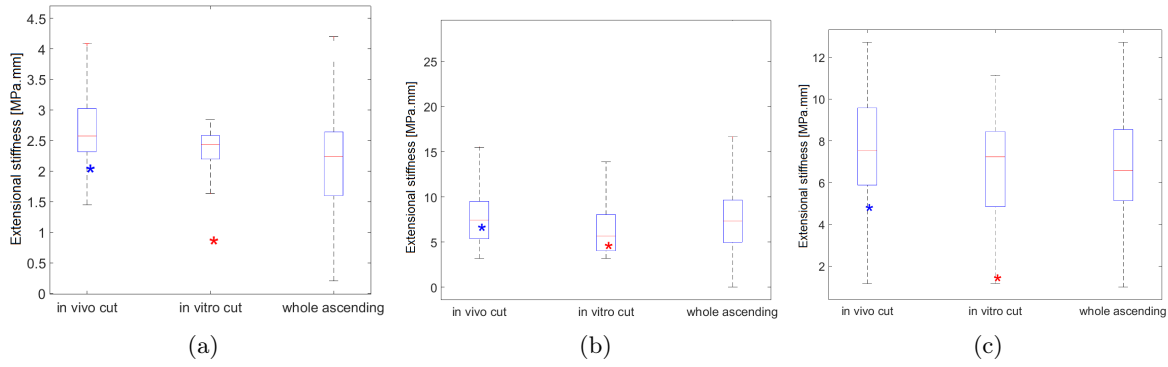


Figure 3.10: Median and interquartile range of the local extensional stiffness [MPa.mm] obtained for *in vivo* cut, *in vitro* cut and whole ascending for Patient 1 (a), Patient 2 (b) and Patient 3 (c). The blue and the red stars demonstrate the values of *in vivo* and *in vitro* cuts, respectively, which are calculated by [138] and [44].

we use only the pressure loading to solve the identification problem (we have no information on the axial tension *in vivo*), it is dominated by effects of the circumferential extensional linearized stiffness. This is in agreement with conclusions of Ferrara et al. [53] who indicated that the weight of the circumferential elastic modulus is significantly higher than the weight of the longitudinal one in the aortic mechanical response to pressure variations. The maximum circumferential elastic modulus was reported in posterior region. Moreover, their results indicate that regardless of age and gender, the mean elastic modulus is larger in the circumferential direction. However aging reduces the mean elastic modulus and male has higher mean elastic modulus in comparison with female. Iliopoulos et al [82] support these results and state that circumferential specimens were stiffer than longitudinal ones in the posterior, left lateral, and all regions at physiologic and high stresses but not at low stresses. Furthermore, in agreement with Ferrara et al. [53] they found no significant regional variations of aortic stiffness in the circumferential direction, and similarly at low stresses for longitudinal specimens, while at physiologic and high stresses the right lateral was the stiffest ATAA region. In the other study by the same group [81] it was shown that peak elastic modulus in the anterior region was significantly lower than that in the right, but not the left, lateral and posterior regions. Choudhury et al [30] studied local mechanical properties of healthy and diseased, bicuspid and tricuspid aortic valves (BAV and TAV), human ascending aorta. Indicating that BAV tissue was the thinnest and contained the largest fraction of collagen, they found significantly less elastin both in TAV and BAV tissue in contrast to healthy tissue, while on average the smallest stiffness was observed in TAV patients. The elastic modulus was not dependent on direction (isotropic) but it was dependent on the quadrant and tissue type. The medial quadrant was the most compliant and the lateral quadrant tissue was the stiffest.

Although most of these previous investigators carried out experimental tests on tissue samples excised from patients during surgery, or on cadavers, the material properties of tissues are commonly characterized on average across these samples and in conditions which may be far

from *in vivo* conditions, such as for instance tensile test. Only recently, the use of digital image correlation (DIC) has made it possible to investigate the local material properties of excised aortic samples [13, 38, 39]. Inverse methods were developed to process DIC measurements and reconstruct the regional variations of material properties, as for instance using a tension inflation tests keeping the cylindrical shape of the aorta [19]. Regional variations of constitutive properties make sense as they can be related to local tissue adaptation through growth and remodeling [79].

When excised aortic samples are tested *in vitro*, the results usually take the form of constitutive parameters in a strain energy density function [74]. Strain energy density functions usually have a large number of constitutive parameters with possible couplings between each other and it was recently suggested to evaluate more functional parameters, such as for instance the linearized *in vivo* stiffness [19]. Here, we focused only on this linearized *in vivo* stiffness as we had only a non invasive loading of the aorta across a limited range of strains through the variations of blood pressure. The non invasive identification of the aortic stiffness was previously achieved on average across aortic segments either by measuring the aortic distensibility [138] or by measuring the pulse wave velocity [65], and relating these quantities to the aortic stiffness. Local non invasive identification was previously achieved using 4D ultrasound on the abdominal aorta [85, 150] but the present study is the first one using gated CT scans and applying the approach onto the ascending thoracic aorta. The availability of these images allowed us to model subject-specific arterial configurations. Since a correlation between the stretch-based rupture risk and the tangent elastic modulus was found by [44], the methodology proposed here has potential to identify the rupture risk of aorta according to calculated local extensional stiffness.

It is important to point out the benefit of using a Fourier analysis (as done here for the regional reconstruction) instead of using simply diastolic and systolic geometries of the aorta (as done for distensibility measurements). Indeed, the distensibility is usually assessed by measuring the change of cross section area of the aorta between diastole and systole, diastole being defined as the stage with minimum cross section area and systole being defined as the stage with maximum cross section area. There is always a significant uncertainty on the times at which the 10 phases of CT scans are acquired. If we could reduce this uncertainty and provided that a pressure curve can be measured simultaneously, the method could be easily extended to derive time variations of the stiffness throughout the whole cardiac cycle. However, we noticed that locally, the maximum deflection of the aorta, and its maximum strains, are not reached at the same stage of the cardiac cycle depending on the position (Fig. 3.1). It means that the response of the aorta to the pressure variations presents phase shifts depending on the position. These phase shifts are potentially the result of viscous effect but also of the combined action of the blood pressure and of the cardiac motion, which are not synchronized, as this was previously shown by [151]. Due to these local phase shifts, it happens that the maximum strain of the aorta is not reached at systole for all the positions and the minimum strain of the aorta is not reached at diastole. Therefore, taking the average change of strain between diastole and systole to derive

the aortic stiffness, as done in the distensibility method [44,138], automatically underestimates the actual strain variations occurring throughout a cardiac cycle. The consequence of this strain underestimation should be a stiffness overestimation for the distensibility method. However, in this work, it can be compensated by another effect which we would like to point out as well. Commonly, pressure variations are linearly related to stress variations without considering the effects of radius variations as we did in Eq. 3.16. However, we found that the term considering the effects of radius variations, namely  $\frac{\tau_1^0(\Delta r_1)}{(r_1^0)^2} - \frac{\tau_2^0(\Delta r_2)}{(r_2^0)^2}$ , is on average responsible for about 10% of  $\Delta P$ , with local effects possibly reaching 50%. Neglecting this term, as it is traditionally done in distensibility assessment, induces an underestimation of stress variations. Combined with the strain underestimation explained previously, the stress underestimation results in a good agreement of the distensibility method with our novel inverse method. Nevertheless, future stiffness identifications should take into account all these effects as done in the current study.

### 3.5.2 Limitations

There are several limitations in this work which are discussed below:

- The inverse approach is based on local equilibrium equations similar to those derived in [19]. These equations are obtained based on the principle of virtual work. It is worth noting that they are equivalent to the generalized Laplace's law which writes the local equilibrium between pressures and tensions in a membrane. Accordingly, it means that it is assumed that the aortic wall behaves as a membrane with no bending moments or no through thickness shear. Regions near the branches may not satisfy the membrane assumption, and were removed from the analysis.
- The present study used gated CT scans as a source of dynamic images of the aortic wall during the cardiac cycle. The use of Xray may present a limitation for an extensive use of the methodology, especially if one wants to repeat the identification of aortic stiffness at different ages of ATAA growth, which would induce repeated irradiation for the patient. We are currently working on an extension of the method to images acquired with 4D MRI.
- The wall is assumed as a linearly elastic material within the systolic-diastolic range and we disregarded the layer-specific wall properties and residual stresses existing in the ATAA wall.
- We here assumed an isotropic behavior of the arterial wall. It was not possible to consider anisotropic effects as only one type of loading was available: variations in blood pressure. The characterization of anisotropic materials requires loading samples in different directions. The consequence of the isotropy assumption in our approach is that the identified extensional stiffness is a combination of the axial and circumferential stiffness, which may be different. However, the local curvatures being involved in Eq. 3.17, most of the weight is put on circumferential effects (the circumferential radius of curvature being

significantly lower than the axial one), meaning that the identified extensional stiffness would be closer to the circumferential stiffness than to the axial stiffness if there was a significant difference between both.

- Average tensions existing in the aorta due to the action of the average blood pressure are also involved in Eq. 3.17. This comes from geometrical nonlinearity involved in finite deformations [18]. These tensions were approximated using the approach of [85]. This approach consists in achieving a linear elastic stress analysis on the same structure as the aorta, assigning a very large elastic modulus. The approach is valid for membrane structures. The membrane assumption was previously shown to be a good approximation for elastostatics of aortic aneurysms [96].
- Due to the removal of in vivo loadings, the artery experiences an elastic recoiling. Even when these loadings are removed, internal or residual stresses still exist in the tissues. An effect of these internal stresses can be observed in arteries with the well-known opening angle [104]. Moreover, Sokolis et al [130] provided evidence of residual stresses in both the circumferential and longitudinal directions considering different wall layers of ATAA. Therefore, disregarding the presence of residual stresses and considering the arterial wall as a 3D membrane with uniform thickness can be considered as additional limitations of the current work. Nevertheless, despite these limitations, the extensional stiffness provided by our methodology is still a useful indicator of local tissue altered remodeling.
- The segmented geometries have some local irregularities (bumps) due to image noise at each phase of the cardiac cycle. The spatial frequency of these irregularities is high and their effect is filtered out by Fourier polynomial smoothing. However, if one wanted to obtain spatial variations of material properties with a higher spatial resolution, one would have to address the issue of these geometric irregularities.

### 3.6 Conclusion

Regional variations of stiffness properties across ATAA were reconstructed in 3 patients non invasively. To achieve this reconstruction, a novel non-invasive inverse method was developed based on preoperative gated CT scans. The non invasive identification of elastic properties of ATAA is highly important as our research group [44, 138] recently showed that the extensional stiffness is significantly correlated with stretch based rupture risk of ATAA. It would be interesting in future studies to consider a cohort with a larger number of patients in order to interpret regional variations of stiffness properties in ATAAs in terms of local hemodynamics effects and of local tissue remodeling.



---

# Chapter 4

## Identifying local arterial stiffness to assess the risk of rupture of ATAA

**Authors:** Solmaz Farzaneh, Olfa Trabelsi, Bertrand Chavent and Stéphane Avril

**Submitted to:** Annals of Biomedical Engineering (under revision)

### Résumé

Nous avons appliqué l'approche du chapitre 3, désignée LESI (identification de la rigidité membranaire locale) sur 11 patients dont le tissu anévrysmal a été caractérisé dans l'essai de gonflement après la procédure chirurgicale pour estimer le critère de risque de rupture. Les tomodensitogrammes et les pressions sanguines systoliques et diastoliques mesurées étaient disponibles avant l'opération. Trois régions ont été définies dans l'aorte thoracique ascendante de chaque patient et une analyse statistique a été effectuée sur la valeur médiane de la rigidité membranaire identifiée dans chacune des 3 régions de l'ATAA. De plus, la valeur de la rigidité membranaire au centre de la coupe située au diamètre maximum a été enregistrée.

### Résultats:

- Nous avons trouvé une très bonne corrélation entre le critère de risque de rupture et la rigidité membranaire locale.
- Nous avons séparé les patients en deux groupes: un groupe d'ATAA rigide et fragile avec un critère de risque de rupture supérieur à 0.9 et un groupe d'ATAA relativement extensibles avec un risque de rupture inférieur à 0.9.
- Les résultats ont montré que la rigidité aortique locale est un indicateur important du risque de rupture de l'ATAA.

## Contents

---

<b>4.1</b>	<b>Abstract . . . . .</b>	<b>69</b>
<b>4.2</b>	<b>Introduction . . . . .</b>	<b>69</b>
<b>4.3</b>	<b>Materials and methods . . . . .</b>	<b>70</b>
4.3.1	The stretch ratio risk criterion . . . . .	70
4.3.2	The LESI methodology . . . . .	73
4.3.3	Statistical analysis . . . . .	75
<b>4.4</b>	<b>Results . . . . .</b>	<b>77</b>
<b>4.5</b>	<b>Discussion . . . . .</b>	<b>80</b>
4.5.1	Rupture risk criterion . . . . .	80
4.5.2	Regional variations of stiffness across ATAA . . . . .	85
4.5.3	Limitations . . . . .	86

---

## 4.1 Abstract

It was recently submitted that the rupture risk of an ascending thoracic aortic aneurysm (ATAA) is strongly correlated with the aortic stiffness. To validate this assumption, we propose a non-invasive inverse method to identify the patient-specific local extensional stiffness of aortic walls based on gated CT scans. Using these images, the local strain distribution is reconstructed throughout the cardiac cycle. Subsequently, obtained strains are related to tensions, through local equilibrium equations, to estimate the local extensional stiffness at every position. We apply the approach on 11 patients who underwent a gated CT scan before surgical ATAA repair and whose ATAA tissue was tested after the surgical procedure to estimate the rupture risk criterion. We find a very good correlation between the rupture risk criterion and the local extensional stiffness. Finally it is shown that patients can be separated in two groups: a group of stiff and brittle ATAA with a rupture risk criterion above 0.9, and a group of relatively compliant ATAA with a rupture risk below 0.9. Although these results need to be repeated on larger cohorts to impact the clinical practice, they support the paradigm that local aortic stiffness is an important determinant of ATAA rupture risk. **keywords:** Non-invasive inverse method; Local extensional stiffness; Finite-elements; Patient-specific rupture risk criterion; stretch ratio risk criterion

## 4.2 Introduction

An ascending thoracic aortic aneurysm (ATAA) is a pathological dilatation of the ascending thoracic aorta. It often grows slowly and usually without symptoms. ATAAs are difficult to detect because it is a silent disease. Small and slow-growing ATAAs may never rupture, but large, fast-growing ATAAs may dissect or rupture, leading to the sudden death of the patient [101].

Depending on the growth rate and size of a thoracic aortic aneurysm, treatment may vary from watchful waiting to emergency surgery. Preferably, surgery for an ATAA can be planned by replacement of the enlarged aortic segment with synthetic grafts. Excluding the patients with familial genetic disorders such as Marfan syndrome, elective surgical repair of ATAA is recommended for diameter larger than 5.5 cm or for fast growing aneurysms (growth > 1 cm per year) [29, 32, 33, 47, 84]. The 5.5 cm diameter criterion is widely acknowledged as an incomplete criterion. The International Registry of Acute Aortic Dissection (IRAD) reported that among 591 type "A" aortic dissections, 59% had a diameter below 5.5 cm. Studies dedicated to AAA demonstrated that biomechanical factors could reliably complete the diameter criterion [54, 61]. Martin et al. [98] performed a predictive biomechanical analysis of ATAA tissues to assess rupture risk on a patient-specific level. They defined a new rupture risk criterion (the diameter ratio risk) as the ratio between the current diameter of the aneurysm and the rupture diameter. They showed that the diameter ratio risk increases significantly with the physiological elastic modulus of the artery [98]. Moreover, there is a large interindividual variability of ultimate stress between individuals, which prevents obtaining patient-specific values. Different authors

measured geometrical and mechanical properties of ATAA and showed that rupture properties may vary significantly even with tissues having similar elastic properties [30,43,44,128,146]. Our research group proposed a similar rupture risk criterion, namely the stretch ratio risk, defined as the current tissue stretch (under *in vivo* conditions) and the maximum stretch (at which the tissue ruptures). We derived the stretch ratio risk criterion for a cohort of 31 patients by performing bulge inflation tests on ATAA tissues collected during surgical procedures of these patients. We also derived from these tests the tangent elastic modulus of the ATAA tissues and demonstrated that it is strongly correlated to the stretch ratio risk criterion, showing that most of the patients for whom the stretch ratio risk criterion is less than 0.9 have a modulus below 1 MPa whereas patients for whom the stretch ratio risk criterion is greater than 0.9 have a modulus ranging from 1 MPa to 7 MPa [44].

A natural question is: could the stretch ratio risk criterion be deduced from non invasive measurements of *in vivo* aortic stiffness? Trabelsi et al. [137] introduced a methodology to identify the patient-specific material properties of ATAAs by minimization of the difference between model predictions and gated CT measurements of the aneurysm. Furthermore, in an additional study, they estimated volumetric and cross sectional distensibility using preoperative dynamic CT scans and brachial pressures on a cohort of 13 patients. They also characterized the stretch ratio risk criterion and tested its correlation with the aortic stiffness obtained from distensibility measurements. However, only a moderate correlation was found. It was assumed that the lack of significance could be explained as the distensibility stiffness [138] is a global homogeneous property across the whole ATAA whereas the stretch ratio risk criterion is a local rupture property. Moreover it is well-known that the heart motion causes axial strains in the ascending thoracic aorta during cardiac cycles [151]. These axial strains of the ATAA were not taken into account in the distensibility assessment, which may be another source of possible dispersion in the results.

We recently presented a novel methodology, referred to as LESI (local extensional stiffness identification) methodology [52], to identify *local* extensional stiffness properties non-invasively, simply employing the gated CT scans and measured systolic and diastolic blood pressures. It was proved that the reconstruction of stiffness is averagely correct and the local heterogeneity can be retrieved using the LESI methodology [52].

In the present work we show that the local extensional stiffness obtained on a cohort of 11 patients using the LESI methodology correlates well with the stretch ratio risk criterion.

## 4.3 Materials and methods

### 4.3.1 The stretch ratio risk criterion

ATAA samples were collected for a cohort of 11 patients who underwent elective surgical repair of ATAA at the University Hospital of Saint-Etienne (CHU-SE) in France. Informed consent was obtained according to a protocol approved by the Institutional Review Board of the University Hospital Center of Saint-Etienne. For each sample, a  $40 \times 40$  mm square piece

was cut and a bulge inflation test was carried out. The bulge inflation test was extensively described in previous publications [38, 39, 44].

During the bulge inflation test, the circumferential,  $\tau_1$ , and axial,  $\tau_2$ , components of tension (Cauchy stress $\times$ thickness), and the circumferential,  $\lambda_1$ , and axial,  $\lambda_2$ , components of Cauchy-Green stretch were measured at the center of the sample for each pressure stage,  $p(t)$ . The stage  $t_{physio}$  at which  $\tau_1$  equals the average *in vivo* circumferential stress (according to Laplace's law) was determined according to

$$\tau_1^{t_{physio}} = \frac{P_{av}D}{4} \quad (4.1)$$

where  $P_{av}$  is the average physiological pressure (mean between diastolic and systolic pressure measured by sphygmomanometry for each patient) and  $D$  is the diameter of the aneurysm measured from the CT scan. We also denote  $\lambda_1^{t_{physio}}$  and  $\lambda_2^{t_{physio}}$  the circumferential and axial stretches respectively, both measured during the bulge inflation tests at  $t_{physio}$ .

Afterwards, the tangent elastic modulus at stage  $t_{physio}$ , denoted  $E_{in-vitro}$ , was derived as:

$$E_{in-vitro} = \lambda_1^{t_{physio}} \frac{d\tau_1^{t_{physio}}}{d\lambda_1^{t_{physio}}} \quad (4.2)$$

At the last stage of the bulge inflation test, when the ATAA sample burst, the rupture stretch and stress, measured in the direction perpendicular to the crack splitting the sample in two halves, were respectively denoted  $\lambda_{rup}$  and  $\sigma_{rup}$ .

Finally the stretch ratio risk criterion was defined as:

$$\gamma_{stretch} = \sqrt{\left(\frac{\lambda_1^{t_{physio}}}{\lambda_{rup}}\right)^2 \cos^2 \theta + \left(\frac{\lambda_2^{t_{physio}}}{\lambda_{rup}}\right)^2 \sin^2 \theta} \quad (4.3)$$

where  $\theta$  is the angle between  $e_\theta$  and  $e_2$  as shown in Fig. 2 of Duprey et al. [44].  $\gamma_{stretch}$  takes a value between 0 and 1.

The clinical and biomechanical parameters of the 11 patients are reported in Table 4.1.

Table 4.1: Clinical (sex, age and pressure difference) and biomechanical (stretch ratio risk criterion, rupture stress, *in-vivo* stiffness [138] and *in-vitro* stiffness [44]) parameters of the 11 patients.

Patient ID	Sex	Age	Valve phenotype	$\Delta P$ [kPa]	$\gamma_{stretch}$	$\sigma_{rup}$ [MPa] [44]	$E_{in-vivo}$ [MPa.mm] [138]	$E_{in-vitro}$ [MPa.mm] [44]
1	M	58	BAV	8.66	0.87	0.79	7.199	1.216
2	M	78	TAV	5.34	0.92	1.12	2.723	2.202
3	M	61	BAV	11.5	0.88	1.11	5.436	0.922
4	M	69	TAV	5.34	0.84	0.50	1.669	0.866
5	M	70	BAV	5.8	0.95	0.90	2.689	3.996
6	M	81	TAV	5.34	0.84	0.65	2.967	1.237
7	M	84	TAV	13.4	0.94	1.24	8.189	3.314
8	M	27	BAV (Marfan)	8.66	0.81	4.84	2.062	0.569
9	M	77	TAV	10.33	0.94	0.78	-	-
10	F	78	TAV	5.34	0.95	1.31	10.089	4.124
11	M	57	BAV	5.34	0.89	0.98	3.999	1.271

### 4.3.2 The LESI methodology

#### 4.3.2.1 Data acquisition

Gated CT scans were obtained for the 11 patients prior to ATAA surgical repair. Ten phases were acquired throughout the cardiac cycle for each patient and they were employed to reconstruct and track the geometrical variations of the whole aorta. Semi-automatic segmentation of the CT scans was achieved using MIMICS (v.10.01, Materialise NV). The obtained three-dimensional (3D) surface of the aorta was exported for each phase in STL format. The Vascular Modeling Toolkit (VMTK, Orobix, Bergamo, Italy; [www.vmtk.org](http://www.vmtk.org)) [11] was used to generate a structural mesh of the exported geometries. In order to run VMTK and to obtain the parametric coordinates of the surface, aortic surfaces were cut at all phases by the same cross sectional planes to determine a larger domain than the final segment of interest. An identical smoothing factor was applied at all phases. To identify the systolic and diastolic phases, the luminal volumes of all phases were compared. The systolic phase was defined as the largest volume and the diastolic phase as the smallest volume. The variation of cross sectional area between diastole and systole was used to derive the arterial distensibility and to deduce the extensional stiffness property based on in-vivo distensibility, denoted  $E_{in-vivo}$ . Results are reported in Table 4.1 and were derived from a previous analysis [138].

#### 4.3.2.2 Foundation of the LESI methodology

Each reconstructed aortic geometry was meshed in such a way that each node represented the position of the same material point at each phase of the cardiac cycle. Thus, a structural mesh is required, with an identical number of elements and nodes at all phases. Therefore, a mesh morphing function between the geometries of each phase was reconstructed and applied. VMTK was used to generate the structural mesh from segmented geometries (STL files). VMTK is based on the calculation of centerlines and decomposition of the surface into existing branches and mapping each branch onto template parametric cylindrical coordinates. VMTK generates consistent parameterizations over a wide range of bifurcating geometries. The procedure to obtain parametric coordinates by VMTK, is explained in detail in Farzaneh et al. [52]. In order to track the same material points at all phases throughout the cardiac cycle, we assumed anatomical references, namely the left subclavian artery, the brachiocephalic artery, the left common carotid artery and the coronary artery branches. Eventually, the obtained data from VMTK were postprocessed in Matlab to extract an accurate mesh using the longitudinal and circumferential metrics. Moreover, twisting occurring during aortic wall motions [151] was also corrected by deriving the time variations of the circumferential coordinate of coronary arteries in the space of parametric coordinates obtained from VMTK and subtracting this value from the circumferential coordinate of the assumed reference phase [52].

Any periodic function (such as material coordinates in each phase of a cardiac cycle,  $x(t)$ ) can be expressed as a summation of sine and cosine functions of varying frequency. Therefore,

using the structural mesh of all ten phases, a discrete Fourier transform was employed such as

$$x(t) = a_0 + \sum_{n=1}^{\infty} \left( a_n \cos(nft) + b_n \sin(nft) \right) \quad (4.4)$$

where  $a_0$  is the Direct current (DC) term (average) and  $f$  is the fundamental frequency.

Strains in longitudinal and circumferential directions were obtained on the average geometry (defined by using DC terms of all nodal positions) by applying displacements and torsion at each node corresponding to the fundamental term obtained from the Fourier transform in Eq. 4.4. As the fundamental term is complex, the real and the imaginary parts are applied separately at the corresponding nodes on the average geometry using the finite element method (FEM). Eventually the reconstructed strain components were also complex [52]. Therefore the magnitude of strains in the longitudinal and circumferential directions could be obtained [52] such as

$$\begin{aligned} \varepsilon_1 &= (\varepsilon_1^r{}^2 + \varepsilon_1^{im}{}^2)^{1/2} \\ \varepsilon_2 &= (\varepsilon_2^r{}^2 + \varepsilon_2^{im}{}^2)^{1/2} \end{aligned} \quad (4.5)$$

where superscripts "*r*" and "*im*" indicate real and imaginary contributions, respectively. It is well-known that the aortic tissue is globally anisotropic and nonlinear, but here its mechanical behaviour was linearized in the physiological range of strains between diastole and systole, and anisotropic effects was neglected in this range. The constitutive equations reduced to Hooke's law and the plane stress assumption was considered [80]. The membrane tensions,  $\tau$ , were written such as

$$\begin{aligned} \tau_1(t) &= \tau_1^0 + Q(\varepsilon_1(t) + \nu\varepsilon_2(t)) \\ \tau_2(t) &= \tau_2^0 + Q(\nu\varepsilon_1(t) + \varepsilon_2(t)) \end{aligned} \quad (4.6)$$

where  $Q$  is the extensional stiffness and  $\nu$  is the Poisson's ratio.  $\tau_1^0$  and  $\tau_2^0$  are the components, in the local coordinate system (1 is for local circumferential direction and 2 is for local axial direction), of the membrane stresses (tensions) resulting from the average pressure applied onto the average aortic geometry. A FE stress analysis was implemented to derive  $\tau_1^0$  and  $\tau_2^0$  by applying the average pressure  $P_0$  on the average geometry using the approach proposed by Joldes et al. [85].

It was assumed that each element of the arterial wall is a finite sector of an ellipsoidal membrane with radii  $r_1$  and  $r_2$  in both circumferential and longitudinal directions, respectively. So, in the framework of these assumptions, local equilibrium equations were written as

$$P(t) = \frac{\tau_1(t)}{r_1(t)} + \frac{\tau_2(t)}{r_2(t)} \quad (4.7)$$

where  $P(t)$  is the applied pressure. Thus linking Eqs. 4.6 with 4.7, we obtained the extensional stiffness as

$$Q = \frac{\Delta P + \frac{\tau_1^0 \Delta r_1}{(r_1^0)^2} + \frac{\tau_2^0 \Delta r_2}{(r_2^0)^2}}{\frac{\varepsilon_1(t) + \nu\varepsilon_2(t)}{r_1^0} + \frac{\nu\varepsilon_1(t) + \varepsilon_2(t)}{r_2^0}} \quad (4.8)$$

where  $\Delta P = (P_{sys} - P_{dias})/2$ .



To obtain  $r_1$  and  $r_2$ , we developed a method based on the principle of virtual work as introduced by Bersi et al. [19] and Farzaneh et al. [52].

#### 4.3.2.3 Numerical implementation of the LESI methodology

For each aorta, the Abaqus FE software [72] was employed to derive strains from the nodal displacements obtained with the Fourier transform. For each FE analysis, an orientation user subroutine (ORIENT) was employed to assign local material directions and to record the results in the local coordinate system. Each geometry was a non-perfectly cylindrical geometry so that the radial direction (normal to the artery) was defined as the outward normal direction to each element, the axial direction was defined as the direction parallel to the luminal centerline in the direction of the blood flow, and the circumferential direction was perpendicular to both previously defined directions. To calculate and visualize the local extensional stiffness obtained from Eq. 4.8, a user material subroutine (UMAT) and a user-defined external databases (UEXTERNALDB) were coupled with Abaqus [72].

In summary, as shown in Fig. 4.1, we have four types of FE analyses to be performed in our methodology:

1. Strain calculation: this was a displacement driven finite element analysis. Displacements derived from CT images were applied to each node of the mesh in the reference geometry.
2. Radii of curvature calculation: this was again a displacement driven finite element analysis. A displacement normal to the luminal surface was applied at each node. The resulting strain fields equaled the local curvature fields, which permitted a direct evaluation of the local radii of curvature.
3. Calculation of average tensions: using the average geometry, an average pressure was applied on the lumen. In the inlet and outlet nodes, we assigned displacements assessed using the dynamic CT images.
4. Validation study: the difference between systolic and diastolic pressures (pulse pressure) was applied on the inner luminal surface. Nodal displacements of inlets and outlets were zeroed.

#### 4.3.2.4 Numerical validation of the LESI methodology

Two different material behaviors were considered to perform numerical validations: linear isotropic elasticity and non-linear anisotropic hyperelasticity. The reconstructed stiffness was in good agreement with the reference, especially local heterogeneities could be well retrieved [52].

#### 4.3.3 Statistical analysis

Three regions were defined in the ascending thoracic aorta of each patient:

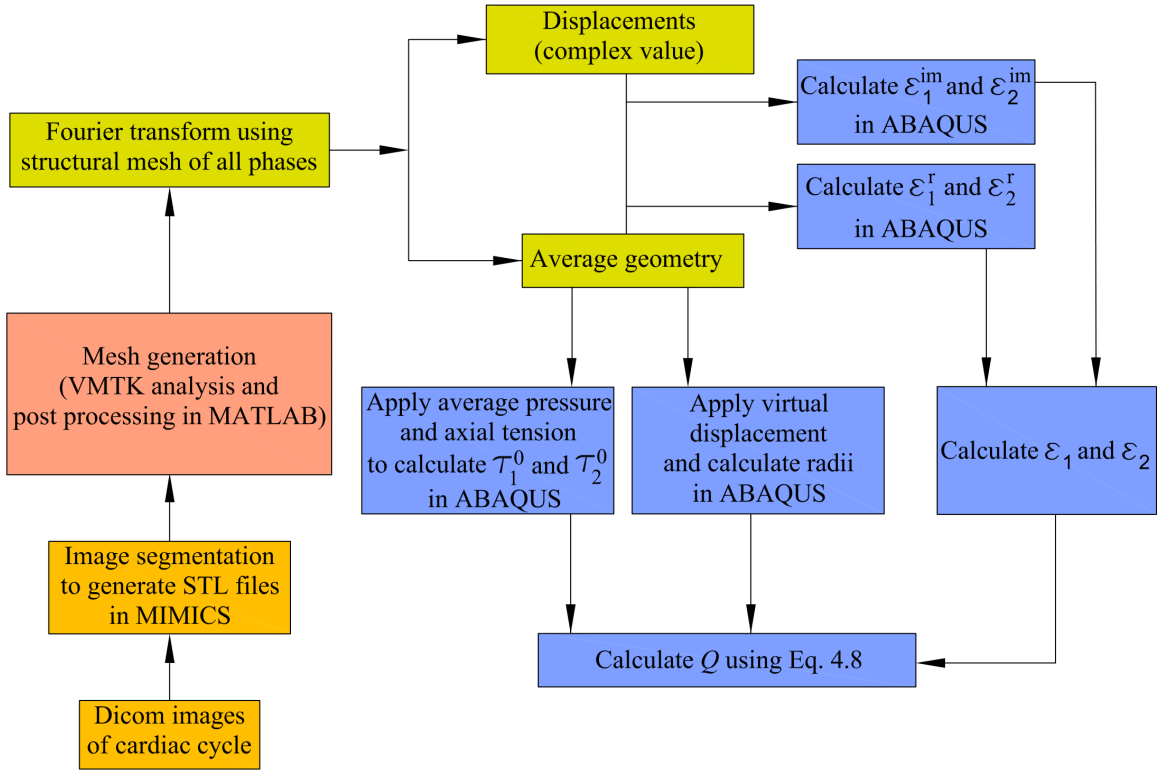


Figure 4.1: Flowchart of the LESI methodology for local extensional stiffness identification.

1. ATAA region 1 is the whole ascending thoracic aorta.
2. ATAA region 2 is the segment of ascending thoracic aorta which was removed during the surgical procedure.
3. ATAA region 3 is the square sample of  $40 \times 40$  mm which was cut for the bulge inflation test.

As the tests of normality show that the data is non-normal, for the sake of statistical analysis, we derived the median value of the identified extensional stiffness of all elements across each of the 3 ATAA regions defined above, denoted respectively  $Q_1$ ,  $Q_2$  and  $Q_3$ . We also derived the value of the identified extensional stiffness at the center of ATAA region 3, denoted  $Q_4$ . The derived median values are very close to mean values.

Patients were divided in two groups based on their  $\gamma_{stretch}$  value, as this appears to be the relevant criterion to estimate the risk of rupture [44]. Then,  $Q_1$ ,  $Q_2$ ,  $Q_3$  and  $Q_4$  for each group were analyzed as median and the 25th and 75th percentiles using boxplots. Statistical pairwise comparisons were made across the 2 groups for each of the 4 material parameters. The P-value was derived for each quantity. Significant differences (denoted by \*) in Fig. 4.5 were identified for comparisons with  $p < 0.05$ .

We also searched for correlations between stiffness values identified *in vivo* ( $Q_1$ ,  $Q_2$ ,  $Q_3$  and  $Q_4$ ) and the properties characterized *in vitro*, including  $\sigma_{rup}$ ,  $E_{in-vitro}$  and  $\gamma_{stretch}$ . These

Table 4.2: Median values of extensional stiffness identified in the different ATAA regions.  $Q_1$ ,  $Q_2$ ,  $Q_3$  and  $Q_4$  are the extensional stiffness of the whole ascending thoracic aorta, the segment of ascending thoracic aorta which was removed during the surgical procedure, the square sample of  $40 \times 40$  mm which was cut for the bulge inflation test and the center of this square (center of the outer curvature part of the ascending thoracic aorta) respectively.

Patient ID	$Q_1$ [MPa.mm]	$Q_2$ [MPa.mm]	$Q_3$ [MPa.mm]	$Q_4$ [MPa.mm]
1	7.48	8.3	8.7	10.7
2	5	5.1	4.9	5
3	5.35	5.6	5.2	5.5
4	2.39	3.3	3.2	2.9
5	5.6	6.6	6.3	7.6
6	3.2	3.7	3.4	3.5
7	5.41	5.69	7.59	8
8	1.68	2.15	2.11	1.41
9	5.5	5.6	5.3	5.3
10	4.11	5.04	4.6	6.17
11	3.4	4.8	3.6	4

correlations are shown in Fig. 4.2 by curve fitting with regression. The Pearson product-moment correlation coefficient was also derived to assess the dependence between each couple of quantities.

## 4.4 Results

The median values of extensional stiffness ( $Q_1$ ,  $Q_2$ ,  $Q_3$  and  $Q_4$ ) are reported in Table 4.2. We report the Pearson product-moment correlation coefficient,  $\rho$ , between stiffness properties identified *in vivo* ( $Q_1$ ,  $Q_2$ ,  $Q_3$  and  $Q_4$ ) and the properties characterized *in vitro*, including  $\sigma_{rup}$ ,  $E_{in-vitro}$  and  $\gamma_{stretch}$  in Table 4.3. We found a good correlation between  $Q_4$  and  $\gamma_{stretch}$  ( $\rho=0.89$ ). Other extensional stiffness properties identified *in vivo* also show some correlation with  $\gamma_{stretch}$ , but the best correlation was found for  $Q_4$ , which is the identified stiffness at the center of ATAA region 3. Note that no correlation was found between  $\sigma_{rup}$  and the identified stiffness properties.

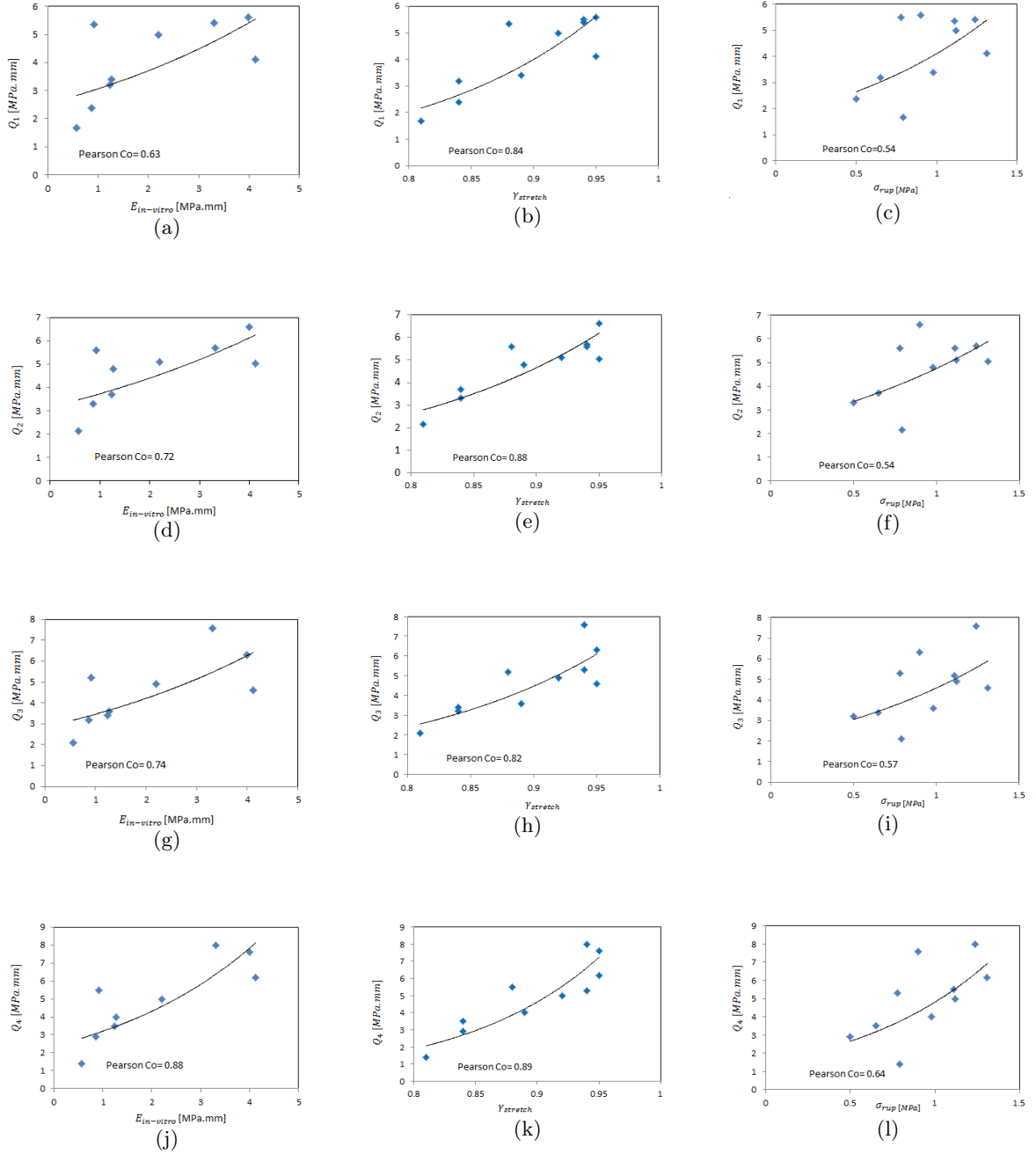


Figure 4.2: Regression of  $Q_1$ ,  $Q_2$ ,  $Q_3$ , and  $Q_4$  versus stretch ratio risk criterion, rupture stress and *in – vitro* stiffness [44] of patients.

Table 4.3: Pearson product-moment coefficient value,  $\rho$ , between stiffness of different ATAA regions and in-vitro parameters.

	$\gamma_{stretch}$	$E_{in-vitro}$ [MPa.mm]	$\sigma_{rup}$ [MPa]	$Q_1$ [MPa.mm]	$Q_2$ [MPa.mm]	$Q_3$ [MPa.mm]	$Q_4$ [MPa.mm]
$\gamma_{stretch}$	1	0.92	0.64	0.84	0.88	0.82	0.89
$E_{in-vitro}$ [MPa.mm]	0.92	1	0.62	0.63	0.72	0.74	0.88
$\sigma_{rup}$ [MPa]	0.64	0.62	1	0.54	0.54	0.57	0.64
$Q_1$ [MPa.mm]	0.84	0.63	0.54	1	0.95	0.9	0.88
$Q_2$ [MPa.mm]	0.88	0.72	0.54	0.95	1	0.87	0.91
$Q_3$ [MPa.mm]	0.82	0.74	0.57	0.90	0.87	1	0.95
$Q_4$ [MPa.mm]	0.89	0.88	0.64	0.88	0.91	0.95	1

Patients were divided in two groups based on their stretch ratio risk index [44]:

- group 1 composed of 5 patients with a large stretch ratio risk index:  $\gamma_{stretch} > 0.9$ .
- group 2 composed of 6 patients with a relatively small stretch ratio risk index:  $\gamma_{stretch} < 0.9$ .

The stress–stretch curves of their ATAA sample derived from the bulge inflation test are shown in Fig. 4.3. Solid lines indicate the state of stress and stretch undergone by the aortic tissue *in vivo*. The same maximum stress is always reached in the circumferential and axial directions of the tissue as the bulge inflation test induces a state of nearly equibiaxial tension. However, anisotropy manifests more evidently for some patients in the maximum stretches, 6/11 patients having a larger circumferential stretch and 5/11 a larger axial stretch. In Fig. 4.4, we show the reconstructed geometry for all patients. Remarkably, Fig. 4.4-h is a patient with Marfan syndrome and in Fig. 4.4-d the patient had a bovine arch which is a rare malformation often related to ATAA. In Fig. 4.5, we show the boxplots of median extensional stiffness values for both groups of patients. A boxplot is shown for each stiffness value ( $Q_1$ ,  $Q_2$ ,  $Q_3$  and  $Q_4$ ). A significant difference between both groups is shown for the  $Q_4$  value with a p-value of 0.027. The identified stiffness distribution obtained with the LESI methodology is shown for each patient in regions 1, 2 and 3 (Fig. 4.6).

## 4.5 Discussion

In this study the LESI methodology [52] was employed to reconstruct noninvasively the stiffness distribution of the ascending thoracic aorta of 11 patients based on their preoperative gated CT scans. For each patient, the stretch ratio risk criterion was also characterized postoperatively using the bulge inflation test [44]. A very good correlation was found between the extensional stiffness and the stretch ratio risk index. Finally it was shown that patients can be separated in two groups: a group of stiff and brittle ATAA with a rupture risk criterion above 0.9, and a group of relatively compliant ATAA with a rupture risk below 0.9. This shows that the *in vivo* arterial stiffness could be used to derive the stretch ratio risk index. The cut–off value of 0.9 was proposed in a previous paper [44] in which we had tested ATAA samples coming from over 30 patients. The statistical analysis nicely showed that the group of ATAA with rupture risk below 0.9 and the group with rupture risk above 0.9 were two different groups. In the current paper, only 11 patients are analyzed as only these 11 patients had both a gated CT scan and a bulge inflation test.

Here we used gated CT to reconstruct the local aortic stiffness. Other imaging modalities may be possible such as ultrasounds [143, 151] or magnetic resonance imaging [12].

### 4.5.1 Rupture risk criterion

Multiple studies have been developed to define a reliable rupture risk criterion for ATAA [44, 98, 128] and AAA [145]. For instance, Martin et al. [98] defined a criterion, named the

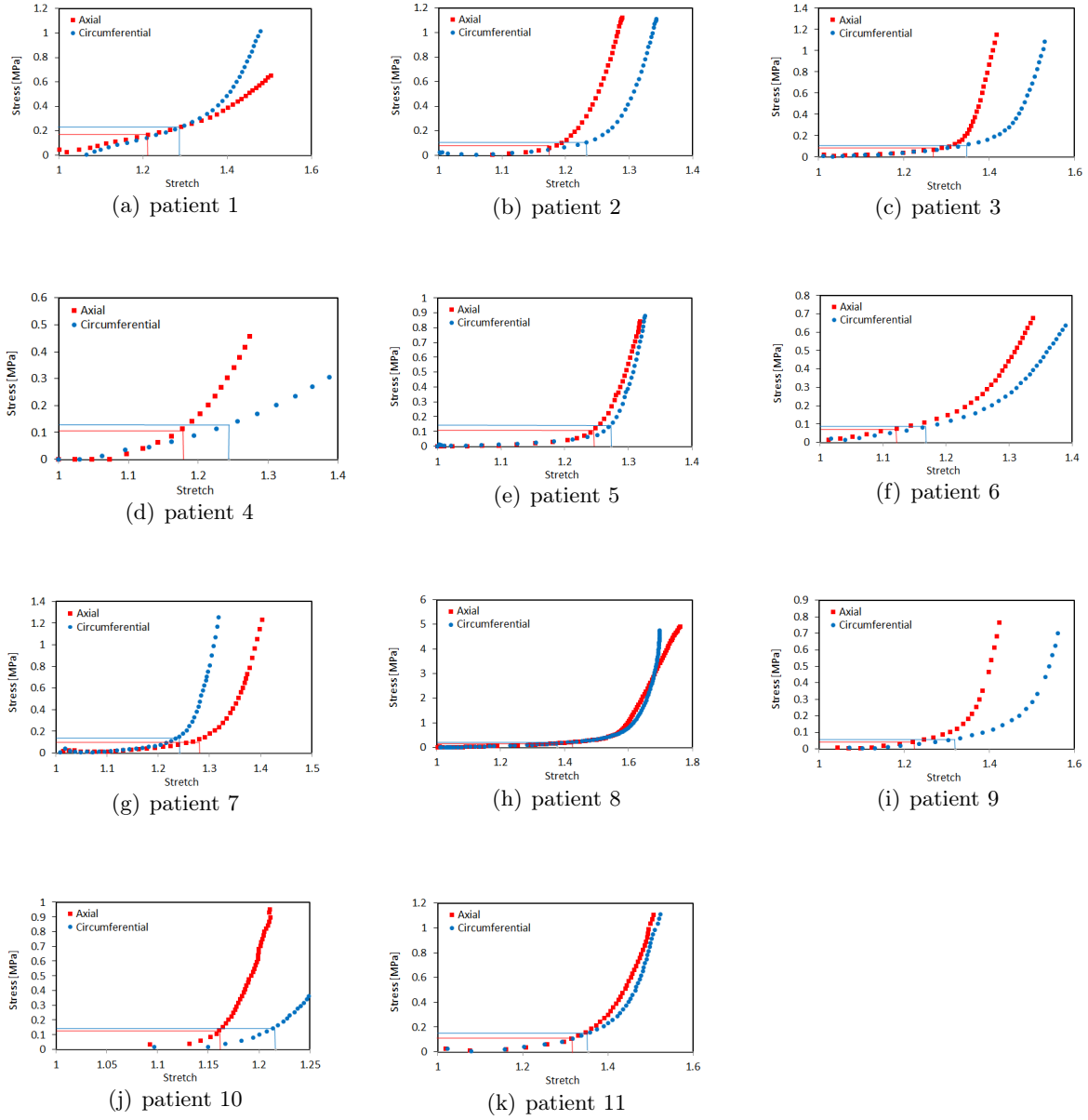


Figure 4.3: Stress–stretch curves obtained from the bulge inflation test for all patients. Solid lines show the in–vivo stretch and stress points [44, 138].

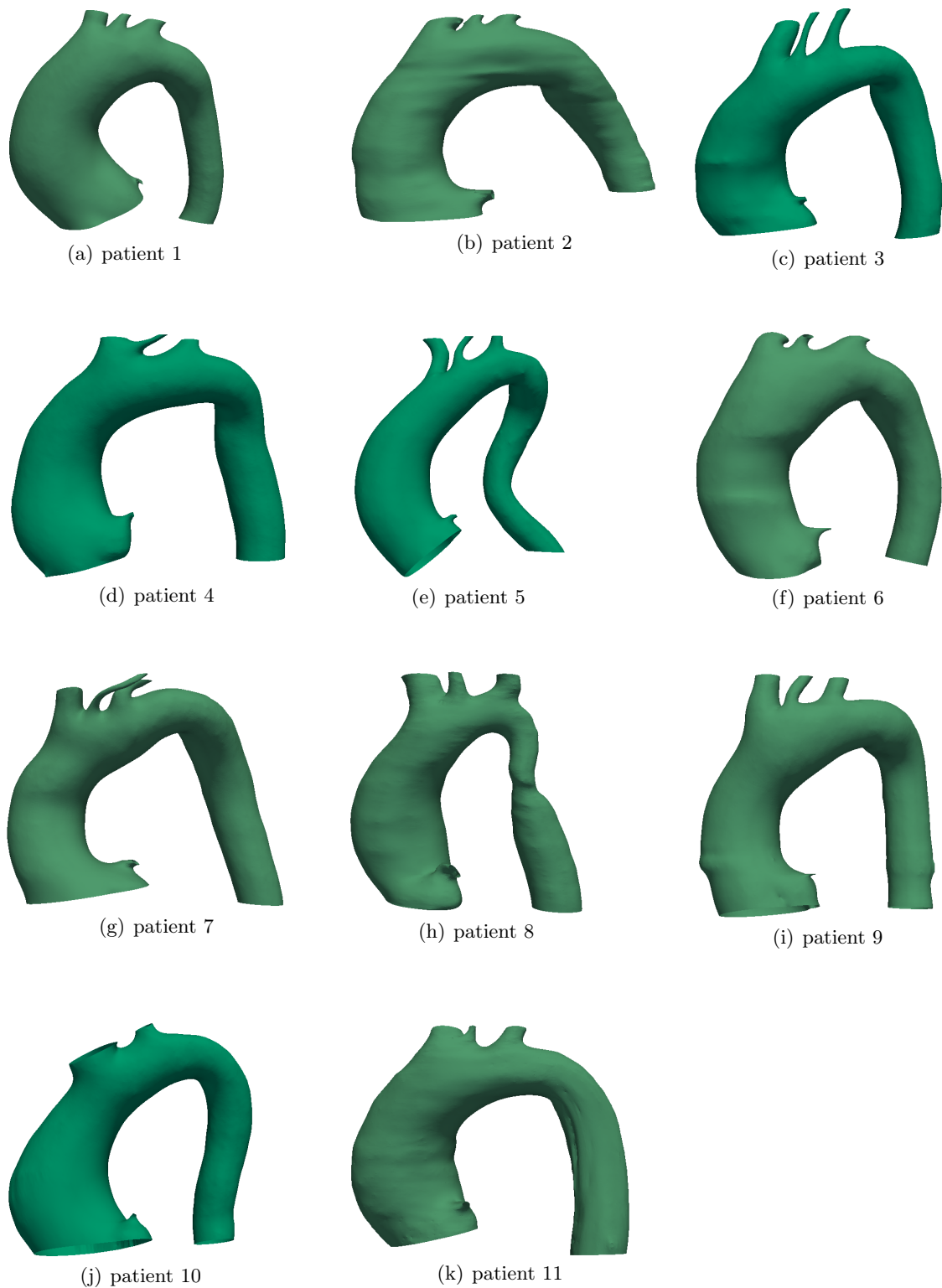


Figure 4.4: Segmented geometries of aorta for diastole using CT images for 11 patients.



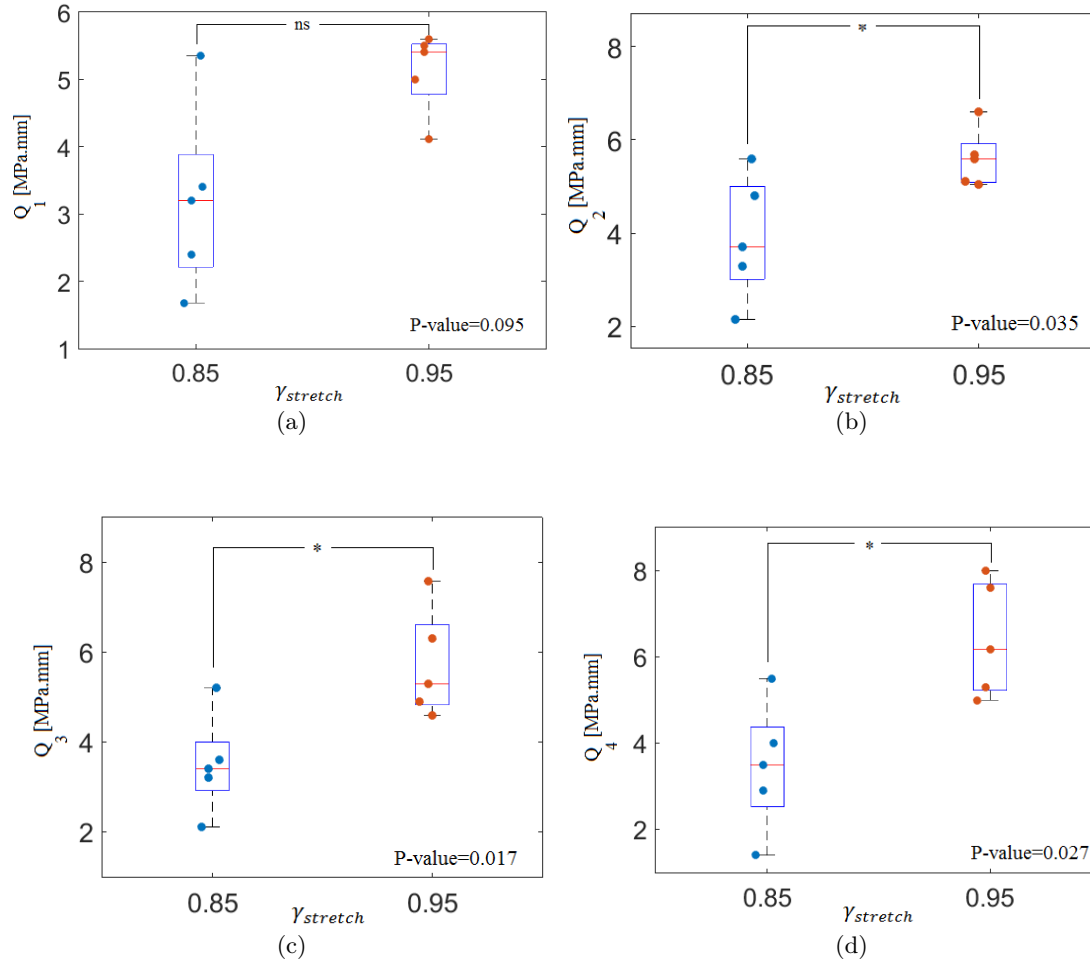


Figure 4.5: Boxplots of both groups of patients a-  $Q_1$  (median value across ATAA region 1), b-  $Q_2$  (median value across ATAA region 2), c-  $Q_3$  (median value across ATAA region 3) and d-  $Q_4$  (value at center of ATAA).

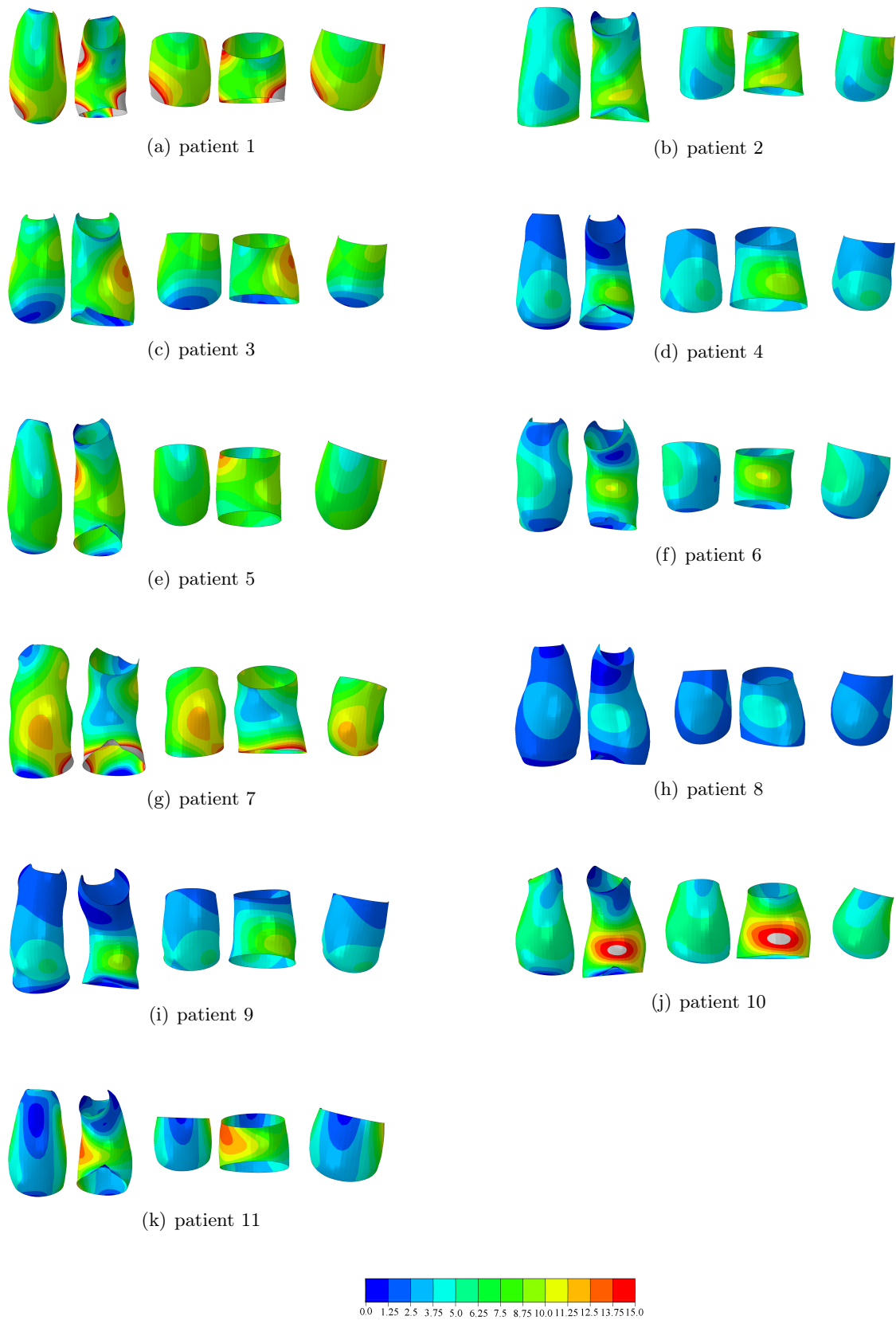


Figure 4.6: Extensional stiffness distribution [MPa.mm] obtained with the LESI methodology across the ascending thoracic aorta of ten patients. From left to right, region 1 (frontal and distal views), region 2 (frontal and distal views) and region 3.

diameter ratio risk, which is the ratio between the current diameter of the aneurysm and the rupture diameter. They showed that the diameter risk increases significantly with the physiological elastic modulus of the artery. Commonly, rupture risk is also estimated as the ratio between current (or physiological) and ultimate stress. However, wall stress estimation suffers from uncertainties in wall thickness measurement. Moreover, there is a large interindividual variability of ultimate stress between individuals, which prevents obtaining patient-specific values. Different authors measured geometrical and mechanical properties of ATAA and showed that rupture properties may vary significantly even with tissues having similar elastic properties [30,43,44,128,146]. Moreover, another disadvantage of stress based rupture index is that current stress induced by normal blood pressures is usually far from the ultimate stress. Indeed, rupture is often an accidental event during which there is a sudden rise of pressure and stress in the wall. There is evidence showing that dissections are preceded by a specific severe exertional or emotional event [47]. The stretch ratio risk index [44], defined as the current tissue stretch (under in vivo conditions) and the maximum stretch (at which the tissue ruptures), appears very promising as it is strongly correlated with the local tissue stiffness which can be obtained with the LESI methodology. Conversely our results showed that there is no correlation between the strength of ATAA samples and their in vivo stiffness.

In addition, to examine various criteria of the local failure of AAA, Volokh et al. [145] developed an experimental model including a failure description. They analyzed various states of the biaxial tension of the AAA material and evaluated the strain energy, the maximum principal stretch and stress, the maximum shear stress and von Mises stress criteria of the local failure. They concluded that the von Mises stress showed a larger variability compared to the strain energy. It could be interesting to define rupture risk criterion based on maximum stored strain energy as it would combine both stress and strain contributions, but apart from Volokh et al., nobody really investigated this way further.

#### 4.5.2 Regional variations of stiffness across ATAA

A major conclusion of the current study is that it is important to identify local stiffness properties and not a global stiffness property based on distensibility analysis for instance [138], as rupture is a local phenomenon. Over the past decades the biomechanical properties of the aorta have been widely investigated [43,44,128,138,146], but the material properties were usually characterized globally and homogeneously across ATAA. A few studies considered regional variations of material properties across ATAA. Iliopoulos et al [82] stated that circumferential specimens were stiffer than longitudinal ones in the posterior and left lateral. Furthermore they found no significant regional variations of aortic stiffness in the circumferential direction. Ferrara et al. [53] supported these results and investigated mechanical properties of human ascending aortas for a cohort of patients taking into account regional, directional, aging and gender variations. They showed that regardless of age and gender, the mean elastic modulus was larger in the circumferential direction. Moreover, aging reduced the mean elastic modulus and male had higher mean elastic modulus comparing to female. Choudhury et al. [30]

compared stiffness and material properties of ATAA at different angular positions and showed that the outer and the inner curvatures are the stiffest and most elastic quadrants respectively. Recently, digital image correlation (DIC) was used to investigate the local material properties of excised aortic samples [13,38,39]. Inverse methods were developed to process DIC measurements and reconstruct the regional variations of material properties.

Regional variations of material properties are attributed to remodeling of the arterial wall due to damage of elastic fibers. A typical wall histopathology, involving ECM breakdown (with disrupted elastin networks), vSMC loss co-localized with areas of mucoid degeneration, is common to ATAA whatever their aetiologies [101]. When elastin networks are disrupted, a larger fraction of collagen fibers need to be produced to resist the wall stress [142]. This manifests with aortic stiffening and reduced extensibility (stretch based rupture risk), which are the two markers for which we found correlations in our study. Sassani et al [124] demonstrated a large distribution of fiber orientations spanning from circumferential to longitudinal directions, which was also supported by Sokolis et al. [131] showing that ATAA had no effect on the tissue strength. However, this can cause stiffening and extensibility reduction, confirmed by histological observations of elastin degradation and increase of collagen mass fractions. It could be interesting also to check the possible correlation of these regions with local concentration of wall shear stress induced by the blood flow [34,97].

### 4.5.3 Limitations

Several limitations in this work can be discussed.

- The residual stresses existing in the ATAA wall were neglected in this work. More specifically, we report that a major limitation of our study is that we do not consider layer specific material and rupture properties of ATAA. As shown by Sokolis et al. [130] residual stretches may vary strongly from one layer to another, and depend also on circumferential positions. It was also shown that failure stretches correlate positively with residual stretches [41]. Therefore, layer-specific properties are important aspects that should be integrated in the future to rupture risk estimation of ATAAs. In addition, it was assumed that the arterial wall behaves as an isotropic and linearly elastic material within the systolic–diastolic range. Therefore, the isotropy assumption here delivers a combination of the axial and circumferential extensional stiffnesses, which may be different. However, if there was a significant difference between the axial and circumferential extensional stiffnesses, the extensional stiffness identified here would be closer to the circumferential one, as shown in chapter 3. Involving the local curvatures in Eq. 4.8 puts most of the weight on circumferential effects, as the axial radius of curvature is significantly higher than the circumferential one.
- The LESI approach stands on local equilibrium equations obtained based on the principle of virtual work, similar to the ones derived by Bersi et al. [19]. Therefore, equivalent to the generalized Laplace’s law, it considers the local equilibrium between pressures and

tensions in a membrane, meaning that the aortic wall experience no shear through the thickness. This may not be a realistic assumption in the regions near the branches which were excluded in this analysis.

- Eq. 4.8 involves average tensions existing in the aorta due to the action of the average blood pressure and geometrical nonlinearity associated with finite deformations [18]. These tensions were approximated using the approach of Joldes et al. [85]. This approach consists in achieving a linear elastic stress analysis on the same structure as the aorta, assigning a very large elastic modulus. The approach is valid for membrane structures. The membrane assumption was previously shown to be a good approximation for elastostatics of aortic aneurysms [96].
- A final limitation is that  $\gamma_{stretch}$  evaluates the ex vivo rupture risk, not the in vivo one (for instance, the role of vSMC tone or surrounding tissues may be important in vivo).



---

## Chapter 5

# Extension of the methodology to MRI and ultrasound imaging

### Résumé

La méthodologie d'identification de la rigidité membranaire locale (LESI en anglais) a été récemment développée dans notre groupe pour identifier la rigidité membranaire locale de manière non invasive, à l'aide de tomodensitométries (TDM) et de pressions brachiales contrôlées pour évaluer le risque de rupture des anévrismes de l'aorte thoracique ascendante (ATAA) chez 11 patients. L'ATAA est un gonflement localisé dans l'aorte asymptomatique et généralement diagnostiqué lors de la recherche d'autres maladies. Il est important d'étudier la possibilité de remplacer le scanner par d'autres méthodes en raison de sa forte dose de rayonnement. Dans ce chapitre, l'objectif principal est d'appliquer la méthodologie LESI à deux autres modalités d'imagerie moins invasives: l'échographie et l'IRM. Plus spécifiquement, nous appliquons la méthodologie LESI aux données l'échographie obtenues sur un patient réel avec un ATAA et aux données IRM sur un volontaire. Les deux applications sont d'abord des études de preuve de concept et montrent la faisabilité de la méthode LESI pour les deux modalités d'imagerie. Les travaux futurs porteront également sur les applications multimodales.

## Contents

---

<b>5.1</b>	<b>Abstract . . . . .</b>	<b>91</b>
<b>5.2</b>	<b>Introduction . . . . .</b>	<b>91</b>
<b>5.3</b>	<b>Material and methods . . . . .</b>	<b>92</b>
5.3.1	Ultrasound (US) . . . . .	92
5.3.2	Iterative Finite Element Analysis . . . . .	94
5.3.3	MRI . . . . .	95
5.3.4	Theory of the LESI methodology . . . . .	95
<b>5.4</b>	<b>Results . . . . .</b>	<b>96</b>
5.4.1	US . . . . .	96
5.4.2	MRI . . . . .	96
<b>5.5</b>	<b>Discussion . . . . .</b>	<b>97</b>
<b>5.6</b>	<b>Future work . . . . .</b>	<b>98</b>

---



## 5.1 Abstract

The local extensional stiffness identification (LESI) methodology was developed recently in our group to identify local extensional stiffness non-invasively, using gated computed tomography (CT) scans and brachial pressures to assess the risk of rupture of ascending thoracic aortic aneurysms (ATAAs) for 11 patients. ATAA is a localized bulge in the aorta which is asymptomatic and generally diagnosed under investigation of other diseases. It is important to investigate the possibility of substituting CT scans by other modalities because of its high radiation dose. In this chapter the main objective is to apply the LESI methodology to 2 other less-invasive image modalities: ultrasound (US) imaging and MRI. More specifically, we apply the LESI methodology to US data obtained on a real ATAA patient and to MRI data on a volunteer. Both applications are first proof of concept studies and show the feasibility of the LESI method for both imaging modalities. Future work will also focus on multimodality applications.

## 5.2 Introduction

An aortic aneurysm is a dilation of the aorta. It is asymptomatic and is accidentally diagnosed under investigation of other disease. The current criterion for surgeons to decide about any treatment or surgical intervention is diameter. Surgery is recommended when the diameter is larger than 5.5 cm or the aneurysm is diagnosed fast growing.

The LESI methodology, which was recently published [52] is able to identify local extensional stiffness non-invasively. It employs gated computed tomography (CT) scans and systolic and diastolic blood pressures of the patients suffering from ascending thoracic aortic aneurysm (ATAA) [52]. In the previous chapter we concluded that the evaluation of the local elastic properties of the ATAA wall from in vivo data that are clinically available, might be essential to estimate rupture risk of ATAA [105].

Nowadays Magnetic resonance imaging (MRI) is becoming commonplace in cardiovascular imaging. Unlike CT scans, MRI uses powerful magnetic fields to produce detailed pictures of organs and there is no Xray radiation involved. Ultrasound imaging is another interesting alternative. For example, Van Disseldorp et al. [144] employed ultrasound (US) images to develop a minimally invasive approach to characterize the incremental mechanical properties of the ATAA wall in vivo. They developed an iterative finite element method (FEM) in which the cyclic deformation was input and a patient-specific incremental shear modulus was assessed.

Based on previously published work using MRI [34] and US [144] data, it would be interesting to reconstruct local extensional stiffness by employing these acquisition techniques. Therefore, the objective of this chapter is to make the first proof of concept of the LESI method with these 2 imaging modalities. We also propose to analyze possible regional correlation between wall shear stress distributions and local extensional stiffness reconstructions as imaging modalities such as 4D flow MRI can also be used to assess blood flows simultaneously with wall deformations.

## 5.3 Material and methods

### 5.3.1 Ultrasound (US)

#### 5.3.1.1 Data acquisition and segmentation

In this study, a patient who underwent graft replacement at the Catharina Hospital in Eindhoven (CZE) was included and the ATAA mechanical properties were characterized in vivo using 4D (3D+t) transesophageal US imaging. The transesophageal US data is a part of the routine clinical workflow during cardiac surgery. US data were captured using a Philips IE33 or EPIQ US System equipped with the same transducer, an X7-2t probe designed for transesophageal echocardiography (Philips Healthcare, Eindhoven, Netherlands and PULS/e lab led by Professor Richard Lopata). Image acquisition was carried out perioperatively and before the function of the heart was taken over by the cardiopulmonary bypass (Fig. 5.1). The image acquisition process by US is explained in detail by [144]. Using an intravascular pressure needle in the ascending aorta the intramural pressure was measured during US acquisitions.

The geometry of the ATAA was needed for the identification of local extensional stiffness.

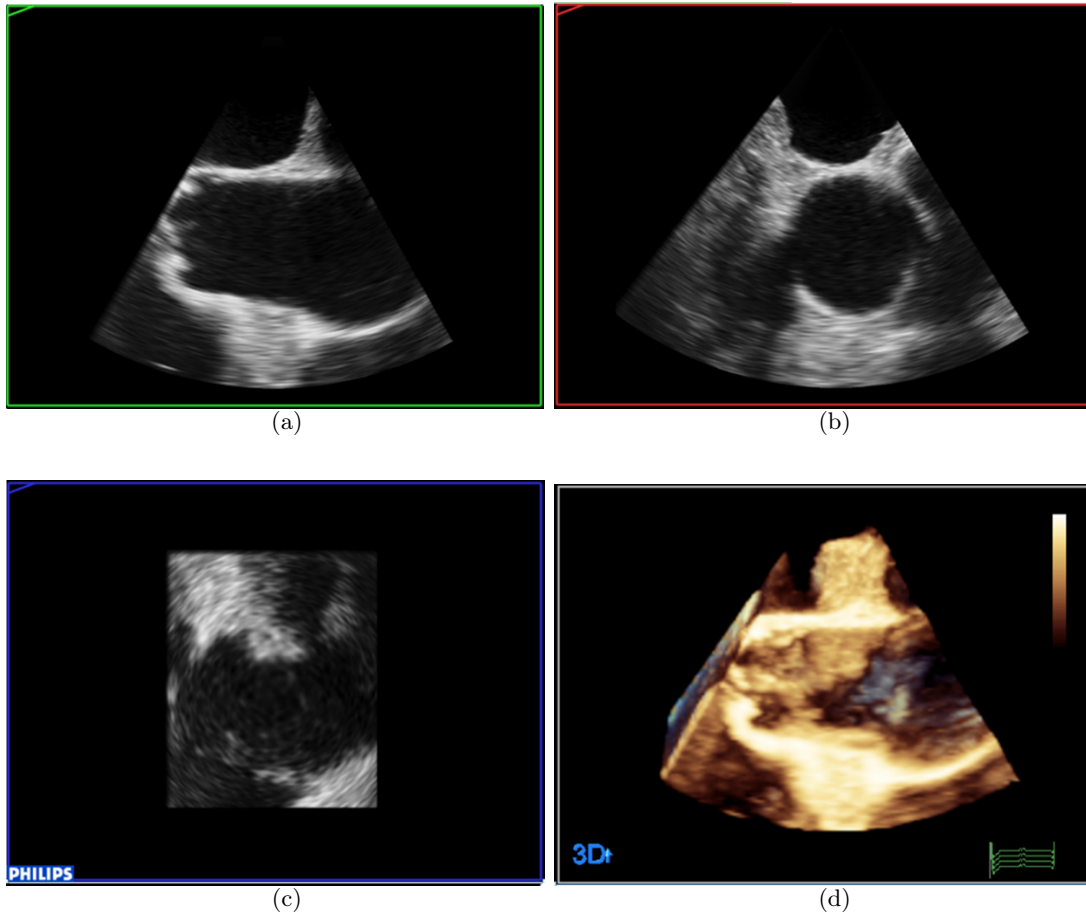


Figure 5.1: Example of a 3D transesophageal US acquisition of an ATAA. a- Sagittal, b- transversal, c- coronal and d- cross-section and a 3D volume render [144].

Aortic wall segmentation began manually and thereafter was completed automatically. As seen in Fig. 5.2-c, two points were first selected at the centerline of the aorta in the longitudinal plane. The Euclidean shortening flow (ESF) filter was used to reduce noise in the US data which could prevent the segmentation process. The segmentation was performed using active deformable models (ADMs) as introduced by [88]. The ADMs were deformed such as to be located at requested image features while minimizing an energy function. The total energy was given by

$$E = s_1 E_{in} + s_2 E_{edge} + E_{shape} \quad (5.1)$$

where  $E_{in}$  and  $E_{edge}$  are external energy terms based on the image intensity and gradients respectively,  $s_1$  and  $s_2$  are weighting parameters, and  $E_{shape}$  is the internal energy of the segmentation shape.

The external energy was estimated using a Gaussian differentiator ( $\sigma = 0.7$ ) in the radial direction. Since the derivative is taken with respect to the vessel's centerline, the inner wall of the aorta is expressed as a positive value in  $E_{edge}$ , while the outer wall is expressed as a negative value. This ensures that the shape is contained within aorta. An overview of the segmentation process is shown in Fig. 5.2. The segmentation procedure was explained in detail in [144]. All parameters are given in Table 2 of [144].

### 5.3.1.2 Cyclic deformation

In the cyclic deformation of the ATAA, a remarkable motion was observed in the longitudinal direction (parallel to the centerline or blood flow direction of the ATAA). Hence, 2D aortic expansion could not be tracked in-plane. Therefore, a multiscale registration approach was used, with the assumption that the cyclic motion and deformation of the ATAA segment within the limited field-of-view (FOV) could be approximated by an affine transformation. An affine parametrization,  $A$ , was employed in which the transformation matrix can be multiplicatively decomposed to a combination of a rotation matrix,  $R$ , shear matrix,  $G$ , scaling matrix,  $S$ , and translation matrix,  $T$  [94] as

$$A = R.G.S.T \quad (5.2)$$

The longitudinal axis was defined to be parallel to the centerline of the aorta, which was obtained by manually rotating the B-mode data until the centerline was parallel to the y-axis. A region of interest closely surrounding the ATAA was chosen by expanding the segmentation results in radial direction.

Registration was performed using the open source registration toolbox Elastix (Image Science Institute, UMC Utrecht, Utrecht, the Netherlands) in a two-step multi-resolution strategy, in which the longitudinal and circumferential stretch were estimated separately. In the first step, a larger region of interest (ROI) was used, including the heart, to estimate the longitudinal motion and stretch accurately. In the second step, the ROI was reduced such that the heart was excluded again, in order to estimate the circumferential stretch more accurately.

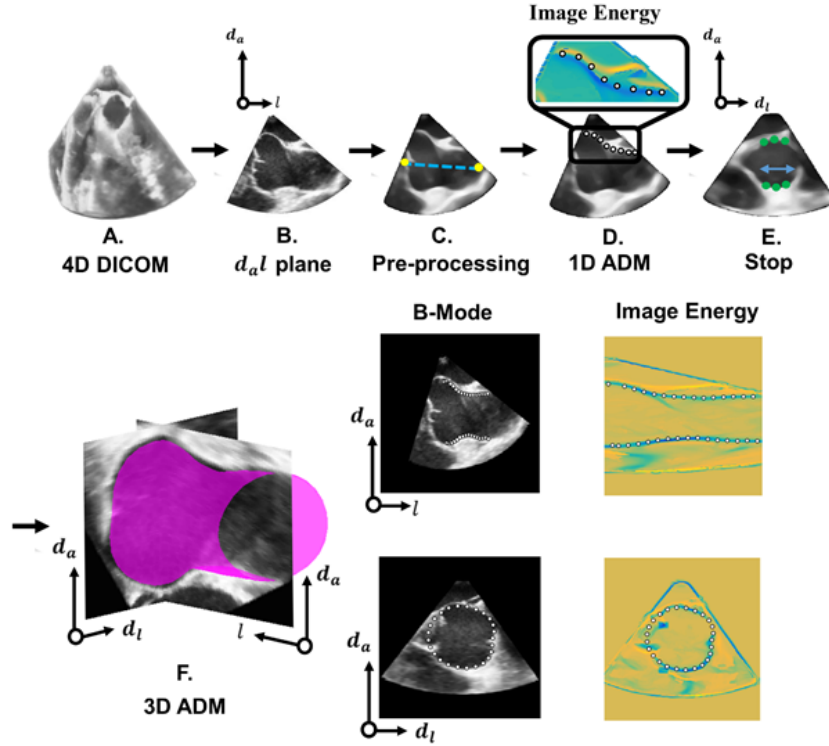


Figure 5.2: An overview of the segmentation process. A- Initially, in the 4D DICOM data, a slice which contains the aorta was manually located B- The automatic segmentation was initialized by selecting two points within the aortic segment. C- Subsequently Euclidean Shortening flow (ESF) filtering was performed. D- The 2D segmentation was applied by solving the minimization problem, i.e., the shape deforms such that the image energy is minimized while the internal energy of the shape prevents discontinuities. E- This is repeated for neighboring slices until the deviation with the previous segmentation exceeded a set threshold. F- The resulting geometry was used as initial geometry for the 3D ADM [144].

### 5.3.2 Iterative Finite Element Analysis

Van Disseldorp et.al [144] developed an iterative FE Analysis (FEA) which is not published yet. The material properties were estimated by an iterative FEM using Abaqus [72]. The aortic wall behaviour was modeled as an incompressible hyperelastic material using Neo-Hookean material model. The ATAA wall was meshed by hybrid elements with 8-node linear hexahedrons. The thickness was assumed homogeneous equal to 2.4 mm with two layer of elements in radial direction. The wall was fixed at the proximal side and in the z-plane at the distal side. To estimate the zero pressure geometry the backward incremental method was employed [40]. The proximal side was displaced with the estimated aortic root motion to simulate the in vivo longitudinal stretch. Subsequently, the patient-specific systolic pressure was applied to the lumen. Finally, the displacements of the aortic wall between the diastolic and systolic geometry were calculated by the FEM and compared to the US displacement data.

A gradient descent method was used to optimize the incremental material property,  $G_{FEA}$ , by minimizing the difference between the x- and y-displacements in the FEA and the ones derived

from the US data [143].

### 5.3.3 MRI

#### 5.3.3.1 Data acquisition and segmentation

One healthy volunteer was scanned on a 3T MR scanner (Siemens Magnetom Prisma) without contrast agent using a 4D flow protocol and sequence. Image acquisition was performed with a true spatial resolution of 1.9x1.9x2.2 mm, field of view (FOV)=360 mm, BW=740 Hz/pixel, flip angle=8°, TE/TR/TI=2.9/39.2/150 ms, venc=350 cm/s and phase duration=39,2 ms fixing the number of cardiac phases that hence depends on the cardiac cycle of the patient (ranging between 21-28 phases). A prospective ECG gating was used, the number of slices and rectangular FOV could be adjusted depending on the patient geometry [34]. The 4D flow MR data analysis and visualization was performed using cvi42 prototype 4DFlow module (cmr, Circle Cardiovascular Imaging Inc., Calgary, Canada).

Using MRI images of 10 phases a semi-automatic segmentation was implemented in Mimics as demonstrated in Fig. 5.3 for diastolic phase. The LESI methodology was applied for this healthy case and the extensional stiffness reconstruction was performed in both ascending and descending thoracic aorta (DTA). The only weakness of the acquired images is that the coronary artery was not visible enough in MRI images so that we were not able to define any reference close to the aortic root in order to adjust all phases longitudinally.

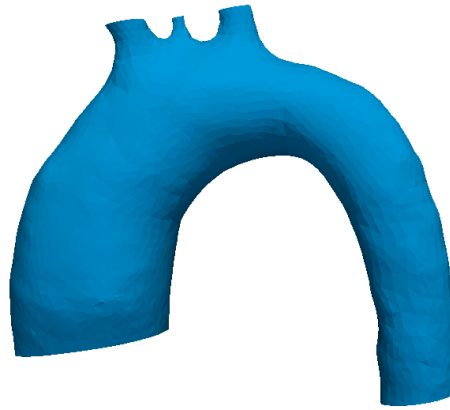


Figure 5.3: Segmented diastolic phases of a healthy case using MRI images.

#### 5.3.4 Theory of the LESI methodology

Relating the strains to tensions with the extensional stiffness, and writing the local equilibrium satisfied by the tensions, we derived the local extensional stiffness at every position as explained in detail in chapter 3 [52]

$$Q = \frac{\Delta P + \frac{\tau_1^0 \Delta r_1}{(r_1^0)^2} + \frac{\tau_2^0 \Delta r_2}{(r_2^0)^2}}{\frac{\varepsilon_1(t) + \nu \varepsilon_2(t)}{r_1^0} + \frac{\nu \varepsilon_1(t) + \varepsilon_2(t)}{r_2^0}} \quad (5.3)$$

where  $\Delta P = (P_{sys} - P_{dias})/2$  with  $P_{dias}$ ,  $P_{sys}$  corresponding to diastolic and systolic pressures, respectively,  $\tau_1^0$  and  $\tau_2^0$  denote the pretensions existing in the average geometry,  $\varepsilon_1$  and  $\varepsilon_2$  are strains in circumferential and axial directions due to displacements in between diastolic and systolic phases and  $\nu$  is the Poisson's ratio.  $r_1^0$  and  $r_2^0$  denote the radii in circumferential and longitudinal directions, respectively, while  $\Delta r_1$  and  $\Delta r_2$  are the fundamentals of the circumferential and longitudinal radii of curvature, respectively. To obtain  $r_1$  and  $r_2$ , we developed a method based on the principle of virtual work as described in detail in [52]. The LESI method was summarized in a flowchart in Figure 3.3 [52].

## 5.4 Results

### 5.4.1 US

The displacement reconstruction through ATAA was available from [144] as shown in Fig. 5.4. Fig. 5.5 shows the map of extensional local stiffness distribution through ATA. The results show a heterogeneity in ATA whereas the material was stiff in the regions of inner and outer curvature of ATA compared to other regions. The high stiffness of the inner curvature can be justified by the effect of surrounding tissue and contact with the pulmonary artery. An average linearized extensional stiffness of 4.3 MPa.mm was found across the whole ATAA.

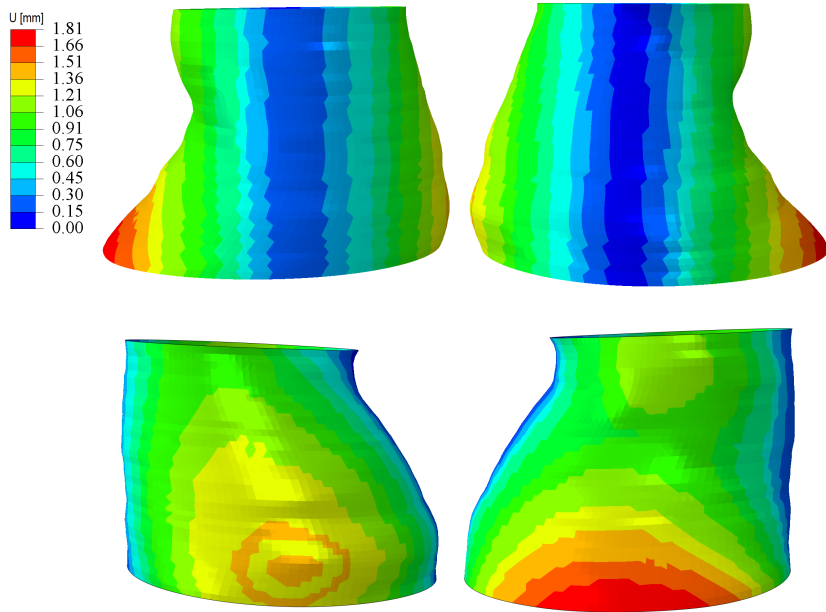


Figure 5.4: Displacement [mm] reconstruction of a patient affected by ATAA using US images.

### 5.4.2 MRI

For the case of MRI images we applied the whole LESI method except definition of coronary arteries [52]. The stiffness distribution demonstrated in Fig. 5.6 showed a heterogeneity in the ATA. The effect of surrounding tissue and contact with the pulmonary artery is observed

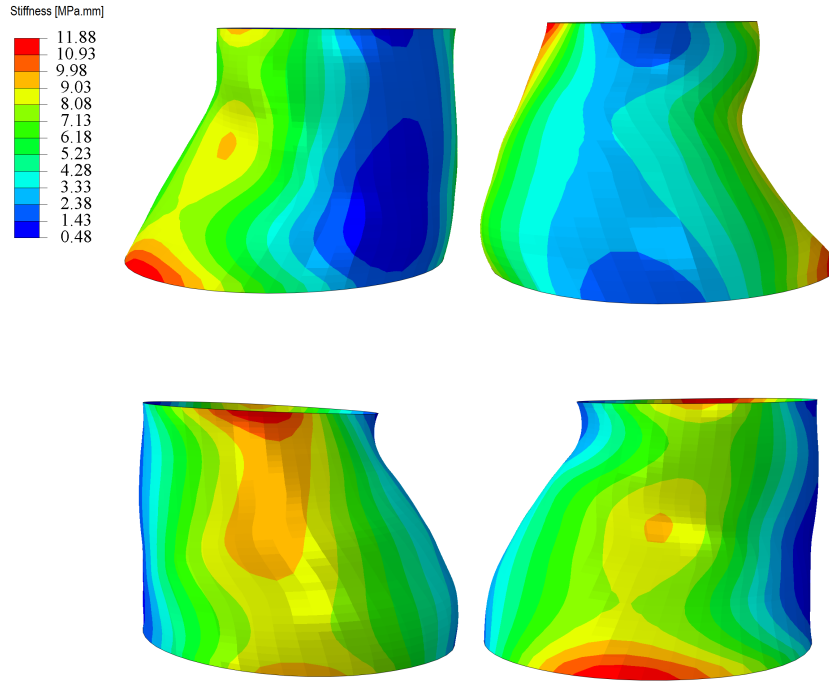


Figure 5.5: Local extensional stiffness map [MPa.mm] of a patient with ATAA using US images.

in the inner curvature of ATA. We derived a mean value of extensional stiffness equal to 3.3 MPa.mm for ATA and 1.8 MPa.mm for DTA. The comparison of these results with the identified extensional stiffness of real patients in [52] shows that the derived extensional stiffness for this healthy case is lower, confirming that the healthy tissue is more extensible.

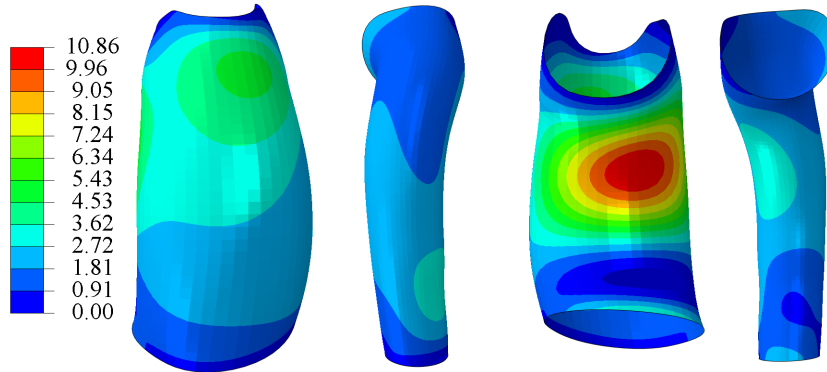


Figure 5.6: Local extensional stiffness [MPa.mm] map of healthy case using MRI images.

## 5.5 Discussion

The average extensional stiffness of 4.3 MPa.mm obtained by the LESI method was compared with the stiffness identified by iterative FEA. Van Disseldorp et al. [144] applied their methodology (iterative FEA) on the same patient with US images and they obtained a value in the range of 0.3-0.6 MPa for shear modulus. If we relate the shear and Young modulus together

assuming homogeneous isotropic material we can write in isotropic linear elasticity:

$$G = \frac{E}{2(1 + \nu)}; \quad \text{with} \quad E = \frac{(1 - \nu^2)Q}{h} \quad (5.4)$$

where,  $E$  is the Young's modulus,  $G$  is shear modulus,  $\nu$  is Poisson's ratio and  $h$  is aortic thickness. As mentioned above we obtained on average  $Q = 4.3$  MPa.mm so that using Eq. 5.4 and recalling that  $h = 2.4$  mm, we obtain  $G = 0.44$  MPa which is in good agreement with the results of iterative Finite Element Analysis (0.2 to 0.6 MPa) [144].

The results from MRI images for a healthy case was satisfactory in which we were expecting a low extensional stiffness. Based on our previously published results [52] the average extensional stiffness for ATAA patients was  $\sim 3.4$ - $5.5$  MPa.mm in ATAAs. The comparison of the average extensional stiffness of a healthy and ATAA patients showed that extensional stiffness of healthy case is lower than that of ATAA patients. Some limitations of using MRI images can still be reported:

1. We attempted to apply the LESI method on available ATAA patients using MRI images but it failed. The images of ATAA patients had low spatial resolution and the presence of the noise to use for geometry reconstruction in MIMICS (see appendix). This is the reason why the LESI methodology is here applied for a healthy case whose images had better quality.
2. The coronary artery was not easy to recognize in MRI images during segmentation even in healthy case. It can be due to heart motion, as coronary arteries are close to the aortic root. In addition, the number of slices in MRI images for available patients is not enough to recognize the coronary artery. Therefore, here we were not able to include longitudinal displacements due to the heart motion in the extensional stiffness reconstruction.
3. We will test to reconstruct the geometries through a cardiac cycle using CRIMSON and Circle Cardiovascular Imaging<sup>®</sup> software (see appendix). In the future for ATAA patients we may need to use some methodologies to improve the resolution of the MRI images.

## 5.6 Future work: assessment of correlations between wall shear stress and stiffness

Altered wall shear stress (WSS) may activate inhibition of signaling pathways, leading to extracellular matrix (ECM) degradation and remodeling, resulting in wall stiffening. Several studies have shown that shear stress induces several genes that encode proteins implicated in atherosclerosis and other vascular diseases [107, 126]. Guzzardi et al. investigated the relationship between WSS and regional aortic tissue remodeling to characterize the effect of regional WSS on the dysregulation of ECM in BAV patients. Patients who underwent ascending aortic resection and 4D flow CMR in the meantime were recruited, to regionally map WSS. Moreover, aortic wall samples were collected and compared for medial elastin degeneration



by histology and ECM regulation by protein expression. They reported that areas with high WSS correspond with ECM dysregulation and concluded that elastic fiber degeneration is a effective factor in the development of aortic diseases [66]. Jalali et al. [83] aimed to explain the mechanism of the upstream signaling that contributes to the shear stress activation of mitogen-activated protein kinases (MAPKs) in vascular endothelial cells. These results show that the typical proteins affect the signaling pathways in reaction to wall shear stress. Therefore, we want to validate such hypothesis by looking at correlations with our methods. As future work it will be interesting to investigate the correlation between WSS using 4D flow MRI [34] and local extensional stiffness distribution obtained with the LESI methodology [52] applied on the same 4D MRI scans. At this stage we were not able to apply the LESI methodology on MRI data of an ATAA patient. As we still desired to make a first proof of concept to derive correlations between WSS and local extension stiffness distribution, we worked with data of a patient who was imaged preoperatively both with gated CT and 4D flow MRI.

Our research group recently developed a computational fluid dynamics (CFD) analysis framework based on 4D MRI datasets. This permits to assess blood flow helicity and wall shear stress in patients affected by ATAA [34]. In the following paragraph, we summarize our methodology and show a first application towards the objective of finding correlations between WSS distribution and local extension stiffness.

Using 4D MRI data, the CRIMSON (Cardiovascular Integrated Modelling and Simulation) software was employed to reconstruct the late systolic phase 3D aortic geometries. Afterwards, the 3D aortic geometries were imported in Ansys-Fluent (ANSYS® Academic Research, Release 17.0) and were discretized using a tetrahedral mesh. Patient-specific velocity profiles which were extracted from the 4D flow-MRI were used to define the inflow boundary condition at the inlet of the aorta. To analyze the flow in the patient-specific geometries, the Navier–Stokes equations assuming incompressible continuity were solved. The outlet boundary conditions at the apico-aortic branches was assigned using the patient-specific pulsatile flow rate obtained from 4D MRI analysis. To describe the hemodynamics at the descending aorta outlet, a multi-scale scheme was developed and the 3D domain was coupled with 3 elements windkessel model. The three-elements windkessel model is a zero-dimensional electric circuit analogue which uses two resistors to represent the vasculature resistance and a capacitor to represent the vessel compliance. Given a target diastolic and systolic pressure, the value of the impedance ( $Z_c$ ), the distal resistance ( $R$ ) and the capacitor ( $C$ ) were tuned to produce the same flow rate waveform obtained from the 4D MRI datasets.

Aortic walls were assumed to be rigid and impermeable, and a no-slip condition was used. Blood was treated as a non-Newtonian fluid using Carreau model. Magnitude of the Time Average WSS (TAWSS) was measured along three cardiac cycles by integrating magnitude of each nodal WSS over the cardiac cycle as [34]

$$TAWSS = \frac{1}{T} \int_0^T WSS \, dt \quad (5.5)$$

The Oscillatory Shear Index (OSI) was used to identify the presence of high oscillatory WSS direction during the cardiac cycle and was calculated as [34]

$$OSI = 0.5 \left[ 1 - \left( \frac{\int_0^T WSS(s, t).dt}{\int_0^T |WSS(s, t)|.dt} \right) \right] \quad (5.6)$$

In Fig. 5.7 the registration of diastolic geometries from both CT scans and MRI scans is demonstrated based on an iterative closest point algorithm which was developed for registration. It is obvious that boundaries of both geometry are not perfectly fitted, however their configurations are similar. Fig. 5.8 shows the TAWSS and the OSI obtained from the CFD analysis and local extensional stiffness obtained with the LESI method of a ATAA patient in different views. The maximum TAWSS and OSI were derived at the systolic phase and the maximum stiffness was observed in the bulged region of the aorta. It is an ongoing work that involves a collaboration with Dr. Francesca Condemi from University of Toronto, Professor Diego Gallo and Professor Umberto Morbiducci from Politecnico di Torino.

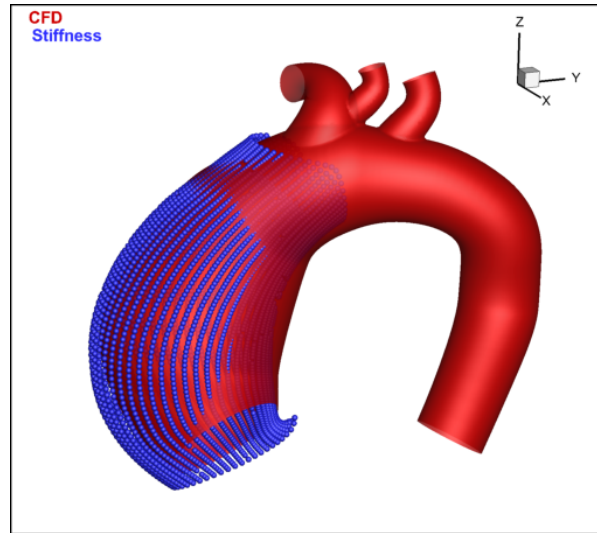


Figure 5.7: Registration of geometries segmented from MRI (red) and CT (blue dots) scans together.

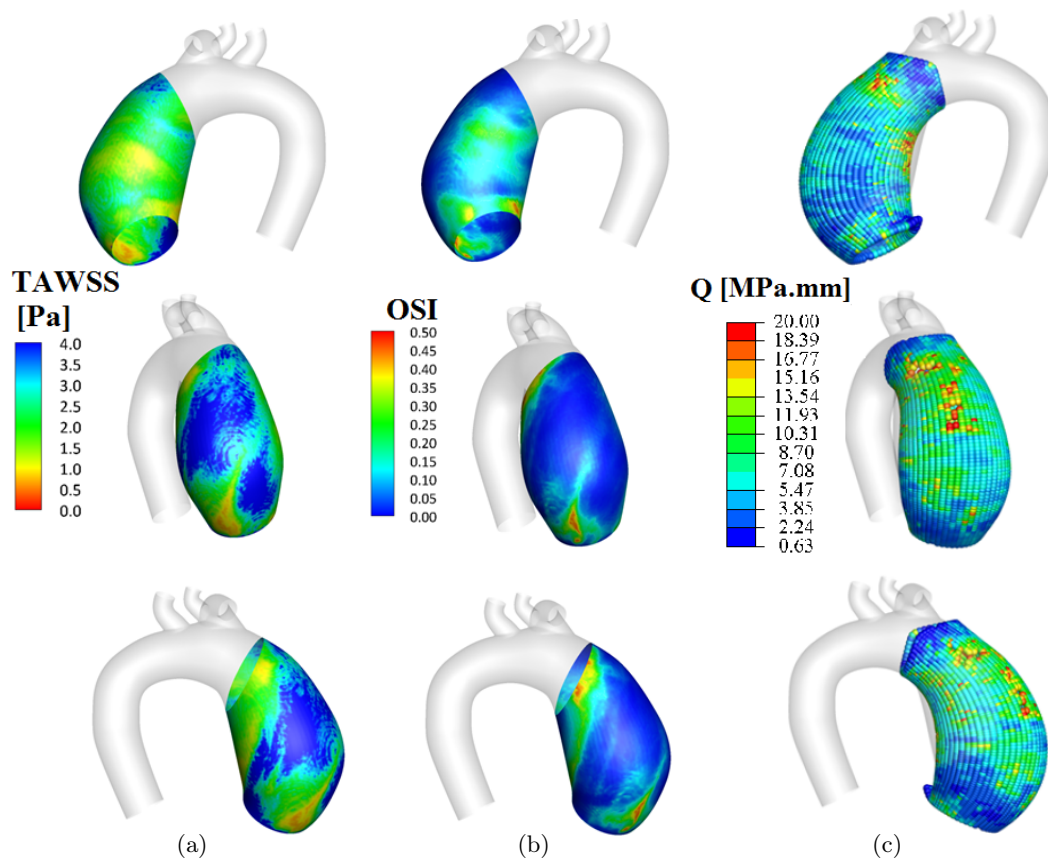


Figure 5.8: a- TAWSS, b- OSI resulting from the CFD analysis and c- extensional stiffness distribution from LESI method in different views.



---

## General Conclusion

In this thesis, we developed a method that could be helpful in the future for decision making of surgical intervention in patients affected by an ascending thoracic aortic aneurysm (ATAA). After reviewing the state of the art in the first chapter it was shown that it is essential to enable noninvasive identification of the in vivo local stiffness of ATAA to estimate a reliable rupture risk criterion. To this aim, strain reconstruction of ATAA is necessary. To facilitate the process of strain reconstruction it is required to track the same identical material points between different phases of a cardiac cycle. To this aim, two methods of mesh morphing were developed and evaluated in the second chapter to calculate the displacements between a reference and a target geometry. The results of the first method which interpolates the coordinates of the reference mesh onto a target model based on the calculation of the parametric coordinates was more precise. Consequently, it was used for the reconstruction of ATAA strain maps in the other chapters. Regional variations of stiffness properties across ATAA were first reconstructed on 3 patients noninvasively. To achieve this reconstruction, a novel noninvasive inverse method, named LESI, was developed based on preoperative gated CT scans. According to our results the regional stiffness distribution appeared heterogeneous across the ATAA. Averagely, the identified stiffness obtained by the LESI method was also compared with values obtained using other non-local methodologies [44, 138]. It was also interesting to consider a cohort with a larger number of patients in order to interpret regional variations of stiffness properties in ATAAs. Therefore, in chapter 4, the LESI method was employed to reconstruct noninvasively the stiffness distribution of the ascending thoracic aorta of 11 patients based on their preoperative gated CT scans. A very good correlation was found between the rupture risk criterion and the local extensional stiffness values obtained by the LESI methodology. Finally it was shown that patients can be separated in two groups: a group of stiff and brittle ATAA with a rupture risk criterion above 0.9, and a group of relatively compliant ATAA with a rupture risk below 0.9. These results need to be repeated on larger cohorts of patients to perform an accurate statistical analysis. However, the analysis of 11 patients showed that local aortic stiffness was an important determinant of the ATAA rupture risk.

Based on previously published articles using MRI and US data, it was interesting to reconstruct local extensional stiffness by employing these acquisition methods, which are much less harmful to a patient in comparison with CT scans. Therefore, in chapter 5, MRI and US data were employed to generate aortic geometries. Afterwards, the LESI method was applied on the other

datasets to reconstruct the local extensional stiffness of ATAAs. Several limitations of LESI method can be discussed.

1. We assumed that the aortic wall behaves as a membrane with no bending moments or no shear through the thickness. Regions near the branches were removed from the analysis because they may not satisfy the membrane assumption.
2. Using of Xray can be a limitation for an extensive use of the methodology, especially if it is repeated for the identification of aortic stiffness at different ages of ATAA growth, it induces frequent irradiation for the patient.
3. A linear elastic material is assumed for the wall within the systolic-diastolic range and we ignored the layer-specific wall properties and residual stresses existing in the ATAA wall.
4. We here assumed an isotropic behavior of the arterial wall. It was not possible to consider anisotropic effects as only one type of loading was available. Therefore, the identified extensional stiffness in this thesis is a combination of the axial and circumferential stiffness.
5. Average tensions existing in the aorta due to the action of the average blood pressure are also involved in this study. This comes from geometrical nonlinearity involved in finite deformations [18]. These tensions were approximated using the approach of [85] which consists in achieving a linear elastic stress analysis on the same structure as the aorta, assigning a very large elastic modulus.
6. The arterial wall was considered as a 3D membrane with uniform thickness.
7. The reconstructed geometries have some local irregularities due to image noise at each phase of the cardiac cycle. The spatial frequency of these irregularities is high and their effect is filtered out by Fourier polynomial smoothing.

In the future it would be interesting to derive the extensional stiffness using the LESI methodology on patients for whom we know where a dissection occurred. Afterwards, we can check the correlation between location of dissection and peak of extensional stiffness or peak wall stress. Moreover, we plan to use the LESI methodology and 4D flow MRI to understand the correlation between local wall shear stress distributions and local extensional stiffness distributions using statistical analyses [116].

# Bibliography

---

- [1] <http://sibere.co/ascending-aortic-root-repair.html>.
- [2] <https://www.webmd.com/heart-disease/heart-disease-aortic-aneurysm1>.
- [3] <https://m.ufhealth.org/uf-health-aortic-disease-center/thoracic-aortic-aneurysm>.
- [4] Cardiovascular system. <https://sites.google.com/a/st.cabarrus.k12.nc.us/3rd-period-group-2-basketball/circulatory-system>.
- [5] Overview of the vascular system. [https://www.hopkinsmedicine.org/healthlibrary/conditions/cardiovascular\\_diseases/overview\\_of\\_the\\_vascular\\_system\\_85,P08254](https://www.hopkinsmedicine.org/healthlibrary/conditions/cardiovascular_diseases/overview_of_the_vascular_system_85,P08254).
- [6] <http://www.aortarepair.com/type-a-aortic-dissection.html>, 2019.
- [7] Aorta: Aortic aneurysm. <https://my.clevelandclinic.org/health/diseases/16742-aorta-aortic-aneurysm>, 2019.
- [8] P.A. Abraham, A.J. Perejda, W.H. Carnes, and J. Uitto. Marfan syndrome. demonstration of abnormal elastin in aorta. *J Clin Invest*, 70(6):1245–52, 1982.
- [9] L. Andreotti, A. Bussotti, D. Cammelli, F. di Giovine, S. Sampognaro, G. Sterrantino, G. Varcasia, and P. Arcangeli. Aortic connective tissue in ageing—a biochemical study. *Angiology*, 36(12):872–9, 1985.
- [10] L. Antiga, B. Ene-Iordache, and A. Remuzzi. Computational geometry for patient-specific reconstruction and meshing of blood vessels from MR and CT angiography. *IEEE Transactions on Medical Imaging*, 22(5):674–84, 2003.
- [11] L. Antiga and D.A. Steinman. Robust and objective decomposition and mapping of bifurcating vessels. *IEEE Trans Med Imaging*, 23(6):704–13, 2004.
- [12] A. Arani, SP. Arunachalam, ICY. Chang, F. Baffour, PJ. Rossman, KJ. Glaser, JD. Trzasko, KP. McGee, A. Manduca, M. Grogan, A. Dispenzieri, RL. Ehman, and PA. Araoz. Cardiac mr elastography for quantitative assessment of elevated myocardial stiffness in cardiac amyloidosis. *J Magn Reson Imaging.*, 46(5):1361–1367, 2017.

- [13] S. Avril, P. Badel, and A. Duprey. Anisotropic and hyperelastic identification of in vitro human arteries from full-field optical measurements. *Journal of biomechanics*, 43:2978–85, 2010.
- [14] S. Avril and S.Evans. Material parameter identification and inverse problems in soft tissue biomechanics. *Springer, CISM International Center for Mechanical Sciences 573 Courses and Lectures*.
- [15] AN. Azadani, S. Chitsaz, A. Mannion, A. Mookhoek, A. Wisneski, JM. Guccione, MD. Hope, L. Ge, and EE. Tseng. Biomechanical properties of human ascending thoracic aortic aneurysms. *Ann Thorac Surg*, 96(1):50–8, 2013.
- [16] P. Badel, K. Genovese, and S. Avril. 3D residual stress field in arteries: novel inverse method based on optical full-field measurements. *Int J Cardiol Heart Vasc*, 6 (2012):528–38, 2013.
- [17] H. Bader. Dependence of wall stress in the human thoracic aorta on age and pressure. *Circ Res*, 20(3):354–61, 1967.
- [18] S. Baek, R.L. Gleason, K.R. Rajagopal, and J.D. Humphrey. Theory of small on large: potential utility in computations of fluid–solid interactions in arteries. *Comput Methods Appl Mech Eng*, 196:3070–78, 2007.
- [19] MR. Bersi, C. Belliniand, P. Di Achille, J.D. Humphrey, K. Genovese, and S. Avril. Novel methodology for characterizing regional variations in the material properties of murine aortas. *Journal of biomechanical engineering*, 138:071005, 2016.
- [20] M.E. Biancolini. Mesh morphing and smoothing by means of radial basis functions (rbf): A practical example using Fluent and RBF morph. *Handbook of Research on Computational Science and Engineering: Theory and Practice*, 2:DOI: 10.4018/978–1–61350–116–0.ch015, 2011.
- [21] M.E. Biancolini. Fast radial basis functions for engineering applications. *Springer*, 2017.
- [22] M.E. Biancolini and P.P. Valentini. Virtual human bone modelling by interactive sculpting, mesh morphing and force-feedback. *Journal for Interactive Design and Manufacturing (IJIDeM)*, pages DOI: 10.1007/s12008–018–0487–3, 2018.
- [23] L.K. Bickerstaff, P.C. Pairolero, L.H. Hollier, L.J. Melton, H.J. Van Peenen, and K.J. Cherry et al. Thoracic aortic aneurysms: a population–based study. *Surgery*, 92:1103–08, 1982.
- [24] M.D. Buhmann. Radial basis functions. *Cambridge University Press, New York, USA*, 2003.



- 
- [25] K. Capellini, E. Costa, M.E. Biancolini, E. Vignali, V. Positano, L. Landini, and S. Celi. An image-based and rbf mesh morphing cfd simulation for ataa hemodynamic. *ESB-ITA-2017*, 2017.
  - [26] L. Cardamone, A. Valentin, J.F. Eberth, and J.D. Humphrey. Incompressibility of the human arterial wall: an in vitro ultrasound study. *J Hypertens Suppl.*, 10(6):S111–4, 1992.
  - [27] L. Cardamone, A. Valentin, J.F. Eberth, and J.D. Humphrey. Origin of axial prestretch and residual stress in arteries. *Biomech Model Mechanobiol*, 8(6):431—46, 2009.
  - [28] T.E .Carew, R.N. Vaishnav, and D.J. Patel. Compressibility of the arterial wall. *Circ Res.*, 23(1):61–8, 1968.
  - [29] K.H. Chau and J.A. Elefteriades. Natural history of thoracic aortic aneurysms: size matters and plus moving beyond size. *Prog Cardiovasc Dis*, 56(1):74–80, 2013.
  - [30] N. Choudhury, B. Olivier, R. Leonie, T. Dominique, C. Raymond, and B. Jagdish et al. Local mechanical and structural properties of healthy and diseased human ascending aorta tissue. *Cardiovasc Pathol*, 18:83–91, 2009.
  - [31] J. M. Clark and S. Glagov. Transmural organization of the arterial media. the lamellar unit revisited. *Send to Arteriosclerosis*, 5(1):19–34, 1985.
  - [32] M.A. Coady, J.A. Rizzo, G.L. Hammond, G.S. Kopf, and J.A. Elefteriades. Surgical intervention criteria for thoracic aortic aneurysms: a study of growth rates and complications. *Ann Thorac Surg*, 67(6):1922–6, 1999.
  - [33] M.A. Coady, J.A. Rizzo, G.L. Hammond, D. Mandapati, U. Darr, G.S. Kopf, and J.A. Elefteriades. What is the appropriate size criterion for resection of thoracic aortic aneurysms? *J Thorac Cardiovasc Surg*, 113(3):476–91, 1997.
  - [34] F. Condemi, S. Campisi, M. Viallon, T. Troalen, G. Xuexin, A.J. Barker, M. Markl, P. Croisille, O. Trabelsi C. Cavinato, A. Duprey, and S. Avril. Fluid- and biomechanical analysis of ascending thoracic aorta aneurysm with concomitant aortic insufficiency. *Ann Biomed Eng.*, 45(12):2921–2932, 2017.
  - [35] Wikipedia contributors. aortic dissection. [https://en.wikipedia.org/w/index.php?title=Aortic\\_dissection&oldid=871520225](https://en.wikipedia.org/w/index.php?title=Aortic_dissection&oldid=871520225), 2018.
  - [36] B. Couteaua, Y. Payanb, and S. Lavallée. The mesh-matching algorithm: an automatic 3d mesh generator for finite element structures. 33:1005–1009, 2000.
  - [37] P. Daniel and M.D. Judge. Marfan’s syndrome. *Ann Vasc Surg*, 366(9501):1965—76, 2005.

- [38] F.M. Davis, Y. Luo, S. Avril, Ambroise A. Duprey, and J. Lu. Local mechanical properties of human ascending thoracic aneurysms. *Journal of the mechanical behavior of biomedical materials*, 61:235–49, 2016.
- [39] FM. Davis, Y. Luo, S. Avril, A. Duprey, and J. Lu. Pointwise characterization of the elastic properties of planar soft tissues: application to ascending thoracic aneurysms. *Biomechanics and modeling in mechanobiology*, 14:967–78, 2015.
- [40] S. de Putter, B. J. Wolters, M.C. Rutten, M. Breeuwer, F. A. Gerritsen, and F. N. van de Vosse. Patient-specific initial wall stress in abdominal aortic aneurysms with a backward incremental method. *J Biomech*, 40(5):1081–90, 2007.
- [41] RP. Deveja, D.C. Iliopoulos, E.P. Kritharis, D.C. Angouras, D. Sfyris, SA. Papadodima, and DP. Sokolis. Effect of aneurysm and bicuspid aortic valve on layer-specific ascending aorta mechanics. *Ann Thorac Surg*, 106(6):1692–1701, 2018.
- [42] P.B. Dobrin and J.M. Doyle. Vascular smooth muscle and the anisotropy of dog carotid artery. *Circ Res*, 27(1):105–19, 1970.
- [43] A. Duprey, K. Khanafer, M. Schlicht, S. Avril, D. Williams, and R. Berguer. In vitro characterisation of physiological and maximum elastic modulus of ascending thoracic aortic aneurysms using uniaxial tensile testing. *Eur J Vasc Endovasc Surg*, 39(6):700–7, 2010.
- [44] A. Duprey, O. Trabelsi, M. Vola, J.P. Favre, and S. Avril. Biaxial rupture properties of ascending thoracic aortic aneurysms. *Acta Biomater*, 42:273–85, 2016.
- [45] T. McGloughlin (Ed.), editor. *Biomechanics and mechanobiology of aneurysms*. Springer-Verlag, Heidelberg, 2011.
- [46] M.D. Roswell Eldridge. Coarctation in the marfan syndrome. *Arch Intern Med*, 113(3):342–49, 1964.
- [47] J.A. Elefteriades and E.A. Farkas. Thoracic aortic aneurysm clinically pertinent controversies and uncertainties. *J Am Coll Cardiol*, 55(9):841–57, 2010.
- [48] L. Emerel, J. Thunes, T. Kickliter, M. Billaud, JA. Phillippi, DA. Vorp, and TG. Gleason S. Maiti. Pre-dissection-derived geometric and distensibility indices reveal increased peak longitudinal stress and stiffness in patients sustaining acute type a aortic dissection: Implications for predicting dissection. *The Journal of Thoracic and Cardiovascular Surgery*, page doi: <https://doi.org/10.1016/j.jtcvs.2018.10.116>, 2018.
- [49] S. Emile and S. Ying. The ascending aortic aneurysm: When to intervene? *Int J Cardiol Heart Vasc*, 6:91—100, 2015.

- 
- [50] M. Faber and G. Møller-Hou. The human aorta. v. collagen and elastin in the normal and hypertensive aorta. *Acta Pathol Microbiol Scand*, 31(3):377–82, 1952.
  - [51] M. A. Farber and T. S. Ahmad. Aortic dissection. *University of North Carolina*, 2017.
  - [52] S. Farzaneh, O. Trabelsi, and S. Avril. Inverse identification of local stiffness across ascending thoracic aortic aneurysms. *Biomechanics and Modeling in Mechanobiology*, pages doi: 10.1007/s10237-018-1073-0, 2018.
  - [53] A. Ferrara, S. Morganti, P. Totaro, A. Mazzola A, and F. Auricchio. Human dilated ascending aorta: Mechanical characterization via uniaxial tensile tests. *J Mech Behav Biomed Mater*, 53:257–71, 2016.
  - [54] M.F. Fillinger, S.P. Marra, M.L. Raghavan, and F.E. Kennedy. Prediction of rupture risk in abdominal aortic aneurysm during observation: wall stress versus diameter. *J Vasc Surg*, 37(4):724–32, 2003.
  - [55] N. Flores, J. Inman, M. Lum, Z. Wang, Y. Xuan, M. D Hope, L. Ge, and E. E Tseng. Ascending thoracic aortic aneurysm wall stress analysis based in surgical vs. nonsurgical patients. *44<sup>th</sup> Annual Meeting Western thoracic surgical association*, 2018.
  - [56] E. Fonck, G. Prod’hom, S. Roy, L. Augsburger, D.A. Rüfenacht, and N. Stergiopulos. Effect of elastin degradation on carotid wall mechanics as assessed by a constituent-based biomechanical model. *Am J Physiol Heart Circ Physiol*, 292(6):H2754–63, 2007.
  - [57] H.L. Fred. Drawbacks and limitations of computed tomography. *Gen Thorac Cardiovasc Surg*, 31(4):345–348, 2004.
  - [58] Y.C. Fung. *Biomechanics. Mechanical properties of living tissues*. Springer, 1993.
  - [59] M. Ben Gadri, Y. Arous, S. Bouguerra, M. Aloui, S. Kouki, H. Boujemaa, and N. Ben Abdallah. Bicuspid aortic valve: Role of cardiac mdct and cardiac mr imaging. *ECR 2015*, C-2274:10.1594/ecr2015/C-2274, 2015.
  - [60] C.M. García-Herrera, J.M. Atienza, F.J. Rojo, E. Claes, G.V. Guinea, D.J. Celentano, C. García-Montero, and R.L. Burgos. Mechanical behaviour and rupture of normal and pathological human ascending aortic wall. *Med Biol Eng Comput*, 50(6):559–66, 2008.
  - [61] J.P. Vande Geest, E.S. Di Martino, A. Bohra, M.S. Makaroun, and D.A. Vorp. A biomechanics-based rupture potential index for abdominal aortic aneurysm risk assessment: demonstrative applicatio. *Ann N Y Acad Sci*, 1085:11–21, 2006.
  - [62] J.P. Vande Geest, M.S. Sacks, and D.A. Vorp. Age dependency of the biaxial biomechanical behavior of human abdominal aorta. *J Biomech Eng*, 126:815–22, 2004.
  - [63] G. H. Gibbons and V.J. Dzau. The emerging concept of vascular remodeling. *N Engl J Med*, 330(20):1431–8, 1994.
-

- [64] SR. Greenberg. The association of medial collagenous tissue with atheroma formation in the aging human aorta as revealed by a special technique. *Am J Cardiol*, 1(4):323–6, 1986.
- [65] M. Groenink, A. de Roos, BJ. Mulder, JA. Spaan, and EE. van der Wall. Changes in aortic distensibility and pulse wave velocity assessed with magnetic resonance imaging following beta-blocker therapy in the marfan syndrome. *Am J Cardiol*, 82:203–8, 1998.
- [66] D.G. Guzzardi, A.J. Barker, Ooi.P van, SC. Malaisrie, J.J. Puthumana, D.D. Belke, H.E. Mewhort, D.A. Svystonyuk, S. Kang, S. Verma, J. Collins, J. Carr, R.O. Bonow, M. Markl, J.D. Thomas, P.M. McCarthy, and P.W. Fedak. Valve-related hemodynamics mediate human bicuspid aortopathy: Insights from wall shear stress mapping. *J Am Coll Cardiol*, 66(8):892–900, 2015.
- [67] T. Hagerty, P. Geraghty, and A.C. Braverman. Abdominal aortic aneurysm in marfan syndrome. *Ann Vasc Surg.*, 40:294.e1–294.e6, 2017.
- [68] S. Haker, S. Angenent, A. Tannenbaum, and R. Kikinis. Nondistorting flattening maps and the 3-D visualization of colon ct images. *IEEE trans. med. imaging*, 19:665–670, 2000.
- [69] T. Halme, T. Savunen, H. Aho, T. Vihersaari, and R. Penttinen. Elastin and collagen in the aortic wall: changes in the marfan syndrome and annuloaortic ectasia. *Angiology*, 43(1):1–12, 1985.
- [70] G.M. Hass. A study of the elasticity and tensile strength of elastic tissue isolated from the human aorta. *Elastic tissue II*, 34:971, 1942.
- [71] K .Hayashi. Experimental approaches on measuring the mechanical properties and constitutive laws of arterial walls. *J Biomech Eng*, 115(4B):481–8, 1993.
- [72] Hibbit, Karlson, and Sorensen. *Abaqus-Theory manual*, 6.11-3 edition, 2011.
- [73] G.A. Holzapfel. Determination of material models for arterial walls from uniaxial extension tests and histological structure. *J Theor Biol*, 238:290–302, 2006.
- [74] G.A. Holzapfel, T.C. Gasser, and R.W. Ogden. A new constitutive framework for arterial wall mechanics and a comparative study of material models. *Journal of elasticity and the physical science of solids*, 61(1-3):1–48, 2000.
- [75] GA. Holzapfel, TC. Gasser, and RW. Ogden. A new constitutive framework for arterial wall mechanics and a comparative study of material models. *Journal of elasticity and the physical science of solids*, 61 (1):1–48, 2000.
- [76] G.A. Holzapfel, G. Sommer, C.T. Gasser, and P. Regitnig. Determination of layer-specific mechanical properties of human coronary arteries with nonatherosclerotic intimal thickening and related constitutive modeling. *Am J Physiol Heart Circ Physiol*, 289(5):H2048–58, 2005.

- 
- [77] Y. Hosoda, K. Kawano, F. Yamasawa, T. Ishii, T. Shibata, and S. Inayama. Age-dependent changes of collagen and elastin content in human aorta and pulmonary artery. *Angiology*, 35(10):615–21, 1984.
  - [78] Y. Hosoda and I. Minoshima. Elastin content of the aorta and the pulmonary artery in the japanese. *Angiology*, 16:325–32, 1965.
  - [79] J.D. Humphrey. Vascular adaptation and mechanical homeostasis at tissue, cellular, and sub-cellular levels. *Cell Biochem Biophys*, 50:53–78, 2008.
  - [80] J.D. Humphrey. Cardiovascular solid mechanics cells, tissues, and organs. *Springer Science Business Media*, 2013.
  - [81] D.C. Iliopoulos, R.P. Deveja, E.P. Kritharis, D. Perrea, G.D. Sionis, K. Toutouzas, C. Stefanadis, and D.P. Sokolis. Regional and directional variations in the mechanical properties of ascending thoracic aortic aneurysms. *Med Eng Phys*, 31(1):1–9, 2008.
  - [82] D.C. Iliopoulos, E.P. Kritharis, A.T. Giagini, and D.P. Sokolis S.A. Papadodima. Ascending thoracic aortic aneurysms are associated with compositional remodeling and vessel stiffening but not weakening in age-matched subjects. *J Thorac Cardiovasc Surg*, 137(1):101–9, 2009.
  - [83] S. Jalali, Y.S. Li, M. Sotoudeh, S. Yuan, S. Li, S. Chien, and J.Y. Shyy. Shear stress activates p60src-ras-mapk signaling pathways in vascular endothelial cells. *Arterioscler Thromb Vasc Biol*, 18(2):227–34, 1998.
  - [84] G. Johansson, U. Markström, and J. Swedenborg. Ruptured thoracic aortic aneurysms: a study of incidence and mortality rates. *J Vasc Surg*, 21(6):985–8, 1995.
  - [85] G.R. Joldes, K. Miller, A. Wittek, and B. Doyle. A simple, effective and clinically applicable method to compute abdominal aortic aneurysm wall stress. *J Mech Behav Biomed Mater*, 58:139–48, 2016.
  - [86] K. Kallenbach, TM. Sundt, and TH. Marwick. Aortic surgery for ascending aortic aneurysms under 5.0 cm in diameter in the presence of bicuspid aortic valve. *JACC Cardiovasc Imaging*, 6(12):1321–6, 2013.
  - [87] E.L. Kanabrocki, I.G. Fels, and E. Kaplan. Calcium, cholesterol, and collagen levels in human aortas. *J Gerontol*, 15:383–7, 1960.
  - [88] M. Kass, A. Witkin, and D. Terzopoulos. Snakes: Active contour models. *Int J Comput Vis*, 1:doi:10.1007/BF00133570, 1988.
  - [89] K. Khanafer, A. Duprey, M. Zainal, M. Schlicht, D. Williams, and R. Berguer. Determination of the elastic modulus of ascending thoracic aortic aneurysm at different ranges of pressure using uniaxial tensile testing. *J Thorac Cardiovasc Surg*, 142(3):682–6, 2011.

- [90] K. Krishnan, L. Ge, H. Haraldsson, MD. Hope, DA. Saloner, JM. Guccione, and EE. Tseng. Ascending thoracic aortic aneurysm wall stress analysis using patient-specific finite element modeling of in vivo magnetic resonance imaging. *Interact Cardiovasc Thorac Surg*, 21(4):471–80, 2015.
- [91] M.R. Labrosse. Cardiovascular mechanics. 2018.
- [92] Y. Lanir and Y.C. Fung. Two-dimensional mechanical properties of rabbit skin. ii. experimental results. *J Biomech*, 7(2):171–82, 1974.
- [93] A.I. Lansing, M. Alex, and T.B. Rosenthal. Calcium and elastin in human arteriosclerosis. *J Gerontol*, 5(2):112–9, 1950.
- [94] A. Leermans and D.K. Jones. The b-matrix must be rotated when correcting for subject motion in dti data. *Magn Reson*, 61:1336–49, 2009.
- [95] M. Liu, L. Liang, and W. Sun. A new inverse method for estimation of in vivo mechanical properties of the aortic wal. *J Mech Behav Biomed Mater*, 72:148–158, 2017.
- [96] J. Lu, X. Zhou, and M.L. Raghavan. Inverse elastostatic stress analysis in pre-deformed biological structures: demonstration using abdominal aortic aneurysms. *J Biomech*, 40:693–6, 2007.
- [97] P.G. Malvindi, S. Pasta, G.M. Raffa, and S. Livesey. Computational fluid dynamics of the ascending aorta before the onset of type a aortic dissection. *European Journal of Cardio-Thoracic Surgery*, 51(3):597–99, 2016.
- [98] C. Martin, W. Sun, T. Pham, and J. Elefteriades. Predictive biomechanical analysis of ascending aortic aneurysm rupture potential. *Acta Biomater*, 9(12):9392–400, 2013.
- [99] G. Martufi, T.C. Gasser, J.J. Appoo, and E.S. Di Martino. Mechano-biology in the thoracic aortic aneurysm: a review and case study. *Biomechanics and modeling in mechanobiology*, 13:917–928, 2014.
- [100] T. Matsumoto, K. Hayashi, and K. Ide. Residual strain and local strain distributions in the rabbit atherosclerotic aorta. *J Biomech*, 28(10):1207–17, 1995.
- [101] JB Michel, G Jondeau, and DM Milewicz. From genetics to response to injury: vascular smooth muscle cells in aneurysms and dissections of the ascending aorta. *Cardiovascular Research*, 114:578–589, 2018.
- [102] D. Mohan and J.W. Melvin. Failure properties of passive human aortic tissue. I-uniaxial tension tests. *J Biomech*, 15:887–902, 1982.
- [103] S.A. Mokashi and L.G. Svensson. Guidelines for the management of thoracic aortic disease in 2017. *Gen Thorac Cardiovasc Surg*, 10.1007:s11748–017–0831–8, 2017.

- 
- [104] S.J. Mousavi and S. Avril. Patient-specific stress analyses in the ascending thoracic aorta using a finite-element implementation of the constrained mixture theory. *Biomech Model Mechanobiol*, 16(5):1765–1777, 2017.
- [105] S.J. Mousavi, S. Farzaneh, and S. Avril. Computational predictions of damage propagation preceding dissection of ascending thoracic aortic aneurysms. *Int J Numer Method Biomed Eng*, 34(4):e2944, 2017.
- [106] V.C. Myers and W.W. Lang. Some chemical changes in the human thoracic aorta accompanying the aging process. *J Gerontol*, (Pt 1 4):441–4, 1946.
- [107] T. Nagel, N. Resnick, W.J. Atkinson, CF. Jr Dewey, and MA. Jr. Gimbrone. Shear stress selectively upregulates intercellular adhesion molecule-1 expression in cultured human vascular endothelial cells. *J Clin Invest*, 94(2):885–91, 1994.
- [108] University of Rochester medical center. <https://www.urmc.rochester.edu/encyclopedia/content.aspx?contenttypeid=85&contentid=P08254>.
- [109] R.J. Okamoto, J.E. Wagenseil, W.R. DeLong, S.J. Peterson, N.T. Kouchoukos, and T.M. Sundt 3rd. Mechanical properties of dilated human ascending aorta. *Ann Biomed Eng*, 30:624–35, 2002.
- [110] D. Oladokun, B.O. Patterson, J. Sobocinski, A. Karthikesalingam, I. Loftus, and P.J. Holt M.M. Thompson. Systematic review of the growth rates and influencing factors in thoracic aortic aneurysms. *Eur J Vasc Endovasc Surg*, 51(5):674–81, 2016.
- [111] B. Panek, M. Gacko, and J. Palka. Metalloproteinases, insulin-like growth factor-i and its binding proteins in aortic aneurysm. *Int J Exp Pathol*, 85(3):159—64, 2004.
- [112] S. Pasta, V. Agnese, M. Di Giuseppe, G. Gentile, GM. Raffa, D. Bellavia, and M. Pilato. In vivo strain analysis of dilated ascending thoracic aorta by ecg-gated ct angiographic imaging. *Ann Biomed Eng*, 45(12):2911–20, 2017.
- [113] S. Pasta, JA. PhillipiThomas, TG. Gleason, and DA. Vorp. Mechanical properties of ascending thoracic aortic aneurysm (ataa): Association with valve morphology. *Computer Models in Biomechanics*, pages 149–160, 2000.
- [114] D.J. Patel and D. L. Fry. Longitudinal tethering of arteries in dogs. *Circ Res.*, 19(6):1011–21, 1966.
- [115] D.J. Patel and R. N. Vaishnav. Basic hemodynamics and its role in disease processes. *Univ Park Press*, 23(1):61–68, 1968.
- [116] V. Peiffer, A. Bharath, S.J. Sherwin, and P.D. Weinberg. A novel method for quantifying spatial correlations between patterns of atherosclerosis and hemodynamic factors. *J Biomech Eng*, 135(2):doi: 10.1115/1.4023381, 2013.

- [117] A.J. Perejda, P.A. Abraham, W.H. Carnes, W.F. Coulson, and J. Uitto. Marfan's syndrome: structural, biochemical, and mechanical studies of the aortic media. *J Lab Clin Med*, 106(4):376–83, 1985.
- [118] P.J. Prendergast, C. Lally, S. Daly, A.J. Reid, T.C. Lee, and D. Quinn et al. Analysis of prolapse in cardiovascular stents: a constitutive equation for vascular tissue and finite-element modelling. *J Biomech Eng*, 125:692–99, 2003.
- [119] M.K. Pugsley and R. Tabrizchi. The vascular system: An overview of structure and function. *Journal of Pharmacological and Toxicological Methods*, 44(2):333–340, 2000.
- [120] V.S. Ramanath, J.K. Oh, T.M. Sundt 3rd, and K.A. Eagle. Acute aortic syndromes and thoracic aortic aneurysm. *Mayo Clin Proc*, 84(5):465–81, 2009.
- [121] A. Rinaudo and S. Pasta. Regional variation of wall shear stress in ascending thoracic aortic aneurysms. *Proc Inst Mech Eng H*, 228(6):627–638, 2014.
- [122] C.S Roy. The elastic properties of the arterial wall. *J Physiol.*, 3(2):125–159, 1881.
- [123] M. Sans and A. Moragas. Mathematical morphologic analysis of the aortic medial structure. *Anal Quant Cytol Histol.*, (15(2):93–100, 1993.
- [124] S.G. Sassani, S. Tsangaris, and D.P. Sokolis. Layer- and region-specific material characterization of ascending thoracic aortic aneurysms by microstructure-based models. *J Biomech*, 48(14):3757–65, 2015.
- [125] T.J. Schlatmann and A.E. Becker. Histologic changes in the normal aging aorta: implications for dissecting aortic aneurysm. *Am J Cardiol*, 39(1):13–20, 1977.
- [126] Y. J. Shyy, H. J. Hsieh, S. Usami, and S. Chien. Fluid shear stress induces a biphasic response of human monocyte chemotactic protein 1 gene expression in vascular endothelium. *Proc Natl Acad Sci U S A*, 91(11):4678–4682, 1994.
- [127] RMS. Sigrist, J. Liau, A.E. Kaffas, M.C. Chammas, and J.K. Willmann. Ultrasound elastography: Review of techniques and clinical applications. *Theranostics*, 7(5):1303–1329, 2017.
- [128] M. Smoljkić, H. Fehervary, P. Van den Bergh, A. Jorge-Peñas, L. Kluyskens, S. Dymarkowski, P. Verbrugghe, B. Meuris, J. Vander Sloten, and N. Famaey. Biomechanical characterization of ascending aortic aneurysms. *Biomech Model Mechanobiol*, 16(2):705–720, 2016.
- [129] D.P. Sokolis. Passive mechanical properties and structure of the aorta: segmental analysis. *Acta Physiol (Oxf)*, 190:277–289, 2007.



- 
- [130] D.P. Sokolis. Effects of aneurysm on the directional, regional, and layer distribution of residual strains in ascending thoracic aorta. *J Mech Behav Biomed Mater*, 46:229–43, 2015.
  - [131] D.P. Sokolis, E.P. Kritharis, A.T. Giagini, K.M. Lampropoulos, S.A. Papadodima, and D.C. Iliopoulos. Biomechanical response of ascending thoracic aortic aneurysms: association with structural remodelling. *Comput Methods Biomech Biomed Engin*, 15(3):231–48, 2012.
  - [132] M. Spina and G. Garbin. Age-related chemical changes in human elastins from non-atherosclerotic areas of thoracic aorta. *Atherosclerosis*, 24(1–2):267–79, 1976.
  - [133] Blausen.com staff. Medical gallery of blausen medical 2014. *WikiJournal of Medicine*, pages DOI:10.15347/wjm/2014.010. ISSN 2002–4436, 2014.
  - [134] Thoracic Aortic Aneurysm Surgery. <https://my.clevelandclinic.org/health/treatments/17527-thoracic-aortic-aneurysm-surgery>.
  - [135] T. Toda, N. Tsuda, I. Nishimori, D.E. Leszczynski, and F.A. Kummerow. Morphometrical analysis of the aging process in human arteries and aorta. *Acta Anat*, 106(1):35–44, 1980.
  - [136] O. Trabelsi, F.M. Davis, J.F. Rodriguez-Matas, A. Duprey, and S. Avril. Patient specific stress and rupture analysis of ascending thoracic aneurysms. *J Biomech*, 48(10):1836–43, 2015.
  - [137] O. Trabelsi, A. Duprey, J.P. Favre, and S. Avril. Predictive models with patient specific material properties for the biomechanical behavior of ascending thoracic aneurysms. *Ann Biomed Eng*, 44(1):84–98, 2016.
  - [138] O. Trabelsi, M. Gutierrez, S. Farzaneh, A. Duprey, and S. Avril. A non-invasive technique for ATAA rupture risk estimation. *Journal of Biomechanics*, 66:119–26, 2017.
  - [139] A. Tsamis, J.T. Krawiec, and D.A. Vorp. Elastin and collagen fibre microstructure of the human aorta in ageing and disease: a review. *J R Soc Interface*, 10(83):DOI: 10.1098/rsif.2012.1004, 2013.
  - [140] R. N. Vaishnav, J.T. Young, J. S. Janicki, and D. J. Patel. Nonlinear anisotropic elastic properties of the canine aorta. *Biophys J*, 12(8):1008–1027, 1972.
  - [141] R.N. Vaishnav and J. Vossoughi. Estimation of residual strains in aortic segments. *Biomedical Engineering II, Recent Developments: Proceedings of the Second Southern Biomedical Engineering Conference*, pages 330—33, 1983.
  - [142] A. Valentín, J.D. Humphrey, and G.A. Holzapfel. A multi-layered computational model of coupled elastin degradation, vasoactive dysfunction, and collagenous stiffening in aortic aging. *Ann Biomed Eng*, 39(7):2027–45, 2011.
-

- [143] E.M. van Disseldorp, N.J. Petterson, M.C. Rutten, F.N. van de Vosse, M.R. van Sambeek, and R.G. Lopata. Patient specific wall stress analysis and mechanical characterization of abdominal aortic aneurysms using 4d ultrasound. *Eur J Vasc Endovasc Surg*, 52(5):635–642, 2016.
- [144] E.M.J. van Disseldorp, P.P.N. Kempera, J. Nijsb, M.E.S.H. Tanc, F.N. van de Vosse, and R.G.P. Lopataa. Mechanical characterization of thoracic aortic aneurysms using 4d ultrasound: In vivo findings and in vitro verification. 2018.
- [145] K.Y. Volokh. Comparison of biomechanical failure criteria for abdominal aortic aneurysm. *J Biomech*, 43(10):2032–4, 2010.
- [146] D.A. Vorp, B.J. Schiro, M.P. Ehrlich, T.S. Juvonen, M.A. Ergin, and B.P. Griffith. Effect of aneurysm on the tensile strength and biomechanical behavior of the ascending thoracic aorta. *Ann Thorac Surg*, 75:1210–14, 2003.
- [147] J. Vossoughi and A. Tozeren. Determination of an effective shear modulus of aorta. *Russian Journal of Biomechanics*, 20(3):235–9, 1987.
- [148] H. Weisbecker, C. Viertler, D. M. Pierce, and G. A. Holzapfel. The role of elastin and collagen in the softening behavior of the human thoracic aortic media. *J Biomech*, 46(11):1859–65, 2013.
- [149] M.A. Whittle, P.S. Hasleton, J.C. Anderson, and A.C. Gibbs. Collagen in dissecting aneurysms of the human thoracic aorta. increased collagen content and decreased collagen concentration may be predisposing factors in dissecting aneurysms. *Am J Cardiovasc Pathol.*, 3(4):311–9, 1990.
- [150] A. Wittek, K. Karatolios, P. Bihari, T. Schmitz-Rixen, R. Moosdorf, S. Vogt, and C. Blase. In vivo determination of elastic properties of the human aorta based on 4D ultrasound data. *J Mech Behav Biomed Mater*, 27:167–183, 2013.
- [151] A. Wittek, K. Karatolios, C.P. Fritzen, J. Bereiter-Hahn, B. Schieffer, R. Moosdorf, S. Vogt, and C. Blase. Cyclic three-dimensional wall motion of the human ascending and abdominal aorta characterized by time-resolved three-dimensional ultrasound speckle tracking. *Biomech Model Mechanobiol*, 15(5):1375–88, 2016.
- [152] Y. Xuan, Z. Wang, R. Liu, H. Haraldsson, MD. Hope MD, DA. Saloner, JM. Guccione, L. Ge, and E. Tseng. Wall stress on ascending thoracic aortic aneurysms with bicuspid compared with tricuspid aortic valve. *J Thorac Cardiovasc Surg*, 492-500:156(2), 2018.
- [153] Z. Yosibash, I. Manor, I. Gilad, and U. Willentz. Experimental evidence of the compressibility of arteries. *J Mech Behav Biomed Mater*, 39:339–54, 2014.

- [154] K. Zhang, X. Qian, X. Mei, and Z. Liu. An inverse method to determine the mechanical properties of the iris in vivo. *Biomed Eng Online*, 13:66:doi: 10.1186/1475-925X-13-66, 2014.
- [155] B. Zhou, S. Ravindran, J. Ferdous, A. Kidane, MA. Sutton, and T. Shazly. Using digital image correlation to characterize local strains on vascular tissue specimens. *J Vis Exp*, (107):e53625:doi: 10.3791/53625, 2016.



## Appendix A. Image segmentation

Image segmentation is the process of extracting the geometry of interest in which each pixel contains similar properties in each region. There are different ways to implement image segmentation such as thresholding which is the simplest method of image segmentation. This method is based on a threshold value to transform a gray-scale image into a binary image based on discontinuities in grayscale or color properties. Second method, "Region-growing", determines the neighboring pixels within one region based on initial seed points having similar properties. Each pixel is compared with its neighbors and then if a similarity criterion is satisfied, the pixel can be selected to belong to the group as one of its neighbors. Another method is based on the calculation of the centerline in the vessel and creating a mask using a fitting algorithm. Medical image segmentation tools that are used or will be used for segmentation are: Mimics (The common software used in this study), Crimson and Circle Cardiovascular Imaging (the software will be used for future segmentations). Their Function and applications are discussed below.

1. **Mimics (Materialise's Interactive Medical Image Control System)** is software for processing medical images and generating 3D models. Mimics employs 2D cross-sectional medical images such as magnetic resonance imaging (MRI) and computed tomography (CT) to generate 3D models, which can then be directly linked to CAD, surgical simulation and advanced engineering analysis.

A set of stacked 2D cross-sectional medical images (commonly in the DICOM format) acquired by CT or MRI scanners are imported to Mimics. It create models based on the grayvalue (Hounsfield units in CT images) within these images. A grayvalue is a number associated with an image pixel defining the shade (white, gray, or black) of the pixel. There is a direct association between material density of the scanned object and the grayvalue assigned to each pixel in the image data. By classifying all grayvalue in distinct groups, the image data can be segmented, and models created. This type of segmentation is called thresholding and yields accurate models. In this work besides thresholding method "Region-growing" method is also used to generate 3D models. "Dynamic Region Growing" does not need thresholding. Instead, Mimics creates a mask based on the comparison of the surrounding pixels to a selected datapoint's grayvalue

and automatically determining threshold values. It exports the outer surface of the 3D model as STL format. Using the segmentation and known information on the pixel size and the distance between the image slices, Mimics can calculate a 3D model.

2. **Crimson** creates patient-specific models of vessels using visualization and responsive user interface. The segmentation starts by importing the DICOM images to CRIMSON. The approximate centerlines of the vessels is specified by a few clicks and then the segmentation toolbox is used to segment the vessel wall at multiple locations along the centerline by fitting circles in order to create mask. The first 3D segmentation of one of the vessels is created using the fitting algorithm. These steps are repeated for all the vessels of interest in the vessel tree and a 3D model is then created. The output as 3D model can be exported in different branches of the geometry.
3. **Circle Cardiovascular Imaging** is an application for managing and evaluating cardiovascular MRI and CT scans. The DICOM images are imported to Circle Cardiovascular Imaging tool. The advantage of this software is that , the error in this software is limited because each pixel of the input image is divided into a set of sub pixels. This software works based on the approximate calculation of centerlines of the vessel by a few clicks and then an automatic segmentation is implemented. Moreover, this software is able to perform flow analysis in which the velocity profile and wall shear stress distribution in each segment can be visualized.

---

## Appendix B. Author's publications

### Peer-reviewed journal articles (In chronicle order)

1. S. Farzaneh, O. Trabelsi, A. Duprey, B. Chavent and S. Avril. Identifying local arterial stiffness to assess the risk of rupture of ascending thoracic aortic aneurysms. Submitted to the journal of annals of biomedical engineering (under revision).
2. S. Farzaneh, O. Trabelsi, and S. Avril. Inverse identification of local stiffness across ascending thoracic aortic aneurysms. *Biomechanics and Modeling in Mechanobiology*, doi: 10.1007/s10237-018-1073-0, 2018.
3. S.J. Mousavi, S. Farzaneh and S. Avril. Computational predictions of damage propagation preceding dissection of ascending thoracic aortic aneurysms. *International Journal for Numerical Methods in Biomedical Engineering*, 34(4):e2944. doi: 10.1002/cnm.2944, 2018.
4. O. Trabelsi, M. Gutierrez, S. Farzaneh, A. Duprey, and S. Avril. A non-invasive technique for ATAA rupture risk estimation. *Journal of Biomechanics*, 66:119-126, 2017.
5. S. Farzaneh, O. Paseta, M.J. G-Benito. Multi-scale finite element model of growth plate damage during the development of slipped capital femoral epiphysis. *Journal of Biomechanics and Modeling in Mechanobiology*, 14(2):371-85, 2015.
6. S.J. Mousavi, N. Nassiri, N. Masoumi, N. Nassiri, M. Majdi-N, S. Farzaneh, A.R. Djalilian and G.A. Peyman. Finite element analysis of blunt foreign body impact on the cornea after PRK and LASIK. *Journal of Refractive Surgery*, 28(1):59-64, 2011.

### Conferences (In chronological order)

1. S. Farzaneh, O.Trabelsi and S. Avril. Rupture risk estimation of ATAA based on identification of local membrane stiffness. ECCM-ECFD 2018, Glasgow, UK 11-15 June.
2. S. Farzaneh, O.Trabelsi and S. Avril. Identification of regional stiffness distribution across ascending thoracic aortic aneurysms using ct images: an inverse method. CMBBE 2018, Lisbon, Portugal, 26-29 March.
3. S. Farzaneh, O.Trabelsi and S. Avril. Inverse identification of local stiffness distribution across ascending thoracic aortic aneurysms. ESB 2017, Seville, Spain, 2-5 July.







NNT : 2019LYSEM006

Solmaz Farzaneh

Assessment of the ascending thoracic aortic aneurysm rupture risk based on the local arterial stiffness

**Keywords :** Non-invasive inverse method; Local extensional stiffness; Finite-elements; Patient-specific rupture risk criterion; stretch ratio risk criterion

**Abstract:**

A methodology named local extensional stiffness identification (LESI) was developed to identify in vivo local extensional stiffness non-invasively in patients suffering from ascending thoracic aortic aneurysm (ATAA). An aneurysm is a ballooning of an artery, which can burst and lead to life threatening hemorrhage. For the thoracic aorta, a diameter greater than 5.5 cm is generally considered aneurysmal, and surgical intervention is recommended. The diameter as current risk indicator causes very high rate of misprogrammed surgical interventions. In this thesis it is suggested to assist physicians in taking the correct decision by considering biomechanical factors such as in vivo material properties of the tissue as we previously showed that there is a significant correlation between a stretch based rupture criterion of the ATAA and the local extensional stiffness of the aorta. Gated computed tomography (CT) scans and brachial pressures were used to assess the risk of rupture of ATAAs. Using these images, we apply the LESI method for 11 patients to first reconstruct the strain throughout the cardiac cycle and then relate the obtained strains to tensions, through local equilibrium equations, to estimate the local extensional stiffness at every position. A very good correlation between the rupture risk criterion and the local extensional stiffness was found. Finally we show that patients can be separated in two groups: a group of stiff and brittle ATAA and a group of relatively compliant ATAA. We also apply the LESI methodology to other modalities, e.g. ultrasound and MRI, to investigate the possibility of substituting CT scans by other modalities avoiding radiations.

NNT : 2019LYSEM006

Solmaz Farzaneh

## Evaluation du risque de rupture d'un anévrisme de l'aorte thoracique ascendante en fonction de la rigidité artérielle locale

Spécialité: Mécanique et ingénierie

Mots clefs : Méthode inverse non invasive; Rigidité membranaire locale; Éléments finis; Critère de risque de rupture spécifique au patient; Critère de risque en déformation

### Résumé :

Une méthodologie appelée identification de la rigidité membranaire locale (LESI en anglais) a été développée pour identifier de manière non invasive la rigidité membranaire locale in vivo chez les patients souffrant d'anévrisme de l'aorte thoracique ascendante (ATAA). Pour l'aorte thoracique, un diamètre supérieur à 5.5 cm est considéré comme anévrisimal et une intervention chirurgicale est recommandée. Le diamètre en tant qu'indicateur de risque actuel entraîne un taux élevé d'interventions chirurgicales mal programmées. Il est suggéré d'aider les médecins à prendre la bonne décision en prenant en compte des facteurs biomécaniques tels que les propriétés matérielles comme nous l'avons précédemment indiqué en montrant qu'il existe une corrélation significative entre un critère de rupture de l'ATAA basé sur la déformation et la rigidité membranaire locale de l'aorte. La tomодensitométrie et les pressions brachiales ont été utilisées pour évaluer le risque de rupture des ATAAAs. Nous appliquons la méthode LESI à 11 patients pour reconstruire la déformation tout au long du cycle cardiaque, puis associer les déformations obtenues à des tensions, par le biais d'équations d'équilibre locales, afin d'estimer la rigidité membranaire locale à chaque position. Une très bonne corrélation entre le critère de risque de rupture et la rigidité membranaire locale a été trouvée. Enfin, nous montrons que les patients peuvent être séparés en deux groupes: un groupe d'ATAAAs rigides et fragiles et un groupe d'ATAAAs relativement extensibles. Nous appliquons également la méthodologie LESI à l'échographie et l'IRM, pour étudier la possibilité de remplacer le scanner par d'autres modalités.